Exploring the Structures and Dynamics of Amine-Templated Formate Frameworks

Lydia Grace Burley

Master's by Research

School of Physical Sciences

University of Kent

2019



Summary

Metal-Organic Frameworks (MOFs) have become increasingly interesting over the past two decades as highly versatile materials for multiple applications stemming from the abundance of metal centres and organic ligands which can be incorporated to create multidimensional synergetic systems. Inclusion of charged guest molecules into perovskite-like MOFs can bring about remarkable ferroelectric properties through directional hydrogen bonding, some of which may be suggestive of relaxor-like behaviour, which would imply some remnant disorder of the structure below the characteristic transition temperatures. It is also likely to increase the transition temperature at which ferroelectric properties emerge to above ambient temperature, which could also be achieved by utilising lanthanide centres to increase the electronegativity difference between the metal centre and organic ligand. Mixed-ligand perovskite-like MOFs are rare, but alteration of their stoichiometry may result in extraordinary structures and properties.

The first part of this thesis focuses on dense perovskite-like MOFs with ABX_3 stoichiometry to probe disorder below the transition temperatures of two members of the known ferroelectric $NH_4\mathbf{M}(HCO_2)_3$ family, specifically $NH_4Mn(HCO_2)_3$ and $NH_4Zn(HCO_2)_3$. Studies of these frameworks using single crystal neutron diffraction and quasi-elastic neutron scattering suggest minimal crystallographic disorder in the low temperature phase but the retention of significant dynamics, which may be key to other relaxor-like properties. The second half of this work characterises a novel amine templated mixed-ligand perovskite-like MOF with the stoichiometry $((CH_3)_2NH_2)Er(C_2O_4)(HCO_2)_2$ in which the dimethylammonium cation is ordered at room temperature and remains ordered up to 500 K. It also reports a novel family $((CH_3)_2NH_2)Ln(C_2O_4)_{1.5}(HCO_2)$ where *Ln* = Tb, Dy, Ho and Er where the A-site cation is highly disordered such that it can only be identified by allied techniques. All lanthanide phases are paramagnetic to low temperature with antiferromagnetic interactions becoming prominent on cooling.

Word count: 20,471

Acknowledgements

I'd first like to thank my supervisor, Dr Paul Saines, for your support and guidance throughout the duration of this year and for teaching me skills and knowledge that I will take with me through my career. I have learnt so much from you this year. I'd also like to thank our postdoctoral researcher, Dr Anant Kumar Srivastava, for all your help and patience with single crystal work, amongst teaching me personal lab habits which became valuable to my work. Thank you to all in the Saines group who have made our research group a friendly one, I have enjoyed getting to know all of you and wish you all the best. I'd also like to thank the School of Physical Sciences for awarding me a Master's scholarship.

Thank you to my dad for your optimism and always helping me see the positives, thank you to my mum for showing me so much strength even when times were hard, you have both helped me more than you know. Thank you to Wes for your endless encouragement and for always being by my side.

This year would not have been such and success without all of you and for that I am grateful.

Contents

Chapter 1. Introduction **1**

1.1 Electric Order……..…2

1.2 Magnetic Order……...7

1.3 Multiferroics……..11

1.4 Metal-Organic Frameworks……...12

1.5 $NH_4M(HCO_2)_3$…….....17

1.6 $AH^+Ln(HCO_2)_4$……..19

1.7 Project Aims……..22

Chapter 2. Experimental Methods **24**

2.1 Synthetic Procedures…….24

2.2 X-ray Diffraction…….....27

2.3 Neutron Diffraction…….....33

2.4 Neutron Scattering…….35

2.5 Super Conducting Quantum Interference Device (SQUID)…….….37

2.6 Thermogravimetric Analysis and Differential Scanning Calorimetry (TGA-DSC)…….38

2.7 Infrared Spectroscopy……38

Chapter 3. Neutron Scattering from $NH_4M(HCO_2)_3$ Frameworks 40

3.1 Powder X-ray Diffraction…….....40

3.2 Single Crystal Neutron Diffraction…….……..43

3.3 Quasi-elastic Neutron Scattering……...49

3.4 Infrared Spectra…….52

3.5 Conclusion…….53

Chapter 4. Experimental Results of $((CH_3)_2NH_2)Ln(C_2O_4)_x(HCO_2)_y$ 54

4.1 Structural Determination and Physical Properties of $((CH_3)_2NH_2)Er(C_2O_4)(HCO_2)_2$……54

4.2 Structural Determination and Physical Properties of the $((CH_3)_2NH_2)Ln(C_2O_4)_{1.5}(HCO_2)$ Family…….64

Chapter 5. Conclusion and Future Work 78

Bibliography 80

Appendix 85

Abbreviations

MOF	Metal-Organic Framework
PBU	Primary Building Unit
SBU	Secondary Building Unit
A	A-site cation
B	B-site metal
X	Organic linker or ligand
Z	Atomic number
AMFF	Ammonium Metal-Organic Framework
M	Metal node
TM	Transition metal
Ln	Lanthanide
TM-AMFF	Transition Metal based Ammonium Metal-Organic Framework
Ln-AMFF	Lanthanide based Ammonium Metal-Organic Framework
Ln-MOF	Lanthanide based Metal-Organic Framework
PSM	Post-Synthetic Modification
PSP	Post-Synthetic Purification
1Mn	$NH_4Mn(HCO_2)_3$
2Zn	$NH_4Zn(HCO_2)_3$
1Er	$((CH_3)_2NH_2)Er(C_2O_4)(HCO_2)_2$
2Tb	$((CH_3)_2NH_2)Tb(C_2O_4)_{1.5}(HCO_2)$
3Dy	$((CH_3)_2NH_2)Dy(C_2O_4)_{1.5}(HCO_2)$
4Ho	$((CH_3)_2NH_2)Ho(C_2O_4)_{1.5}(HCO_2)$
5Er	$((CH_3)_2NH_2)Er(C_2O_4)_{1.5}(HCO_2)$
$tmenH_2$	N,N,N’,N’-tetramethylethylenediamine
$dmenH_2$	N,N’-dimethylethylenediamine
PMN	$Pb(Mg_{1/3}Nb_{2/3})O_3$
KLT	$K_{1-x}Li_xTaO_3$
KMN	$KTa_{1-x}Nb_xO_3$
Å	Angstrom
a, b, c	Crystallographic axis
DMA	Dimethylammonium
DMF	Dimethylformamide

SCXRD	Single Crystal X-ray Diffraction
CIF	Crystallographic Information File
GUI	Graphical User Interface
PXRD	Powder X-ray Diffraction
ND	Neutron Diffraction
SXD	Single Crystal Diffractometer
SCND	Single Crystal Neutron Diffraction
QENS	Quasi-elastic Neutron Scattering
INS	Inelastic Neutron Scattering
ENS	Elastic Neutron Scattering
EISF	Elastic Incoherent Scattering Factor
MSD	Means Square Displacement
IR	Infrared
SQUID	Superconducting Quantum Interference Device
DC	Direct Current
FC	Field-cooled
ZFC	Zero field-cooled
TGA	Thermogravimetric Analysis
DSC	Differential Scanning Calorimetry
FeRAM	Ferroelectric Random-Access Memory
CSD	Cambridge Structural Database
R&D	Research and Development
CWA	Chemical Warfare Agents
SCO	Spin Crossover
VOC	Volatile Organic Components
LRFD	Long Range Ferroelectric Domains
PNR	Polar Nanoregions
LRO	Long-Range Order
DP	Displacement Parameter
t	Goldschmidt tolerance factor
P	Electrical polarisation
E	Applied electric field
ε_0	Permittivity within a vacuum (8.854×10^{-12} F m^{-1})
χ_e	Dielectric susceptibility

C	Capacitance
ε_r	Dielectric constant
T_C	Curie temperature
T_N	Néel temperature
T_B	Burns temperature
T_D	Depolarisation temperature
M	Magnetisation
χ	Magnetic susceptibility
H	Applied magnetic field
C	Curie constant
T	Temperature
θ	Weiss temperature
k	Boltzmann constant
μ_B	Bohr magneton
μ_{eff}	Effective magnetic moment
F_{calc}	Calculated scattering factor
F_{obs}	Observed scattering factor
2θ	Bragg angle
K	Kelvin
°C	Degrees Celsius
F	Farads
cm^{-1}	Wavenumber
%T	Percent transmittance

Chapter 1

Introduction:

Interest in Metal-Organic Frameworks (MOFs) has grown immensely over the past couple of decades as the crystalline coordination complexes have become highly recognisable and interesting to material chemists [1-3]. There is rapidly growing interest in dense MOFs which are not porous or by the inclusion of charged guest molecules into the cavities that would otherwise be void space rendering them inaccessible. In comparison to porous MOFs where the cavities are vacant. An abundance of organic molecules available are typically incorporated as the bridging linker, so the pores can be tailored for purpose.

Constructed from relatively simple starting components they can be transformed into highly valuable and useful materials. Fashioned from simple metal centres connected by organic ligands, these primary building units (PBUs) assemble into multidimensional lattices which have given promise to a vast range of applications and bring together the benefits of both organic and inorganic components in a single system.

Porous MOFs offer themselves as gas storage systems or sites for catalysis [4-6]. Longer linkers give rise to larger pores, therefore can allow uptake of larger gas molecules, or more catalytic sites. Organic linkers allow the system to possess a degree of flexibility, facilitating the uptake of gas molecules of varying sizes as the framework is not completely rigid and can bend to allow these molecules to migrate into the pores. This has been the focus of many researchers due to the importance of air pollution remediation, in particular, greenhouse gas capture. Charged guest molecules within dense MOFs can become ordered with a polar pattern due to directional hydrogen bonding between themselves and the anionic framework, resulting in ferroelectricity emerging below the characteristic transition temperature [7]. Numerous molecules can be incorporated into the cavities, including hydrogen-rich compounds, such as amines. This provides the potential to develop MOFs with useful ferroelectric properties to be used in wide range of applications such as ferroelectric-RAM and modulators for

optical applications [8, 9]. If coupled with typically weak ferromagnetism, MOFs offer exciting possibilities in multiferroics [10]. These properties typically arise well below room temperature, but efforts are in place to increase transition temperatures to, ideally, above room temperature. Some of these frameworks show signs of belonging to a particular sub-class of ferroelectrics, relaxor ferroelectrics, which are typically diagnosed by possessing a high frequency dependent dielectric constant [11, 12]. In comparison to traditional oxide materials, where relaxor-like behaviour can arise due to cation-doping induced disorder, in hybrid organic-inorganic materials, it is suspected to be achievable by increasing the electronegativity difference between the metal ion and anionic linker.

Two different families of dense MOFs will be presented here, both featuring ammonium cations in the pores and both incorporating the smallest and simplest carboxylate, the formate. The first have the general formula $NH_4B(HCO_2)_3$ where B = first row transition metals Mn and Zn [11, 12]. The second is a mixed-ligand system combining the formate ligand with the oxalate ligand, with the general formula $AB(C_2O_4)_x(HCO_2)_y$. Both families have potential to be developed into ferroelectric functional materials due to the presence of charged guest molecules. The former family is known to contain ferroelectric members, with frequency dependant dielectric properties, suggesting relaxor-like behaviour [11, 12]. One member of the latter, $((CH_3)_2NH_2)Er(C_2O_4)(HCO_2)_2$, has shown to exhibit a state at room temperature with ordered dimethylammonium A-site cations. The latter are new materials, first reported in this thesis, but studies so far have shown interesting results which have only sparked interested further. Before describing these compounds in detail, it is first necessary to explain fundamentals of ferroic properties, particularly ferroelectricity and ferromagnetism.

1.1 Electric order

Electrical polarisation, P, is the average dipole moment per unit volume in a solid, and is proportional to the applied electric field, E [13].

$$P = \varepsilon_0 \chi_e E \qquad \text{(Equation 1.1)}$$

where ε_0 is the dielectric permittivity within a vacuum (8.854×10^{-12} F m^{-1}) and χ_e is the dielectric susceptibility, which is dimensionless. The capacitance, a materials ability to

store electrical charge, of a circuit in the absence of a solid can be used to determine the dielectric susceptibility, and the ratio between the capacitance with a solid present, C, and when a solid is absent, C_0, both measured in Farads, equals the dielectric constant, ε_r.

$$\frac{C}{C_0} = \varepsilon_r \qquad \text{(Equation 1.2)}$$

These two terms, the dielectric constant and dielectric susceptibility are related to each other by:

$$\varepsilon_r = 1 + \chi_e \qquad \text{(Equation 1.3)}$$

Dielectric properties within materials is one of the most common properties a material can possess. Dielectrics in the absence of an applied electric field are electric insulators, with no net polarisation, but can become polarised when a field is applied due to being very poor conductors of electricity. The relationship between the applied field and polarisation is linear, with increasing electric field comes an increasing polarisation. Removal of the field results in the loss of the polarisation of the material which therefore does not have the ability to store any charge. Paraelectric materials are similar in that they have no initial zero-field polarisation but differ in a way that locally they contain randomly orientated dipoles which align with an applied electric field. The alignment of pre-existing diploes allows a weaker applied field to result in a higher polarisation. Similarly to dielectrics, the polarisation decreases back to zero when the applied field is removed. As paraelectrics are cooled and interactions become significant, ferroelectricity and antiferroelectricity can emerge which will be discussed below.

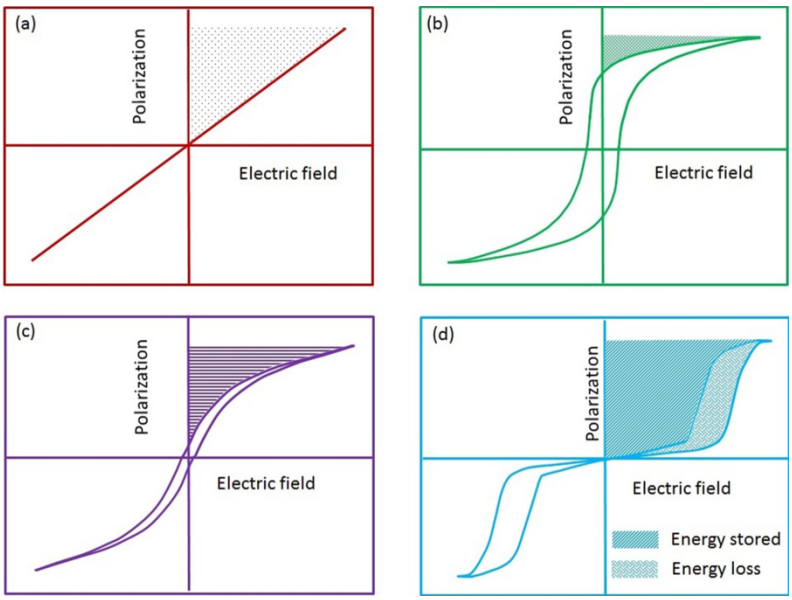


Figure 1.1. Hysteresis loops of a) a paralectric material, b) ferroelectric material, c) a relaxor-like material and d) an anti-ferroelectric, reproduced from A. Chauhan *et al* [14].

1.1.1 Ferroelectricity and antiferroelectricity

The polar nature of ferroelectric materials makes them susceptible to a spontaneous switchable electrical polarisation, therefore it cannot be ignored that ferroelectric materials must exhibit polar point groups and must therefore have a polar space group. This functionality makes them appealing for numerous applications such as photovoltaic applications and non-volatile memory devices (i.e. FeRAM) [15, 16]. Unlike in dielectric and paraelectric materials, ferroelectric materials maintain remnant polarisation even after the applied field is removed, and application of an applied field in the opposing direction reverses the direction of the polarisation; this particular occurrence creates a single hysteresis loop graphically (see Figure 1.1). These particular materials have a characteristic transition temperature, Curie temperature, T_C, associated with a phase transition. Above T_C the material is paraelectric and below T_C it is a lower-symmetry ferroelectric phase in which ions are displaced in the same direction inducing a long-range polarisation.

In oxides, ferroelectricity can arise as a result of off-centred metal octahedra, as it is energetically favourable to form stronger metal-oxygen bonds, and this can be referred to as displacive induced ferroelectricity [13]. But unlike in conventional inorganic materials, ferroelectricity in hybrid-organic frameworks typically arises from directional hydrogen bonding between the guest molecule and the anionic framework, this can be referred to an order-disorder induced ferroelectricity. In the late 19th century the Rochelle salt ($NaKC_4H_4O_6$•$4H_2O$, potassium sodium tartrate tetrahydrate) was discovered by the Curie brothers and was reported to exhibit a large piezoelectric effect, but it was not until the 1920's before it was discovered to be ferroelectric [17]. In a study by Valasek [18] in 1920 the anomalous dielectric properties of the materials are discussed, and hysteresis loops are presented. Possibly one of the most interesting properties of the Rochelle salt is that is possess two Curie points, and the ferroelectric phase is confined between 291 K and 249 K, a relatively high temperature for a material to be in a ferroelectric phase [17]. Above room temperature, at 324 K, the material is paraelectric and belongs to the space group $P2_12_12$, at 274 K the system has passed through the first T_C, through an order-disorder phase transition and is monoclinic, belonging to the space group $P2_1$, and in the ferroelectric phase. Then at 213 K it is once again in the paraelectric phase and the space group $P2_12_12$.

Interestingly deuteration of Rochelle salt results in a wider temperature range at which the ferroelectric phase is dominant. This inspired the studies of materials based on the salt, KH_2PO_4 (KDP, monopotassium phosphate) in the 1930's, which were discovered as another class of hydrogen bonded ferroelectrics which led onto the theory that hydrogen bonding must be present for ferroelectricity to arise [19]. The discovery of the first non-hydrogen bonded ferroelectric in 1945, $BaTiO_3$ sparked the interest into the now famous perovskite ferroelectrics, leading to functional properties at much higher temperatures [20].

Antiferroelectric materials follow the same linear relationship as dielectrics at low levels of the applied electric field. However, when the applied field reaches a certain threshold, in either direction, it induces a ferroelectric state and consequently, results in a double hysteresis loop graphically. This unique property has made them subject to energy storage studies due to having a higher dielectric storage density compared to ferroelectrics [14, 21]. This transition with applied fields is commonly attributed to ions in antiferroelectrics being displaced in opposite directions such that the dipoles cancel out; applying an electrical field to these materials causes the displaced ions to align in the same direction.

Within a ferroelectric material there are microscopic domains of uniform polarisation which are all aligned in the same direction, but this is not true between these domains. When subjected to an applied electric field, the domains can align with respect to one another, producing an overall net polarisation [13, 22]. The relationship between polarisation and applied electric field is represented by a hysteresis loop, (see Figure 1.1).

1.1.2 Relaxor ferroelectrics

A sub-class of ferroelectric materials are relaxor-like ferroelectrics which exhibit dielectric relaxation and ferroelectricity, hence the coined term "relaxors", and are typically non-polar [23]. Although the definition of relaxor ferroelectric is still debated, they can be classified by having no well-defined Curie temperature and can often be called ferroelectrics with a diffuse phase transition. These can be differentiated from conventional ferroelectrics in a few ways; firstly, by plotting the dielectric constant as a

function of temperature, ferroelectrics show sharp peaks whereas the peak produced from a relaxor is highly diffuse and broad [24]. Also, by producing a much slimmer hysteresis loop, and the field induced remnant polarisation decreases much more smoothly compared to ferroelectrics, whose polarisation vanishes above the T_C [24].

Relaxor-like behaviour can arise through heterogeneity in composition, such as mixed A- or B-sites in the general formula ABX_3 of ionic solids, particularly perovskites [23]. The substitution of ions within this stoichiometry plays a role with differing polarisabilities, valence state and size facilitating different dipolar effects and cease formation of long-range order (LRO). The discovery of the first relaxor is a compositional heterogenous system at the B-site, $Pb(Mg_{1/3}Nb_{2/3})O_3$ (PMN), and has sparked over 60 years' worth of research and development (R&D) [20]. PMN's polar structure can be described as a superparaelectric model, where polar nanoregions (PNR) are within a non-polar matrix, the volume fraction of these PNR's increase as the material is cooled to 15 K, while more general relaxors can be described as exhibiting heterogeneous polar states at the nanoscale [25]. The phase transition in relaxors is more complex than in ferroelectrics, consisting of 3 stages. The high temperature paraelectric phase, above the Burns temperature, T_B, conforms to the Curie-Weiss law, stage 1 [20]. Cooling to below this results in no long-range ferroelectric domains (LRFD) but no longer obeys the Curie-Weiss law and possess polar regions, stage 2. As the LRFD begins to become present, it passes through a depolarisation temperature, T_D, into stage 3 where LRFD is wholly present and the PNR are frozen.

A good example of typical behaviour in relaxor ferroelectrics are doped $KTaO_3$ phases. $KTaO_3$ is a cubic, pure ferroelectric, but when doped at either the A or B-site, the relaxor-like properties becomes enhanced and a dielectric response showing relaxor-like behaviour which deviates from the Curie-Weiss law is observed [20]. In both $K_{1-x}Li_xTaO_3$ (KLT) and $KTa_{1-x}Nb_xO_3$ (KTN) the doped-impurities (Nb and Li) occupy the off-centred sites and possess temperature dependent relaxational motion between said sites [26]. In KLT, 100 K above its T_C the Li sites have been shown to interact and form PNR by polarising regions surrounding it, modifying both static and dynamic properties of the undoped $KTaO_3$ [26]. An example of relaxor behaviour arising from another origin of disorder is $Cd_2Nb_2O_7$ [27]. In this system, there is progressive freezing of the orientational disorder in the alignment of O-Cd-O, along the [111] axis, which is

responsible for the relaxor-like behaviour. However, doping has been reported to enhance this phenomenon, specifically with copper [27]. Moreover, there have been studies reporting frequency dependent susceptibilities within hybrid systems, such as MOFs, which is indicative of relaxor behaviour. Dimethylammonium manganese formate ($DMAMn(HCOO)_3$) is just one of the hybrid organic-inorganic MOFs which has shown a dielectric permittivity of relaxor behaviour, particularly when the average size of the particles is 1 μm [28].

1.2 Magnetic order

Magnetism relates to the response of a material to an applied magnetic field, and the magnetisation, *M*, can be measured related to the magnetic susceptibility, χ and the strength of the applied magnetic field, *H*.

$$M = \chi H \qquad \text{(Equation 1.4)}$$

Materials which have a $\chi < 0$ are diamagnetic, and are repelled by a magnetic field, whereas those with $\chi > 0$ are paramagnetic, and are drawn into the magnetic field. The force of diamagnets are extremely small and can be overcome by attractive forces of magnetic dipoles. Diamagnetism is present in all atoms with paired electrons. Paramagnetism is present when there are unpaired electrons in an atom and is typically only found in elements in oxidation states with unpaired electrons, such as lanthanides or certain transition metals. Paramagnetism dominates over the diamagnetic properties that emerge from paired electrons. The spins of paramagnets are randomly orientated in the absence of an applied magnetic field, but once exposed to an applied field, become increasingly aligned to the direction of the field on cooling. Once this field is removed the induced magnetic moment is lost. This alignment is opposed by the thermal motion favouring a randomness to the spins; therefore, the thermal motion and magnetic susceptibility become dependent on temperature and can be expressed as using the Curie law:

$$\chi = \frac{C}{T} \qquad \text{(Equation 1.5)}$$

Where *C* is the Curie constant and *T* is the temperature, in Kelvin.

1.2.1 Ferromagnetism and anitferromagnetism

Ferromagnetism in materials arises when the spins of unpaired electrons align parallel with an applied magnetic field, inducing a magnetic moment. While antiferromagnetism arises in materials when said spins align anti-parallel and consequently, result in an overall zero magnetic moment [29].

Ferromagnetism is another ferroic order with analogous macroscopic responses to a magnetic field as ferroelectrics do to an electric field. Despite these similarities, the microscopic influences causing these macroscopic properties are very different due to the dependence of the alignment of magnetic moments compared to the cation displacement. It must be remembered that above the characteristic transition temperature, ferromagnets are paramagnets. The susceptibility of the paramagnetic phase now becomes related to the characteristic transition temperature, via the Curie-Weiss law:

$$\chi = \frac{C}{T - \theta} \qquad \text{(Equation 1.6)}$$

where θ is the Weiss constant which is positive for ferromagnets. When such systems are cooled to below their characteristic transition temperature, T_C, which is typically close to zero, they undergo a phase transition to the ferromagnetic phase. The spins cooperatively align in parallel with each other due to magnetic interactions between magnetic cations, leading to an overall magnetic moment that readily aligns with the applied magnetic field. Once aligned by the applied field the magnetisation of a ferromagnet remains when the field is removed, see Figure 1.2. This quality makes them appealing for uses such as data storage and transformers [30]. Ferromagnetism only occurs in a limited number of elements in the periodic table, a handful of lanthanides and a small group of transition metals, specifically iron, cobalt and nickel, due to the less diffuse 3*d* orbitals. Ferromagnetic properties arise more commonly when incorporated into multielement compounds, such as oxides. In molecular magnetism, instead of long-range interactions, there may be short-range interactions within smaller molecular clusters with no interactions between these clusters.

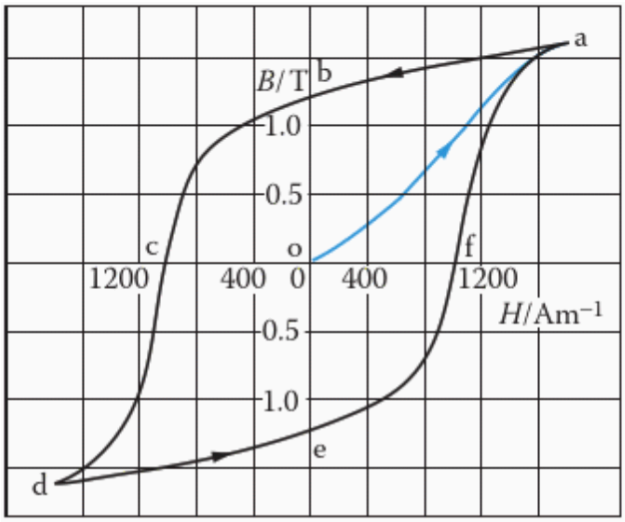


Figure 1.2. Hysteresis curve of a typical ferromagnet showing the field dependence of magnetisation. Image reproduced from L. E. Smart and E. A. Moore [13].

Alternating spin orientations in which half the spins are aligned parallel and the other half aligned antiparallel gives rise to antiferromagnetism, below their Néel temperature, T_N, and because the spins are alternating compared to each of its neighbours, the magnetic moment is cancelled out. The uses of antiferromagnetic systems are limited due to the absence of a spontaneous magnetisation, like in ferromagnetic materials. Antiferromagnets also act as Curie-Weiss paramagnets above their T_N, and if a Curie-Weiss plot is extrapolated, the extrapolated values of θ is above 0 K for ferromagnets, is 0 K for paramagnets, here, it is below 0 K for antiferromagnets. Obviously, a value θ below 0 K is impossible so antiferromagnetism becomes apparent on cooling to below this value, which is typically close to T_N, and deviates from the Curie-Weiss law [29]. A typical hysteresis loop resembles that in Figure 1.2, however the height of the loop is slimmer. Ferrimagnets have antiparallel spins similarly to antiferromagnets; however, the magnetic moments are unequal, thus producing a small overall magnetic moment. (see Figure 1.3). Ferrimagnetism can only be present in compounds, and never in a single pure element.

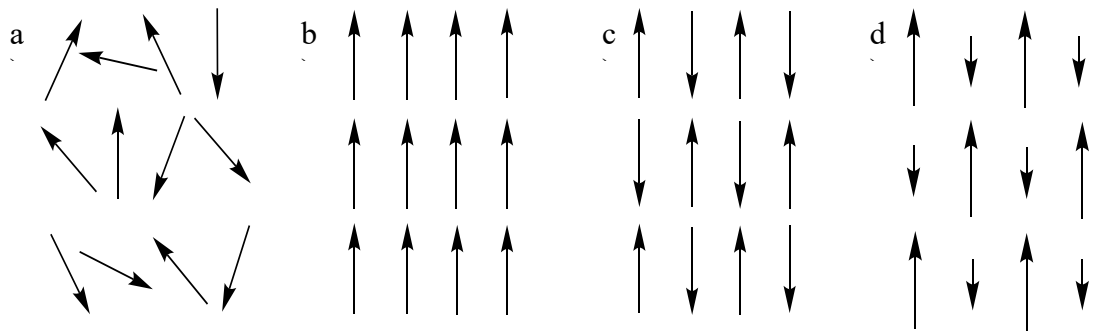


Figure 1.3. Diagrams showing the spin orientations in four different types of magnetism, a) Paramagnetism, b) Ferromagnetism, c) Antiferromagnetism and d) Ferrimagnetism.

1.2.2 Superexchange

Thus far the origins of magnetic orders have been discussed and what is observed, but the nature of magnetic interactions within compounds has not. For both ferro- and antiferromagnetic systems the interactions in compounds are typically mediated through a non-magnetic ion, but the bond angle at which this occurs is different. Superexchange is a phenomenon which favours the formation of antiferromagnetic states or as weakly coupled ferromagnetic states when the magnetic ion-non-magnetic ion-magnetic ion angles lie between 90^{o} and 180^{o}. The angle where superexchange favours a ferromagnetic state over an antiferromagnetic state will be determined by the system as this is a very system dependent process. These non-magnetic ions which the process is mediated through occurs using anions, including oxygen. The presence of the large anion between the two metal sites, prevents overlap of the very localised *d*-orbitals in **M**, where **M** is typically a transition metal or lanthanide with unpaired electrons, and inhibits any chance of direct exchange as the magnetic cations are too far apart. For superexchange to occur, there must be some type of energy of interaction present between them allowing of spins to align parallel or antiparallel, which is typically enabled by a greater depolarisation of electrons. For example, antiferromagnetic superexchange in NiO two d_{z2} orbitals occurs from two Ni^{2+} ions overlap with a single O^{2-} $2p_z$ orbital within a 180^{o} plane, see Figure 1.4 for orbital overlap within M-O-M 180^{o} plane. There are two mechanisms in which two consecutive 'hopping' procedures can take place, and a third which is supressed by Pauli's principle. If initially the spins in the Ni^{2+} d_{z2} orbital are parallel then the first step is allowed where an electron of opposing direction can 'hop' from the O^{2-} $2p_z$ orbital to a d_{z2} orbital in Ni^{2+} and form a pair of electrons but the second electron from the O^{2-} $2p_z$ orbital cannot undergo the second 'hopping' process, as it is limited by Pauli's principle. However, if the electron spins are antiparallel in the Ni^{2+} d_{z2} orbitals with respect to each other, then two pairs of electrons can result in two different configurations; the first with two pairs on both metal sites, and the other with one pair in the Ni^{2+} d_{z2} orbital and the other within the O^{2-} $2p_z$ orbital [13].

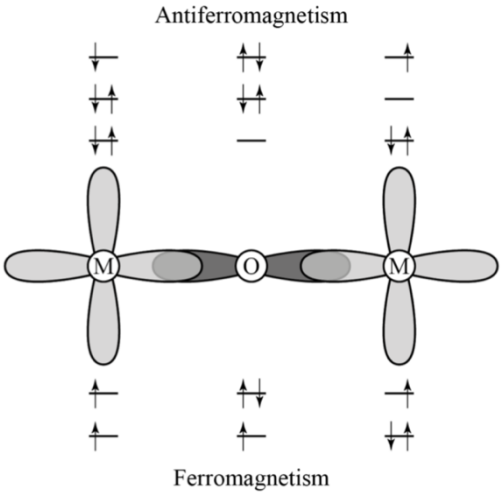


Figure 1.4. Superexchange within a material along a 180° M-O-M bond. The *d*-orbitals of the metal overlap with the *p*-orbitals of the oxygen. Above and below the M-O-M bond are the electron configurations of antiferromagnetic and ferromagnetic states, respectively.

Ferromagnetic superexchange differs in a way which it occurs along a 90° plane, so the *d*-orbitals couple orthogonally to two different *p*-orbital of the bridging anion. In this case the anion bridges between two orthogonal *d*-orbitals decreasing orbital overlap and the tendency for electron delocalisation. This leads to ferromagnetic Coulomb exchange as it minimises electrostatic effects.

1.3 Multiferroics

A multiferroic is the combining of two or more of the ferroic orders; ferroelectricity, ferromagnetism and ferroelasticity, within a given system [13]. There are two types of multiferroic: type I and type II. Type I is when the cooperative ferroic orders arise from different origins, such as a ferromagnetic metal centre weakly coupled with ferroelectricity induced by octahedral tilting, or directional hydrogen bonding of a non-magnetic ion. Type II is where the ferroelectric properties arise directly from magnetic ordering as a result of this breaking any inversion symmetry. So unlike in type I, there is strong coupling between the two parameters, and this is what differentiates them from each other. The handful of systems that combine ferroelectric and ferromagnetic properties have been explored extensively, more recently due to the magnetoelectric effect; the mutual control of electric polarisation by a magnetic field or magnetisation by an applied electric field. This cooperative behaviour can be applied to memory storage systems where information is written electronically and stored, then read out magnetically [31]. While it may appear that a system having both these cooperative

properties would be highly useful and beneficial, these types of systems are rare. To combine both ferroelectricity and ferromagnetism in a single-phase material requires contradiction of where these individual properties originate from. This is because for magnetism to arise it relies on the basis of unpaired *d*-electrons, whereas this actually lessens the distortion of octahedra which most commonly leads to ferroelectricity in perovskites due to the effects this arising from requiring a d^0 configuration at the B-site [32]. Even though coupling to another ferroic order offers another degree of freedom, it simultaneously restricts the properties to those which occur in both ferroic orders. For example, ferromagnetism often develops at extremely low temperatures, so in type II multiferroics, useful properties only arise at low temperatures.

1.4 Metal-Organic Frameworks

This project focuses on metal-organic frameworks (MOFs), which are a subset of coordination polymers or coordination networks. These are a relatively recent revelation in material science but have been explored extensively due to their numerous qualities and applications [1, 3, 5-6]. They contain metal nodes connected by organic linkers, see Figure 1.5, become transformed into multidimensional synergetic frameworks. Combining both organic and inorganic components, this brings together the advantages of both into a single collaborative system. As of 2016, there are 85,000+ MOFs in the CSD database and that number is only increasing [33]. Constructed from molecular entities or distinct molecular complexes, also known as secondary building units (SBUs), they can be transformed into complex and highly useful synergetic frameworks, and the abundant number of combinations, makes them even more attractive.

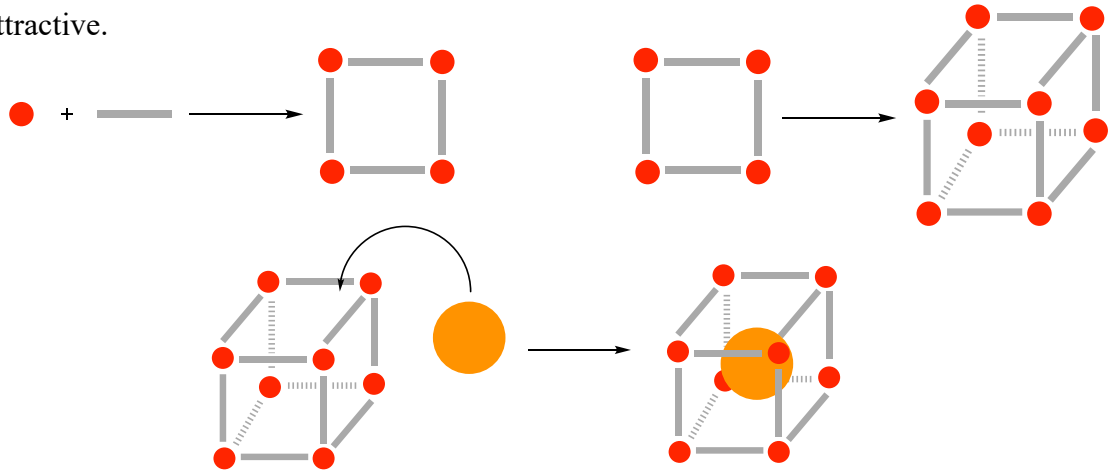


Figure 1.5. The formation of MOF. Red: metal node; grey: organic linker; orange: charged species occupying the pore but this only applies to dense MOFs.

Categorised as either porous or dense, each sub-class of MOF offers their own qualities. Porous MOFs possess cavities which are created during the formation of the framework. This property has been exploited extensively over the past two decades for a vast number of applications, due to the highly versatile size and shapes of these cavities. These materials can be applied to green applications, there are also carbon derived MOFs have been reported to be used in rechargeable battery materials as well as phototherapy procedures as drug delivery systems [34-37]. As mentioned previously, all these applications stem from the same factor, the porosity. The tailored chemical identity in these materials is focused towards their particular function, the type of ligand which is incorporated will have a direct effect on the porosity of MOFs, while providing the opportunity to functionalise these cavities through uncoordinated functional groups.

Dense MOFs are similar in that they have a multidimensional framework of metal centres connected systematically by organic ligands into an array of both organic and inorganic components but differ by either a lack of pores or have pores filled by a charged molecular cation that cannot be removed without decomposing the framework. The applications of dense MOFs are very different to those of porous MOFs but are equally useful. The presence of molecular cations allows the potential for other properties, such as ferroelectricity (see Section 1.1.1). Within dense MOFs there is a sub-class which adopt the perovskite-like formula of ABX_3, where A is the molecular cation, B is a divalent metal and X_3 are the organic linkers, most commonly formates. In 1926, Goldschmidt [38] derived a tolerance factor, *t*, which has been modified to represent hybrid systems with molecular organic anions, relating the ionic radii of the A-site cation, r_A, the B-site metal, r_B, and the length and radius of the organic ligand X, h_X and r_X respectively, to the architecture of the MOF it forms [39]:

$$t = \frac{(r_A + r_X)}{\sqrt{2(r_B + 0.5h_X}} \qquad \text{(Equation 1.7)}$$

Generally, when a tolerance factor between 0.8 and 1 occurs a perovskite-like structure is observed while a range of other structures with ABX_3 formulas are observed for other tolerance factors, see Figure 1.6.

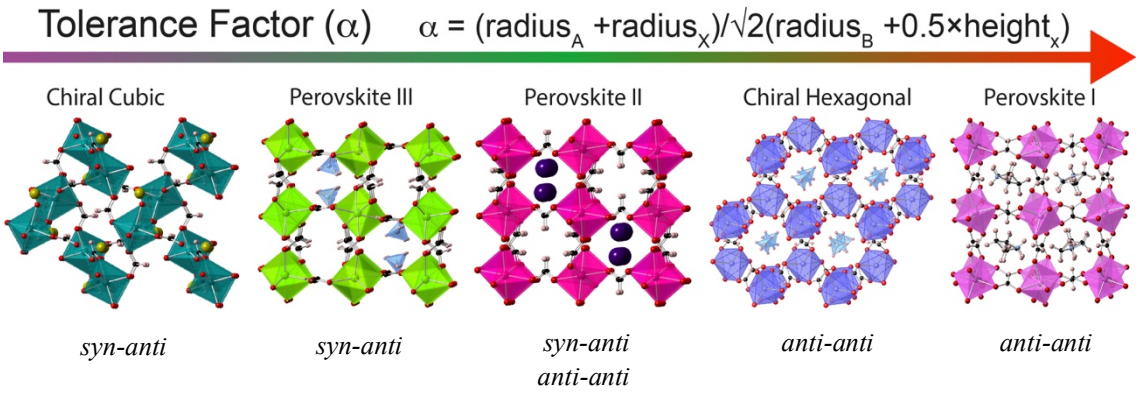


Figure 1.6. The relationship between the tolerance factor, which increases from left to right, and the ABX_3 MOF produced.

Porous and dense MOFs will now be discussed in detail and describing the key features as well as applications.

1.4.1 Porous MOF

What makes MOFs diverse and gives them an advantage over other porous materials is their tuneable properties, such as pore size. The size of the pore can simply be changed by the length of the organic linker, yet this can become risky when incorporating a linker which is too long, the stability of the framework may be jeopardised. However, desolvation of the MOF is more likely to result in collapse of the framework, if the framework remains intact, it becomes vulnerable to interpenetration. Porous MOFs can fall into any of four divisions depending on the durability of the framework; the 1st, display a high guest-host dependence, so high in fact that removal of the guest results in complete collapse of the cages, rendering it now useless [3]. The 2nd division have a much more robust structure where the guest can be separated from the host, so the porosity can be accessed, and the applications are completely different. If the framework is still stable after the removal of the guest molecule, but offers flexibility and allows for guest exchange, these are in the 3rd division, and finally, MOFs within the 4th division allow Post-Synthetic Modification (PSM), where adaptations to the system can occur at any site within the MOF.

The sites within the cavities are open to be utilised for purposes such as gas storage and separation, as well as catalysis, transport mediums for spin-crossover (SCO) materials and immobilising chemical warfare agents (CWAs) [40-47]. Catalytic MOFs not only decrease the amount of material needed in a reaction; they simultaneously minimise the

energy input needed to carry out the reaction. The potential use of MOFs for harvesting solar energy, converting and storing this energy to electricity and fuels for varying applications, are one of the processes which are in line to follow the 7th principle of green chemistry 'the use of renewable feedstocks' [34]. As MOFs containing complimentary chromophores have been involved with broad spectrum light harvesting and satisfy the criteria for solar energy conversion and successive storage abilities. The product of a MOF with porphyrin links incorporated into the framework along with boron dipyrromethene linkers allow the absorption of blue and red, and green light, respectively, give a black MOF which absorbs all visible wavelengths of light [34, 48].

However, gas storage and separation are possibly the most popular uses for MOFs, as the vast number of ligands available enables many structures to be made to accommodate and separate various gases. It is not only down to the size of the pore which makes them attractive, but linkers containing functional groups and open metal sites that aid gas adsorption also. A lot of focus has been put on MOFs for hydrogen storage and it is without a doubt that hydrogen is a difficult gas to store, but also for CO_2 capture as CO_2 is the number one contributor to greenhouse gases [34, 43]. Open metal sites within MOFs can also be useful in air pollution remediation when capturing volatile organic compounds (VOC). MOFs for water pollution remediation may seem unusual at first as this relies on a high stability in water, but Zr_6-based MOFs have been classed as exceptional candidates for this as they possess a high-water stability over a wide pH range [34, 49].

1.4.2 Dense MOFs

Classification of a MOF as dense, simply means the framework is not porous including materials with charged species that cannot be removed from what would otherwise be a void [50]. Most commonly a charged species is present for charge balancing purposes, but also brings about remarkable properties and are exploited for numerous applications. While usually porous MOFs are utilised for gas adsorption, a dense MOF has been reported to having excellent selective adsorption abilities [51]. These MOFs utilise the flexible framework to allow the uptake of the gas molecules as well as demonstrating a "gate opening" mechanism [51]. But possibly one of the most well renowned properties is the potential for multiferroicity (see Section 1.3), a property of

which conceptually makes them useful for memory storage devices, due to the coexistence of both magnetic and electric orders [52, 53]. With ferromagnetism arising from the ferromagnetic coupled metal centres, and ferroelectricity from directional hydrogen bonds formed between a molecular cation and the anionic framework pushing the cation through an order-disorder phase transition from a paraelectric to ferroelectric phase, and a multiferroic material is produced. This differs from inorganic perovskites as typically single atoms occupy the pores in perovskite-like MOFs. The organic linkers add distance between the metal centres, and consequently larger pores and a degree of flexibility, so that relatively larger species can inhabit the cavities, such as some amines.

Amines included into the A-site of ABX_3 MOFs has become a popular choice for studies into ferroelectric and multiferroic applications. Due to the numerous hydrogen atoms amines typically possess there is the ability to form directional hydrogen bonds with the framework, inducing an order-disorder transition from non-polar disordered phases to polar structures. The concept of amines incorporated as guest molecules has only been a recent one, with acid groups of hydrogen-heavy networks typically being utilised before [54, 55]. But due to the hydrogen-rich presence found in some amines, specifically dimethylamine, containing 8 hydrogen atoms, they seem an ideal candidate [54, 55]. But of course, guest molecules are not limited to amines, some aryl compounds have also been reported, giving rise to luminescent properties [56]. The cause of relaxor-like behaviour must vary from cation doping induced disorder as these lack compositional homogeneity, but it is not currently clear how this arises. In some cases, it can arise as a result of long-range order (LRO) of dipoles disrupted by partial cation disorder of the molecular cation, although ferroelectricity has been reported to be present due to this in formate MOFs [23, 57].

Most commonly in dense perovskite MOFs the ligand of choice is the formate ion; it is the simplest and smallest carboxylate but still permits significant hydrogen bonding with guest molecules due to the presence of two oxygen atoms per molecular unit, to favour a low temperature ferroelectric phase. As well as supporting coupling between magnetic metal centres, giving rise to magnetic properties or even multiferroic functionalities if the framework becomes polarised and ferroelectricity is induced within the system. Allowing 3 bridging modes, *syn-syn, syn-anti* and *anti-anti*, the formate ion can adapt to grant the inclusion of various sizes of guest molecules, see Figure 1.7.

Larger cations possessing the pores will drive the formate ion to adopt an *anti-anti* bridging mode as this results in maximum pore space available [58]. Whereas smaller cations, such as ammonium, will result in the formate linker adopting a *syn-syn* bridging mode, favouring non-perovskite structures.

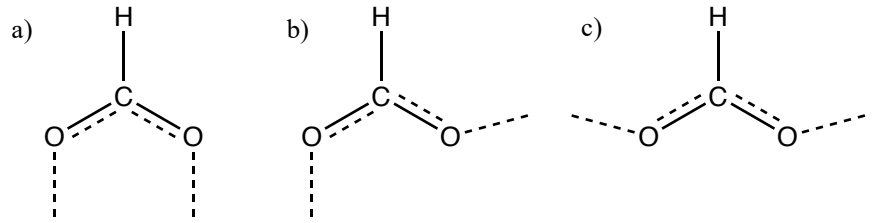


Figure 1.7. The three bridging modes of the formate ligand. a) *syn-syn*, b) *syn-anti* and c) *anti-anti*.

A popular combination are transition metals, specifically manganese (Mn), zinc (Zn), cobalt (Co), iron (Fe) and nickel (Ni), and formate ions, with some organic cation within the pores, with a $ATM(HCO_2)_3$ stoichiometry, and have been explored extensively for both ferroelectric and multiferroic applications [59-63]. Although not a transition metal, magnesium is a popular choice and has also been reported for ferroelectric applications [11, 12]. Incorporation of the formate ion has also shown promise for magnetocaloric applications, this is also true for when the oxalate ion is used as the organic linker [64, 65].

As mentioned previously, the formate ion ($HCOO^-$) is one of the most popular choices of organic linker to be incorporated into the X-site of a MOF with ABX_3 stoichiometry. Other ligands which have caught the attention of material chemists are the cyanide ligands, which is just one of many functional groups which has been exploited for incorporation into dense frameworks, others include azide- and alkyne- and cyano-functionalised groups, some for the effects the ligand has on the properties that are exhibited [66-72]. These are all monovalent anions and there are scarce examples of incorporating ligands with higher charges.

1.5 $NH_4M(HCO_2)_3$

The ammonium metal formate framework (AMFF) family have shown significant potential for their ferroic properties [11, 12]. They adopt the stoichiometry ABX_3 and are often found to have chiral hexagonal topology in comparison to the typically achiral perovskite structure other MOFs are known to adopt (see Figure 1.8). Formic acid,

although achiral itself along with other precursors which may be used, when bonded to metal centres chirality evolves from the handedness of the formate-metal-formate arrangement. This offers another route to chirality that does not require the use of enantiopure PBUs, another potential benefit to the formate.

With an abundance of hydrogen atoms on the NH_4^+ cation, this enables significant hydrogen bonding leading to polar order at 191 K – 255 K [59]. All paramagnetic AMFFs are reported to exhibiting weak ferromagnetism, and in all expect the Fe analogue, there was evidence of LRO spin-canted antiferromagnetism [59]. When cooled to below their characteristic T_C, 191 K – 254 K when **M** = Mn, Co and Zn, the ammonium cations undergo a disorder-order transition and ferroelectricity emerges as the cation becomes frozen in place by directional hydrogen bonds to the formate oxygen, hence order. The structural phase transitions leading to ferroelectricity in this family are all similar, but it will be described using the Zn analogue. Zinc is diamagnetic and this has no ferromagnetic properties but exhibits interesting ferroelectric properties. At 290 K it is chiral hexagonal and in non-polar space group $P6_322$, similarly to those mentioned above, with the ammonium ions along the *c*-direction of the hexagonal channels [60]. The disorder stems from competition between the ammonium and multiple H-bonding sites, as a result of thermal motion and the cation is constantly moving and rotating. This is also true for other members of this family. Cooling to 191 K induces a disorder-order transition where the ammonium ions become ordered and undergo a structural phase transition to polar space group $P6_3$, identical to the previously mentioned analogues, but interestingly at ~190 K there is tripling of the unit cell [60]. Dielectric measurements support this by showing anomalous dielectric peaks around this temperature, corresponding to said transition, alongside hysteresis loops below 190 K.

Diamagnetic $NH_4Mg(HCO_2)_3$ is also known to have dielectric properties with clear frequency dependency with the highest T_C, of 255 K, albeit only slightly higher than the Mn phase [11]. In a similar mechanism to the rest, at 255 K $NH_4Mg(HCO_2)_3$ undergoes a second order structural phase transition induced by the ordering of the ammonium ions from space group $P6_322$ to $P6_3$ [11]. Particularly interesting compared to others, is that it endures a 2-step freezing process, indicative of relaxor like behaviour [12]. During studies, there has been discussions on the dependence of the size and mass of

the $\mathbf{M}^{2+}$ with respect to the T_C. Initially it was thought that T_C decreases with a smaller radius of the $\mathbf{M}^{2+}$ ion, as discussed by Xu *et al* [61]. But the similar transition temperatures of $NH_4Mg(HCO_2)_3$ and $NH_4Mn(HCO_2)_3$ is a significant deviation from this as Mg^{2+} is considerably smaller than Mn^{2+}. Mączka *et al* [71] suggested that T_C increases with decreasing mass of **M** and increasing size of $\mathbf{M}^{2+}$. An alternative explanation would be that the smaller size of the Mg atom is compensated by its lower electronegativity [73]. This would lead to a greater degree of ionisation of the M-OCHO bond; the greater the negative charge on the formate oxygen then potentially leads to stronger hydrogen bonds.

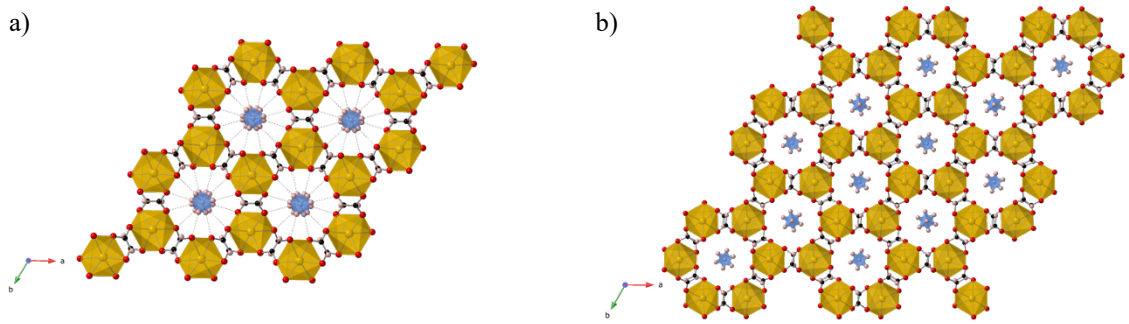


Figure 1.8. Structures of $NH_4Mg(HCO_2)_3$ at a) 295 K, b) 220 K. Yellow polyhedra: Mg atoms; O: red; C: black; H: pink and dotted lines in a represent hydrogen bonds in the ordered phase at 295 K. Images created using the CIFs from M. Mączka *et al* [11].

1.6 $AH^+Ln(HCO_2)_4$

If the decreased electronegativity of the B-site cation can be used to increase the temperature at which the A-site cation orders, another alternative would be to include lanthanide cations. The known examples of this case, the $AH^+Ln(HCO_2)_4$ frameworks, see Figure 1.9 for structures, which much like AMFFs, have potential in the field of ferroelectrics, ferromagnetism and multiferroics [74-78]. But unlike transition metal AMFFs (TM-AMFFs) which have been explored extensively, Ln-AMFFs studies are sparse despite this potential. The higher coordination numbers that lanthanides can possess mean that more variable coordination geometries can be adopted, and the +3 charge of the lanthanide results in one extra formate ligand within the system to charge balance the presence of the guest molecule, remembering that transition metals have a +2 charge in TM-AMFFs.

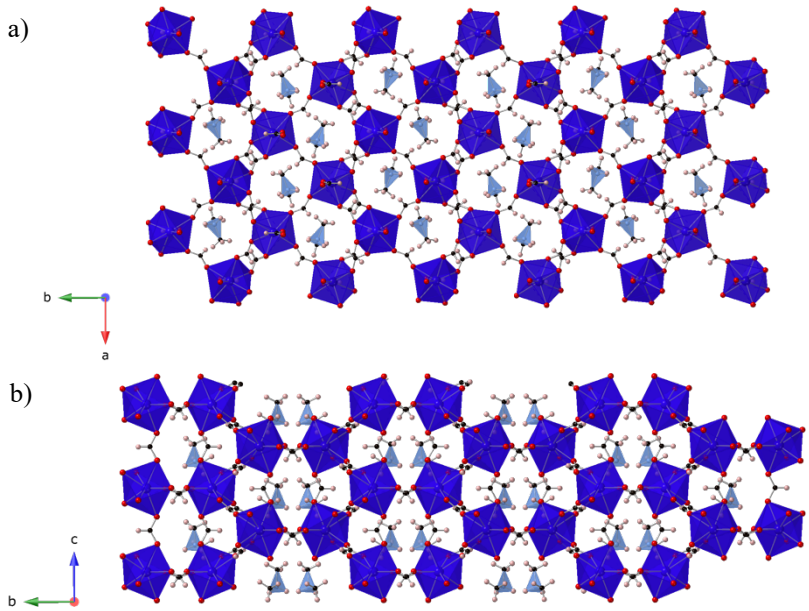


Figure 1.9. Crystal structures of $((CH_3)_2NH_2)Dy(HCO_2)_4$ along a) *c*-axis and b) *a*-axis. Depictions made from the structures reported by M. Ptak *et al* [77].

Lanthanides are also known for adopting acentric coordination environments [74]. Lui *et al* [74] suggested that the more acentric starting materials are employed into the system and the higher the possibility is that a chiral solid will crystallise out and consequently conducted a study making seven members of the $AH^+Er(HCO_2)_4$ family to explore this hypothesis. The guest molecules were all acentric amines, including ammonium (NH_4^+), methylammonium ($CH_3NH_3^+$), formamidinium ($NH_2CHNH_2^+$), guanidinium ($C(NH_2)_3^+$), imidazolium ($C_3H_5N_2^+$), ethylammonium ($CH_3CH_2NH_3^+$) and ethanolammonium ($HOCH_3CH_2NH_3^+$), all hydrogen-rich amine guest molecules with potential to induce ferroelectricity into the system. In all of these systems the Er^{3+} is in an 8-fold coordination geometry, but as the size of the amine gets larger, the coordination environment of Er^{3+} changes. For example, the smaller amines like NH_4^+, $CH_3NH_3^+$ and NH_2CHNH_2, the geometry of Er^{3+} adopts a square antiprism environment, with larger amines, $C(NH_2)_3^+$ and $C_3H_5N_2^+$, the Er^{3+} adopts a distorted square antiprism environment, and the largest, $CH_3CH_2NH_3^+$ and $HOCH_3CH_2NH_3^+$, results in Er^{3+} adopting a pentagonal bipyramidal environment [74]. An interesting point presented is that all amines possess hydrogen bonds between the amine groups and the anionic framework, displaying an ordered nature at room temperature. Furthermore, not only does this occur, the number of *syn-anti* bridging modes of the formate ion varies from two to none where all bridging modes become *anti-anti*. Unusually, incorporation of the two largest amines results in one chelating formate ion per structure, an occurrence which is not seen in transition metal formate frameworks

[60]. This supports the fact even more that the structure formed is highly dependent on the size of the guest molecule, and in this case the size of the amine and has huge structure directing effects. It is worth remembering also that the starting materials of these frameworks were all acentric and achiral yet crystallised into chiral architectures, but this is not the only study which has reported this phenomenon [78].

A similar duo of Ln-AMFFs are $[dmenH_2][Er(HCO_2)_4]_2$ and $[tmenH_2][Er(HCO_2)_4]_2$ and studied by Li *et al* [76]. Similarly to those reported by Lui *et al*, the relatively large amines resulted in no *syn-anti* bridging modes, and one chelating mode in $[tmenH_2][Er(HCO_2)_4]_2$. Interestingly, when $AH^+ = dmenH_2^+$ there is no phase transition, but when $AH^+ = tmenH_2^+$, at 203 K the cation undergoes an order-disorder phase transition which may result in the emergence of ferroelectricity and is also accompanied by a doubling of the unit cell [76, 78]. While there is significant interest into these Ln-AMFFs for potential as ferroelectric, ferromagnetic and synergetic multiferroic materials, a common application for lanthanide containing formate frameworks, as well as other hybrid lanthanide containing systems, is in luminescence [76, 79-81].

The architecture of lanthanide MOFs (Ln-MOFs) can go beyond employing a single linker, and in some complexes two ligands have been incorporated and give rise to structurally interesting materials, such as inclusion of dicarboxylate-based linkers for luminescence [82, 83]. A study in 1996 reports other porous mixed-ligand systems combing oxalate and carbonate, and oxalate and formate ligands, and is reported to be the first kind of lanthanide compounds which combine both oxalate and formate in a single system [84]. In a study reported by Vaidhyanathan *et al* [85], two amine templated lanthanide frameworks are explored, one which utilises only the oxalate ligand and the other which combines both formate and oxalate ligands [86]. The mixed-ligand oxalate formate system, $[NH_3CH_2CH(NH_3)CH_3]Nd(C_2O_4)_2(HCO_2)]\bullet H_2O$ has a 9-fold coordination geometry of the Nd, stemming from Nd connected to three oxalates creating a honeycomb-like network, and a fourth oxalate connecting the centres perpendicular to this, giving rise to a 3D system, and finally a single formate linker [85]. The two compounds reported possess dangling functional groups within the channels, which are believed to exhibit remarkable properties such as molecular recognition and chemical reactivity [85, 86]. Another example of a lanthanide

framework containing oxalate and formate ligands are *Ln*(C_2O_4)(HCO_2) frameworks, which lack A-site cations, see Figure 1.10.

The oxalate ligand is the simplest dicarboxylate and has often been overlooked due to the numerous advantages of employing a formate linker, but there is significant potential to be had by utilising it. This simplest dicarboxylate linker may represent an opportunity to obtain dense MOFs with an ABX_3 formula while incorporating the Ln^{3+} cation. Its relative size may enable it to be suitable to replace one formate linker, leading to a $AB(HCO_2)_2(C_2O_4)$ compound. This would open a new family of dense MOFs with potentially interesting ferroelectric and ferromagnetic properties to explore, possibly raising the ordering temperature of the former due to the greater strength of hydrogen bonding enabled by the lower electronegativity of the lanthanide.

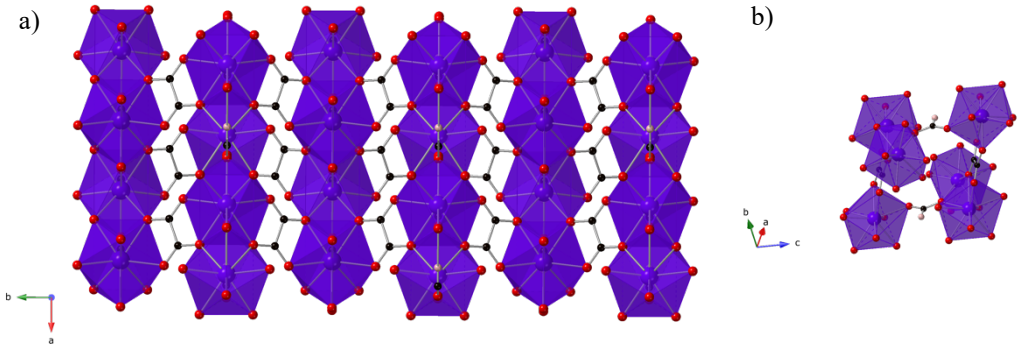


Figure 1.10. Crystal structures of porous Tb(C_2O_4)(HCO_2) displaying the mixed-ligand feature of both a) oxalate linkers and b) formate linkers. Produced from structures reported by C. Kittipong *et al* [87].

1.7 Project aims

There are two aims within this project, the first to probe whether disorder of the ammonium cation in the (NH_4)**M**(HCO_2)$_3$ family, where **M** = Mn and Zn and are known ferroelectric materials, remains below the characteristic transition temperature of these materials. This would provide an explanation for the frequency dependence of the dielectric spectroscopy. Single crystal neutron diffraction (SCND) can be exploited to obtain the structure of these materials at very low temperatures because unlike in X-ray diffraction, neutrons are sensitive to lighter elements, therefore the positions of the hydrogen atoms should be deduced using this technique. Combined with quasi-elastic neutron scattering (QENS) of these materials to study the dynamics that should be gone on sight into the ferroelectric ordering transition. Any disorder below the transition

temperature could be the cause of relaxor-like behaviour and an understanding of the structure-property relationship would provide significant insight into making new ferroelectric materials. Secondly, to create a synthetic route to obtaining a novel compound, (DMA)Er(C_2O_4)(HCO_2)$_2$, (DMA = $(CH_3)_2NH_2^+$), as the first example of a new family of dense MOFs with mixed oxalate and formate linkers with the aim of creating a framework with an A-site cation ordering at higher temperatures, highlighting a route to potential ferroelectric phases at ambient temperature. Alongside of achieving this, a family of other ALn(HCO_2)(C_2O_4)$_{1.5}$ frameworks have been made showing the versatility of how formate and oxalate anions can be combined to achieve new families of frameworks.

Chapter 2

Experimental Methods

2.1 Synthetic Procedures

2.1.1 $NH_4M(HCO_2)_3$

A double-layered diffusion technique was adopted for the synthesis of this family of AMFFs inspired by G-C. Xu *et al* [60]. In this method an 8 ml solution of the metal salts, namely metal perchlorates, were layered on top of an 8 ml solution containing ammonium formate and formic acid, the sources of the A-site cation ammonium and the formate ligands, respectively. All reactions were carried out in methanol dried over molecular sieve 4A initially, but due to reoccurring **M**$(HCO_2)_2 \cdot 2H_2O$ impurities in the obtained products, pre-dried methanol kept under argon was used for the remainder of the project. When **M** = Mn, a second impurity was present in initial syntheses, another polymorph of $NH_4Mn(HCO_2)_3$ but was typically omitted by the change in solvent [58]. The use of anhydrous metal chlorides could have been considered in order to try and reduce the presence of impurities; however, they are hydroscopic and rapidly convert to the hydrated species unless used in a glove box. The aim of the synthesis of $NH_4Mn(HCO_2)_3$ and $NH_4Zn(HCO_2)_3$ was to grow large single crystals as the route would permit for a single crystal neutron diffraction (SCND) experiment as well as multigram samples for a quasi-elastic neutron scattering (QENS) experiment. The Mn and Zn analogues of this family will hereafter be referred to as **1Mn** and **2Zn**. Both the reactions followed the general formula:

$$M(ClO_4)_2 \cdot xH_2O + NH_4CO_2H + 2HCOOH \rightarrow [NH_4]M[HCO_2]_3 + 2HClO_4 + xH_2O$$

$NH_4Mn(HCO_2)_3$

Single crystals of 1 mm^3 were obtained of **1Mn** with use of $Mn(ClO_4)_2 \cdot 6H_2O$ (0.1 M, reagent grade 99+ %, Acros Organics), NH_4CO_2H (0.8 M, 99 %, Acros Organics) and HCOOH (0.4 M, 98+ %, Acros Organics) all in methanol (16 ml, 99.9 %, Fisher Scientific). The crystals were harvested after 13 days and used for SCND. After optimisation of conditions, the same reagents yielded a pure phase of **1Mn** in the form of a white coarse powder (0.0626 g, 83.59 % yield) after 2 months using 0.045 M, 0.68 M, and 0.34 M solutions in pre-dried methanol (16 ml, 99.9 %, Alfa Aesar) of $Mn(ClO_4)_2 \cdot 6H_2O$, NH_4CO_2H and HCOOH, respectively. During this synthesis, the best efforts were in place to prevent the methanol from exposure to the air. An equally pure phase of **1Mn** (0.0996 g, 59.67 % yield) was also obtained after just 4 days with the same appearance using the same reagents and method as the latter by the following amounts, 0.1 M, 0.4 M and 0.2 M of $Mn(ClO_4)_2 \cdot 6H_2O$, NH_4CO_2H and HCOOH, respectively. A combination of multiple batches from these two methods were used to make a sample for the QENS experiment with a mass of 1.7975 g. However, due to recurring issues with the formation of $Mn(HCO_2)_3 \bullet 2H_2O$ during some of the batches when scaling up the reaction to yield multigram samples for QENS, a technique inspired by I. E. Collings *et al* [88] was adopted to post synthetically purify **1Mn**. This involved soaking **1Mn** in a 1:5 molar ratio solution of **1Mn**:ammonium formate in 20 ml methanol and stirring overnight, for approximately 20 hours.

$NH_4Zn(HCO_2)_3$

A pure phase of **2Zn**, a white coarse powder, (0.2694 g, 77.06 % yield) was obtained after 21 days using $Zn(ClO_4)_2 \cdot 4H_2O$ (0.2 M, 98 %, Alfa Aesar), NH_4CO_2H (2.4 M, 99 %, Acros Organics) and HCOOH (0.8 M, 98+ %, Acros Organics) in pre-dried methanol packed under argon (16 ml, 99.9 %, Alfa Aesar). These conditions were scaled up to 40 ml of pre-dried methanol for a QENS experiment, where 2.3702 g was used. A very large single crystal of 4 mm^3 was obtained using the same reagents but with the following conditions, 0.2 M, 2.4 M and 0.8 M of $Zn(ClO_4)_2 \cdot 4H_2O$, NH_4CO_2H and HCOOH, respectively and used for SCND.

2.1.2 $((CH_3)_2NH_2)Ln(C_2O_4)_x(HCO_2)_y$

Initially, the double-layer diffusion technique was adopted in order to attain a synthetic route at ambient conditions, in which the lanthanide salt, namely lanthanide nitrates, were layered on top of solutions of oxalic acid, formic acid and dimethylamine, all in methanol (16 ml, 99.9 % Fisher Scientific). This was to avoid relying on the decomposition of the solvent dimethylformamide (DMF) to produce formate ions and dimethylammonium (DMA), ($(CH_3)_2NH_2^+$ = DMA). However, numerous attempts via ambient conditions were unsuccessful therefore solvothermal synthesis was utilised for the remainder of the project. Mixed-ligand MOFs are rarer than MOFs with only a single ligand, especially those containing both the oxalate and formate ligands, so the aim here was to study the structural possibilities that these systems offer, as well as exploring the potential physical properties. Two different families of these materials were studied, the first containing only one member: $((CH_3)_2NH_2)Er(C_2O_4)(HCO_2)_2$, hereafter referred to as **1Er**. The second containing 4: $((CH_3)_2NH_2)Ln(C_2O_4)_{1.5}(HCO_2)$ where *Ln* = Tb, Dy, Ho and Er, hereafter referred to as **2Tb**, **3Dy**, **4Ho and 5Er**.

$((CH_3)_2NH_2)Er(C_2O_4)(HCO_2)_2$

1Er (0.3439 g, 87.85 % yield) was synthesised by solvothermal synthesis using $Er(NO_3)_3{\cdot}5H_2O$ (0.4432 g, 1 mmol, 99.9 %, Acros Organics), dimethylamine (3 mmol, 33 wt% in ethanol, Sigma Aldrich), oxalic acid (0.0902 g, 1 mmol, 98 %, Acros Organics) and sodium carbonate (0.0210 g, 0.2 mmol, 99.5 %, Acros Organics) in a 1:1 ratio of water:DMF (DMF: 3 ml, >99 %, Fisher Scientific) with a total volume of 6 ml and placed in a Teflon-lined autoclave. This was heated at 100 °C for seven days and yielded a pale pink fine powder.

$((CH_3)_2NH_2)Ln(C_2O_4)_{1.5}(HCO_2)$

2Tb, a white fine powder, (1.3899 g, 83.67 % yield) was synthesised using $Tb(NO_3)_3{\cdot}5H_2O$ (1.9697 g, 1 mmol, 99.99+ %, Acros Organics) and oxalic acid (0.5874 g, 1.5 mmol, 98 %, Acros Organics) in DMF (39.1 ml, >99 %, Fisher Scientific) and heated at 150 °C for 48 hours in a 100 ml glass jar and Teflon lid. **3Dy**, a pale-yellow fine powder, (1.5461 g, 92.21 % yield) was synthesised similarly to **2Tb**, with $Dy(NO_3)_3{\cdot}5H_2O$ (1.9065 g, 1 mmol, 99.9 %, Alfa Aesar) and oxalic acid (0.5867 g) but

with additional dimethylamine (2 mmol, 33 wt% in ethanol, Sigma Aldrich). **4Ho**, a pale-yellow fine powder, (1.5867 g, 94.05 % yield), was synthesised similarly to **3Dy**, with $Ho(NO_3)_3 \cdot 5H_2O$ (1.9175 g, 1 mmol, 99.9 %, Alfa Aesar), oxalic acid (0.5867 g) and dimethylamine. **5Er**, a pale pink fine powder, (0.3356 g, 92.36 % yield) was obtained similarly to **3Dy** and **4Ho**, using $Er(NO_3)_3 \cdot 5H_2O$ (0.4430 g, 1 mmol, 99.9 %, Acros Organics), oxalic acid (0.1347 g) and dimethylamine, however in this case, in a 25 ml glass jar and 9 ml of DMF. Further reactions to obtain **5Er** took place to scale up the reaction, and therefore the yield, which involved a similar method but employing a 100 ml glass jar and 39.1 ml of DMF with a similar scale up of the amount of reagents used, resulting in similar conditions to **2Tb**, **3Dy** and **4Ho**.

2.2 X-ray Diffraction

X-rays have a wavelength of ~ 1 Å (10^{-10} m) and are placed between γ-rays and the ultraviolet region of the electromagnetic spectrum. X-rays are produced when high energy particles collide with matter, specifically when electrons are accelerated by a potential difference of ~ 30 kV and hit a metal target [29]. The spectra produced is made up of two components: white radiation, a broad spectrum of wavelengths, and monochromatic wavelengths, or fixed wavelengths. In an X-ray tube, electrons are accelerated by a high potential difference, typically ~30kV, emitted from an electrically heated filament which is typically made of tungsten (W) and collide with a metal target, commonly copper (Cu) or molybdenum (Mo) fixed to an anode. These high energy incident electrons ionise the K shell (1s) electrons and higher L shell (2p or 3p) electrons immediately drop down to fill the vacancy emitting X-rays as a consequence. This leads to a series of sharp peaks in the X-ray spectrum, referred to as the Kα and Kβ lines, which result from the 2p to 1s and 3p to 1s transitions, respectively. The Kα lines have characteristic wavelengths of 1.5418 Å and 0.7107 Å for Cu and Mo respectively [13, 29]. The Kα line occurs much more frequently than Kβ and is a doublet due to the different energies of the different spin states of the 2p electron giving rise to Kα_1 and Kα_2 [29]. Kβ can also be filtered out by two mechanisms, the first by using a thin metal foil of atomic number – 1 (Z-1). Or a single crystal, usually of graphite, can be used to reflect the beam producing monochromatic beam of X-rays, from which Kα_2 radiation has also been removed if the single crystal is used on the primary beam [13].

Diffraction takes place when incident light's wavelength is the same order of magnitude of spacings between the arrays of atoms in a crystalline solid, see Figure 2.1. Diffraction of X-rays only occurs when constructive interference is satisfied; constructive interference is when the maxima of two waves are in phase and can be added together so the resultant wave is the same as the individual waves but possesses a larger amplitude, twice that of the sum of the individual waves. Lawrence Bragg developed an equation to represent the spacing between the crystal planes and the angle in which the reflections occur.

$$n\lambda = 2d_{khl}sin\theta \qquad \text{(Equation 2.1)}$$

n is an integer and represents the order of the reflections, for example n = 1 is a first-order reflection, n = 2 is a second-order reflection and so on. Most commonly, n is treated as 1. λ is the wavelength, *hkl* are the Miller indices of the parallel planes, *d* is the spacing between the parallel planes and θ is the angle of incidence, or more famously, the Bragg angle [13]. Constructive interference leads to sharp peaks known as Bragg peaks or Bragg reflections. There are two types of X-ray diffraction, single crystal and powder which are discussed below.

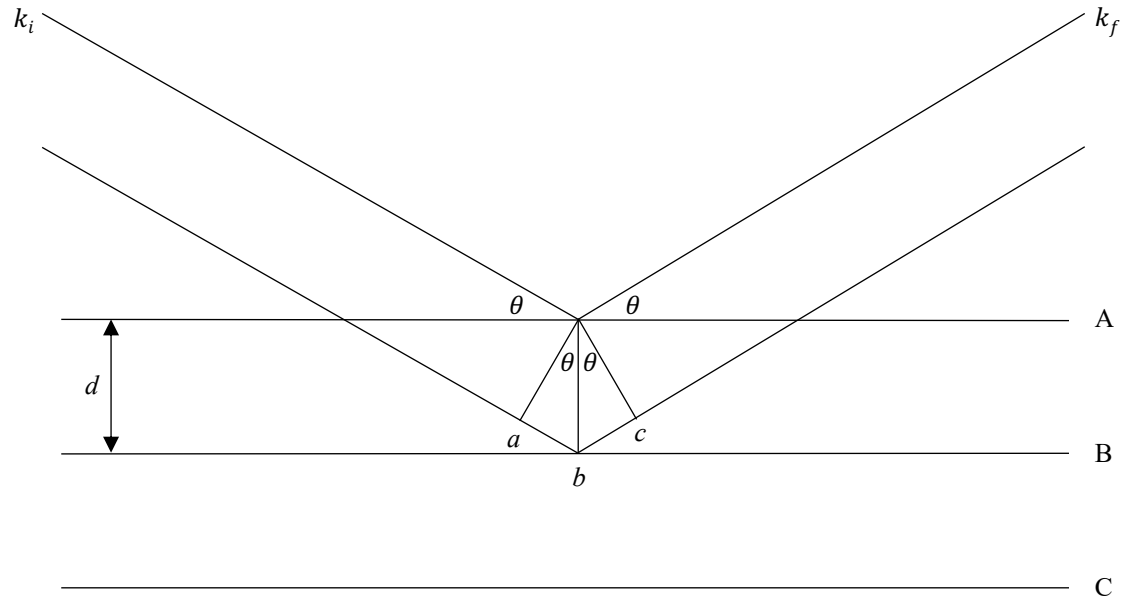


Figure 2.1. Derivation of Bragg's Law. k_i and k_f are the incident and final momentums of the neutron, respectively.

2.2.1 Single Crystal X-ray Diffraction

Single crystal X-ray diffraction (SCXRD) is an extremely valuable technique that enables the structure of a crystal to be determined by measuring the positions and intensities of the *hkl* reflections produced during the data collection. This information,

which resolves *hkl* reflections by crystal orientation can be thought of as a 3D dataset, can be used to determine the space group and unit cell and positions of the atoms in the crystal. This allows the identity of the crystal to be uncovered if the reflections are measured and indexed properly. The X-ray form factor is how effective an atom is at scattering X-rays, and a system possessing more electrons will scatter the X-rays much more strongly. This scattering factor is directly proportional to the atomic number for neutral atoms, but it is also dependent on the Bragg angle [13].

There are two most well-established methods for solving single crystal data: the Patterson method and Direct Methods. The former is typically used for when the structure has at least one heavy atom. The latter is typically employed when all the atoms in the structure have similar scattering properties, meaning similar atomic numbers, and is able to calculate an electron density map of the unit cell through the probabilities of the phase values [13]. A set of structure factors are established and are compared with the observed structure factors, F_{calc} and F_{obs} respectively. If a reasonable model is achieved, atomic positions and displacement parameters are refined using the Least Squares Method, which minimises the sum of squares of the difference between F_{calc} and F_{obs} for all reflections to determine the best fit. Displacement parameters are a measure of the displacement of atoms from their ideal crystallographic sites, including thermal motion, and can be refined isotropically or anisotropically. If refined isotropically, the atomic displacement is assumed to the spherical but if refined anisotropically, the atoms appear as ellipsoids, allowing non-spherical displacement.

The quality of the refinement is given as a R_1-factor which represents the difference between the observed and calculated structure factors. Lower value of R_1 means smaller differences between observed and calculated intensities therefore a better structure model.

$$R_1 = \frac{\sum |(|F_o| - |F_c|)|}{\sum |F_o|} \qquad \text{(Equation 2.2)}$$

Where F_o and F_c are the observed and calculated structure factors, respectively [13]. Two other refinement statistics are generated: wR_2 (weighted R-factor) and (S) the Goodness of Fit, see Equations A.1-3 in the appendix for definition.

Single crystal structure determinations were carried out using a dual source Rigaku Oxford Diffraction Supernova equipped with Mo Kα and Cu Kα, β micro-focus sources (0.8 kV, 50 mA) with multi-layered focusing optics and an Atlas S2 CCD detector. Samples were cooled, when required, using an Oxford Cryostreams cryostream with samples held on MiTeGen micro loops. Data were integrated and absorption corrections performed using CrysAlisPro software suite version 171.38.41 using direct methods in SHELXS or SHELXT or charge density methods in olex.2 and least-squares refinements carried out using SHELXL-2014 via the Olex2 graphical user interface (GUI) [89-94]. Note, the 100 K data for **2Tb** was solved using the APEX3 interface [95].

2.2.2 Powder X-ray Diffraction

Powder X-ray diffraction (PXRD) can be used for phase identification of a bulk polycrystalline material. It can give information on the crystal structure of a material, but also for following solid state reactions, as well as acting as a method to test a sample for phase purity. Using PXRD as a test for phase purity is simple yet effective, simply by comparing the PXRD pattern obtained to the Crystallographic Image File (CIF) of a known crystal structure, it can be determined whether the bulk phase matches the structure determining single crystal. It is difficult to identify phases with unknown structures using PXRD. This is because of the reduction of information obtained from collecting diffraction data from a single crystal to a collection of arbitrarily arranged polycrystals makes solving structures from powder diffraction challenging. PXRD is highly valuable for refining high symmetry structures, but for lower symmetry systems the pattern becomes more complex by containing numerous overlapping lines which are difficult to index [13].

The powdered sample has crystallites orientated in every possible direction to one another and when subjected to a monochromatic beam of X-rays, those which satisfy the Bragg angle, will cause the X-rays to diffract [13, 29]. If the crystallites within the powdered sample are not all randomly orientated then preferred orientation occurs, where certain *hkl* values are favoured and consequently result in more intense Bragg peaks. Although some compounds have the same crystal structure, they will give different diffraction patterns due to differences in unit cells. Changes in the lattice

parameters will affect peak position while changes in composition effect peak intensity. Crystalline materials will produce sharp Bragg peaks whereas amorphous materials will result in broad and diffuse Bragg peaks.

Two main refinement methods will be discussed here: Rietveld and LeBail. Rietveld can be used to refine crystal structures from PXRD data, while LeBail refines the unit cell and peak shape parameters. Both of these methods require the use of a starting model of the structure or a closely related material to commence refinements from. The former, the Rietveld method, involves the interpretation of the lines' intensities from known atomic coordinates and peak positions from the lattice parameters and space group. Low symmetry systems have a higher number of peaks compared to higher symmetry systems, which as mentioned previously, result in overlapping lines on the diffraction pattern. To overcome this problem the Rietveld method involves overall line profile analysis [13]. This method was originally formulated for neutron powder diffraction data and H. M. Rietveld [96] published introducing a number of parameters which could be refined using this method that were dependent on instrumental and experimental factors such as peak shape, peak width and preferred orientation.

A calculated pattern is created using an initial structure which is compared to the experimental pattern where the difference between the two is represented by a line beneath the two patterns. The structure is altered accordingly, and parameters are modified and refined until a fit is obtained which minimises the difference and maximises the agreement between the calculated model and experimental patterns, this is called the R-factor. The R-factor is a measure of precision and not accuracy. Refined parameters include atomic positions, occupancies, displacement parameters and phase scale in addition to the instrumentally determined parameters mentioned above. Care must be taken in the way in which the refinement is performed to avoid a false minimum [29]. During the refinement, three outputs are generated, R_p (profile), R_{wp} (weighted profile, which adjusts for the relative intensity of reflections) and χ^2 which represent the goodness of fit between the calculated pattern and the observed pattern, in other words, the quality of the refinement. χ^2 and R_{wp} are defined in Equations A.4-6 in the appendix. R_p is defined by:

$$R_p = \frac{\sum(I^{obs} - I^{calc})}{\sum I^{obs}} \text{ x } 100\ \% \qquad \text{(Equation 2.3)}$$

The aim is to minimise these values as much as possible, as the lower the value, the better the fit of the refinement is. The Rietveld method involves a least squares refinement method, and is represented by the function which *M* can account for the overall profile refinement, including those with overlapping peaks:

$$M = \sum_i W_i \{y_i(obs) - \frac{1}{c} y_i(calc)\}^2 \qquad \text{(Equation 2.4)}$$

where Σ_i is the sum of the independent observations, *W* is a halfwidth parameter, y_i is the fractional coordinate on *i*th atom in the asymmetric unit and *c* is the overall scale factor [96]. *M* must be minimised as far as possible with respect to the other parameters.

LeBail fits are a modification of the Rietveld method, which is also referred to as profile matching or pattern matching and typically has fast refinement cycles. No atomic positions are used, and the calculated intensities of the individual peaks are simply optimised to best fit the data [97]. As for the Rietveld method, unit cell parameters and space group are used to determine where Bragg reflections will be observed. Equation 2.5 describes how the reflection intensities are determined using this method:

$$I_K(obs) = \sum_j \{w_{j\cdot K} \cdot S_K^2(calc) \cdot y_j(obs)/y_j(calc)\} \qquad \text{(Equation 2.5)}$$

where $I_K(obs)$ is the integrated intensity which is related to $w_{j\cdot K}$ which is the contribution of the Bragg peak at $2\theta_K$, to the profile y_j at $2\theta_j$. Initially, all equal $S_K^2(calc)$ are used in this equation, instead of the structure factors from atomic coordinates, which subsequently generates a $I_K(obs)$ value which is reinserted into the equation as the new $S_K^2(calc)$ value in the next iteration and successive step meaning the intensities are determined after each refinement cycle.

Powder diffraction in the context of this project was used to assess sample purity and were collected using a Rigaku Miniflex utilising Cu Kα radiation (40 kV, 15mA) and D/teX Ultra detector. Patterns were collected in reflection geometry with the samples mounted on zero background Si wafer plates, over a range of 5-60° 2θ, at a rate of 2°/minute with a step size of 0.02. Overnight scans were collected when a pure phase was optimised using a X'pert^3 PANalytical powder diffractometer utilising Cu Kα raditation, (40 kV, 40 mA) and a X'celerator Scientific detector, over a range of 5-80°

2θ. These scans were collected to obtain higher resolution diffraction patterns of pure phases used for most refinements, carried out using the Rietica software, version 4.0 [98].

2.3 Neutron Diffraction

Neutron diffraction (ND), or elastic neutron scattering (ENS), is a technique which only occurs at a restricted number of facilities around the world due to the high cost and the way in which neutrons are generated. Neutrons can be produced by spallation, involving firing high-energy protons at a metal target and unlike in X-ray diffraction where characteristic peaks are observed (see Section 2.2), neutrons produce a continuous spectrum of radiation [13]. Compared to X-ray sources the resultant beam is typically weak. Spallation sources can be used for time-of-flight analysis where all the wavelengths of a neutron are used with a fixed diffraction angle, θ, but each wavelength is dependent on the velocity of the neutron. This enables the neutrons to be separated out by their time of flight and wavelength which is represented by the de Broglie equation:

$$\lambda = h/mv \qquad \text{(Equation 2.6)}$$

where λ is the wavelength, h is Planck's constant (6.626 x 10^{-34} m^2 kg s^{-1}), m is the mass of a neutron (1.675 x 10^{-27} kg) and v is the velocity of the neutron [29]. This is comparable to other diffraction methods in which λ is fixed and d and θ vary.

As mentioned previously, neutrons are more sensitive to hydrogen atoms than X-rays are. This stems from the scattering power being a function of the atomic nuclei rather than the number of electrons. However, the relationship between atomic number and scattering power is not as straight forward as the relationship between number of electrons and X-rays, and there is no dependence on $\sin\theta/\lambda$ [13]. Neutron diffraction is also a valuable tool in studying the magnetic structure of a material since neutrons possess a magnetic dipole moment so are also diffracted by unpaired electrons [29]. The low intensity of neutron beams and weaker interactions between neutrons and matter require larger samples than X-ray diffraction experiments require, typically 1 cm^3 in all dimensions of a single crystal or a multigram powdered sample [29]. Bond lengths are also more accurate when utilising neutron diffraction as the process involves the atomic

nuclei so will give the true distance whereas in X-ray diffraction, it is based around the electron clouds [13].

2.3.1 Single Crystal Neutron Diffraction

The relatively large single crystals needed to a neutron diffraction experiment can cause issues as it is quite difficult to grow single crystals of 1 mm^3, a minimum size for modern instruments, even where X-ray quality crystals of a material are available. If sufficiently large single crystals are not able to be obtained, multiple smaller crystals can be aligned to increase the surface area which the beam is exposed to. As mentioned previously, neutron diffraction is a valuable technique crystallographically to determine the positions of light atoms due to the scattering power as a function of atomic nuclei, so is very effective in precisely locating hydrogen atoms and has been used for this purpose in this thesis.

Single crystal neutron diffraction studies were carried out using the single crystal diffractometer (SXD) in TS1 at ISIS at the Science and Technology Facility Council, Oxford [99, 100]. Three single crystals of $NH_4Mn(HCO_2)_3$ 1 mm^3 in size were aligned underneath aluminium tape and placed in the beam. Data was collected at 22 K, cooled using a He^3 cryostat and measured under zero field. A total of seven orientations: 10°, 50°, 90°, 130°, 180°, 220° and 310°, were collected with a 1 cm by 1 cm beam exposure to the sample and a current of 2500 µA. Data for **2Zn** was collected using SXD also, with the time-of-flight Laue method. The sample was cooled to 20 K in a closed circle cryorefrigerator under He atmosphere and data were collected at eight static orientations: 10°, 50°, 90°, 130°, 200°, 240°, 290° and 330°, with a counting time per orientation of ~8 hours for each orientation. Diffraction spots were indexed initially with unit cells available from X-ray measurements at 100 K confirming no change in crystal structure down to 20 K. Bragg intensities were extracted using the 3D-profile fitting method implemented in the SXD2001 software and corrected for the Lorenz effect, no absorption correction was applied for the shape of the crystal [101]. Data was solved using SHELXS or SHELXT or direct methods and refined using SHELXL-2014 via the Olex2 GUI [89, 90, 92, 93].

2.4 Neutron Scattering

There are three types of neutron scattering: inelastic, elastic and quasi-elastic (INS, ENS and QENS, respectively). ENS is the same as diffraction, as discussed in Section 2.2 and occurs when neutrons are scattered without changing the energy, see Figure 2.2. INS involves an energy transfer between the incident neutrons and the sample alongside a change in the direction in which the neutrons are travelling, so the neutrons which are not absorbed by the sample have a different kinetic energy to the incident neutrons [102]. The sample gains the energy from the incident neutrons and can undergo a transfer from the lower energy state to a higher energy state. The reverse occurs when the sample loses energy. This energy transfer results in magnetic and vibrational transitions but, unlike other techniques such as Infrared Spectroscopy (IR) and Raman, there are no selection rules rendering all the vibrations active. Vibrations involving ^{1}H atoms will dominate due to the much higher scattering cross section of this isotope.

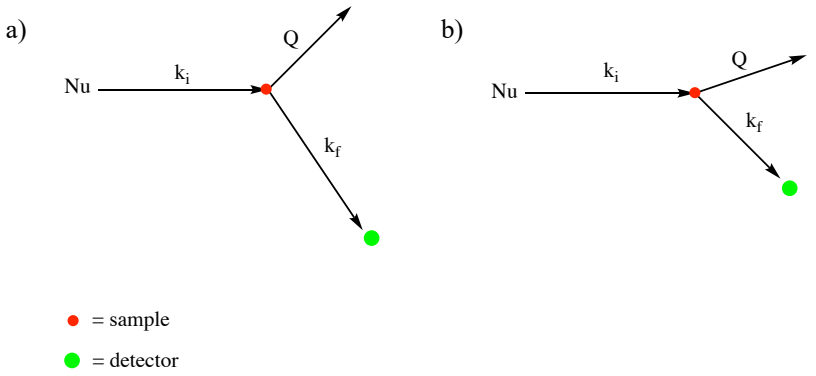


Figure 2.2. a) elastic neutron scattering and b) inelastic neutron scattering. k_i and k_f show the momentum of the incident and final neutrons, respectively, and Q is the momentum transfer. In a) $E_i = E_f$ while in b) $E_i \neq E_f$, where $E_{i,f}$ are the incident and final energies.

The neutron has a wavelength, λ, which is related to the momentum, k, by $k = 2\pi/\lambda$. $Q = k_i - k_f$ and for elastic scattering: $E_i = E_f$ and for inelastic scattering: $E_i \neq E_f$ [102].

QENS is a type of inelastic scattering but there is only a very small energy change compared to the energy of the incident neutrons. The elastic line has a tendency to broaden as a result of rotational motion or translation of the centre of masses in atoms within the material, and QENS is used to probe this type of energy exchange. The specific geometry of motion, such as rotations of particles is referred to as the Elastic

Incoherent Structure-Factor (EISF) and is the quasi-elastic intensity within the purely elastic peak and is represented by the ratio:

$$A_0(Q) = \frac{I^{el}(Q)}{I^{el}(Q) + I^{q}(Q)} \qquad \text{(Equation 2.7)}$$

Where $A_0(Q)$ is the ratio of quasi-elastic to elastic (the EISF) and $I^{el}(Q)$ and $I^{q}(Q)$ are the integrated intensities of the elastic and quasi-elastic sections of the spectra, respectively [103].

QENS was conducted using OSIRIS on TS1 at ISIS at the Science and Technology Facility Council, Oxford and is a high resolution quasi- and inelastic neutron scattering spectroscopy instrument [104, 105]. For the $NH_4Zn(HCO_2)_3$, the sample was cooled to 5 K, where a resolution function for the (002) graphite monochromator configuration using the Be filter was collected. The elastic scans began at 10 K up to 300 K in 10 K increments and a current of 30 μA. Long runs were then collected at 150 K, 160 K, 170 K, 190 K, 200 K, 210 K and 250 K with a current of 360 μA each. A second resolution function was obtained at 100 K for the (004) graphite monochromator and long scans collected at 170 K, 190 K, 200 K, 210 K, 240 K, 270 K and 300 K. For the $NH_4Mn(HCO_2)_3$ sample a resolution function for the (002) setting was collected at 10 K, and elastic scans obtained from 10 K to 340 K at 10 K increments. Long scans were then collected at 170 K, 200 K, 220 K, 240 K, 260 K, 280 K and 310 K. Finally a second resolution function for the (004) setting of monochromator were obtained at 100 K for the $NH_4Mn(HCO_2)_3$ and long scans collected at: 200 K, 220 K, 240 K, 260 K, 280 K, 310 K and 340 K. Data were reduced and processed using MantidPlot, version 4.1.0 [106].

An X'press measurement was collected on the INS spectrometer TOSCA on TS1 at ISIS at the Science and Technology Facility Council, Oxford also to assist with identifying the composition of the mixed-ligand lanthanide MOFs [107, 108]. This measurement was performed at < 20 K using an aluminium cell and the spectrum was collected over a 3 hour scan and data were presented using OriginLab [109].

2.5 Superconducting Quantum Interference Device (SQUID)

A SQUID magnetometer can be used to measure the magnetic susceptibility of a material. It consists of two superconducting loops connected by two Josephson junctions, also called “weak links”, see Figure 2.3 [110]. These are insulating and parallel to one another and allow Cooper pairs of electric passes through from one superconducting loop to the other via quantum tunnelling. A magnetic field induced from the sample is applied perpendicular to the ring, inducing a supercurrent which in turn gives rise to a phase difference between the two currents, left and right, penetrating the two Josephson junctions. An interference of these two currents causes an oscillation as a function of the applied field and a magnetic flux, ϕ, arises enabling magnetic fields to be measured [110]. The threshold of magnetic field which a SQUID can detect are so small, it can be used to detect neural activity in the brain [111].

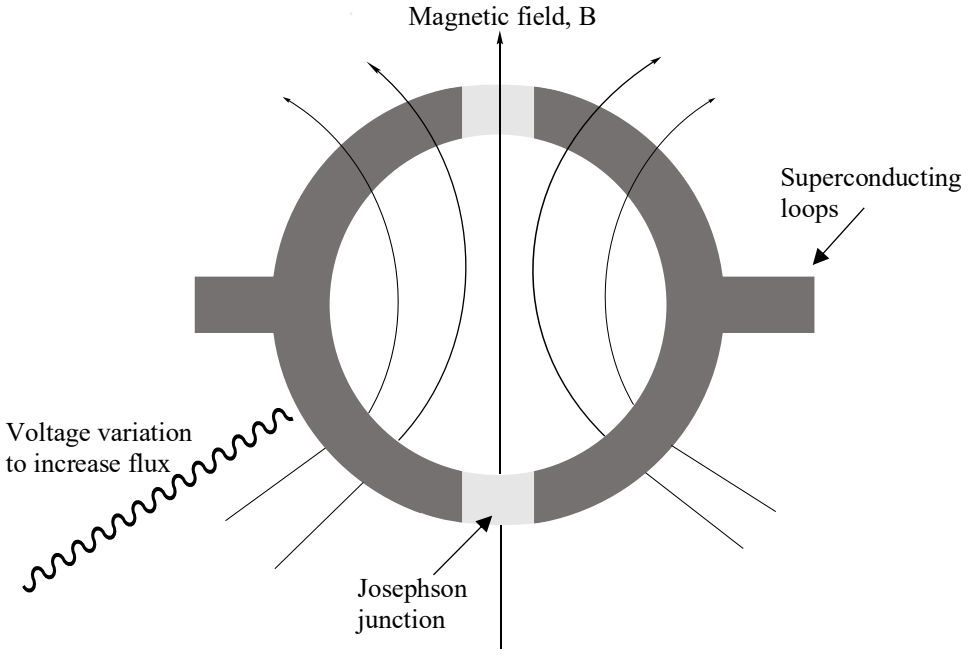


Figure 2.3. Basic principle of a SQUID.

Field-cooled (FC) measurements involve cooling the material to a base temperature in the presence of an applied field, and magnetic susceptibility measurements are taken on warming. Whereas during zero-field-cooled (ZFC) measurements, there is an absence of an applied field on cooling the material to a base temperature, the field is then applied, and the magnetic susceptibility is measured on warming.

Direct Current (DC) SQUID measurements were collected using Quantum Design's Magnetic Property Measurement System (MPMS) using the MPMS MultiVu application [112, 113]. A field-cooled (FC) and a zero field-cooled (ZFC) measurement was taken, using an applied field of 1000 Oe between 2 K and 300 K. Then hysteresis measurements were obtained at 2 K and cycled between ~ -50 kOe and ~ 50 kOe.

2.6 Thermogravimetric Analysis and Differential Scanning Calorimetry (TGA-DSC)

Thermogravimetric Analysis (TGA) is used to determine the thermal properties and stability of a material as is typically used to determine at what temperature it decomposes. When combined with Differential Scanning Calorimetry (DSC) it will reveal whether the decomposition was exothermic or endothermic by measuring the heat content of both a reference and a sample, represented as a peak or trough respectively [114].

TGA-DSC was carried out simultaneously using a NETZSCH 409 PG/PC TGA. The sample was held in a ceramic crucible and heated under flowing N_2 at a rate of 10 or 20 K/minute from 20 ^oC or 25 ^oC to 600 ^oC. **4Ho** was held at standby at 30 °C for 30 minutes to study if any remnant surface water evaporated. Both the sample and reference crucible are heated simultaneously, and the percentage weight loss is measured as a function of temperature which is set to increase at a given rate up to an instructed temperature limit.

2.7 Infrared Spectroscopy (IR)

IR Spectroscopy produces a spectrum containing information regarding the vibrations or rotations of bonds within molecules, with wavenumber (cm^{-1}) occupying the x-axis and the percent of transmittance (%T) on the y -axis. However, not all bonds are IR active, as there must be a change in the energy due to the motions. For example, diatomic homonuclear species are not IR active as there is no change in the dipole moment [114]. Each vibrational, which occur in the form of bends or stretches, or rotational motion of particular bonds have characteristic wavenumber at which the peak will be appear.

IR spectra were collected over a range of 500-4000 cm^{-1} using a Shimadzu IRAffinity-1S Fourier Transform Spectrometer equipped with an attenuated total reflection stage. Measurements were averaged over a total of 32 scans and a resolution of 4 cm^{-1}.

Chapter 3

Neutron Scattering from $NH_4M(HCO_2)_3$ Frameworks

The primary goal set in place for the isostructural $NH_4M(HCO_2)_3$ Metal-Organic Frameworks (MOFs) was to probe any disorder of the ammonium (NH_4^+) cation below the structural transition temperature. Single crystals of sufficient size were successfully synthesised for single crystal neutron diffraction of the Mn (**1Mn**) and Zn (**2Zn**) members of this series, as well as pure bulk phase for quasi-elastic neutron scattering (QENS). As discussed in this chapter these techniques suggest a lack of static disorder in these materials but clear dynamical disorder in the low temperature phase was indicated by QENS.

3.1 Powder X-ray Diffraction

Figure 3.1 displays the purity of **2Zn**, and the conditions used to obtain this phase were used from hereafter to obtain phase pure multigram samples used for further analysis, such as QENS. (See Section 2.1.1 for synthetic details)

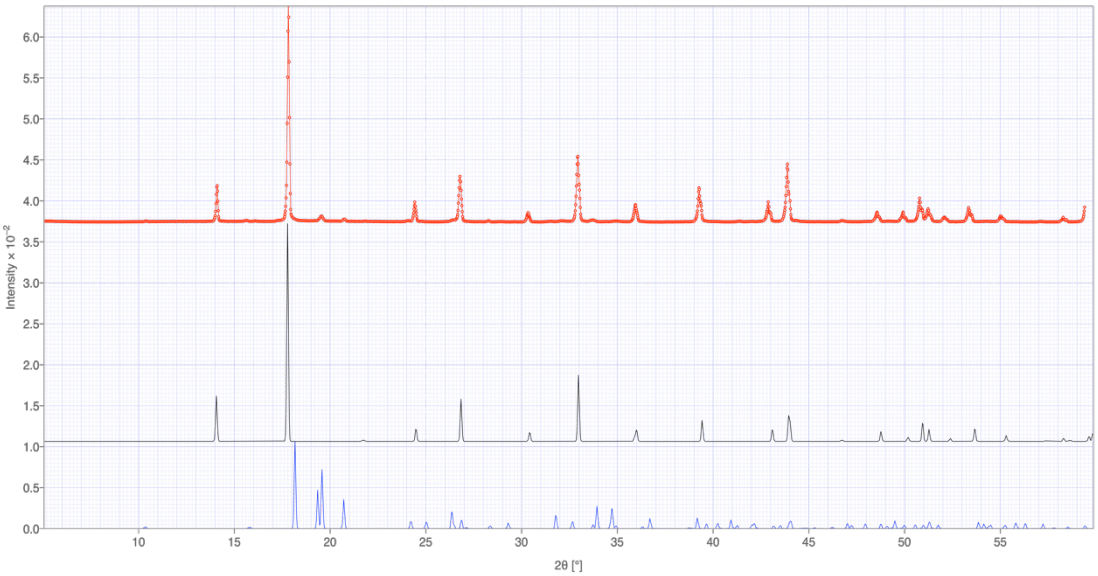


Figure 3.1. Powder X-ray Diffraction (PXRD) pattern obtained of the pure phases of **2Zn**. Black: CIF of **2Zn**, red: PXRD pattern of pure phase and blue: CIF of zinc formate dihydrate.

Figure 3.2 shows the PXRD patterns obtained of the pure phases of **1Mn** with conditions which were used to obtain samples for further synthesis and analysis, including QENS. When repeating reactions using the conditions which yielded phases as seen in Figure 3.2, the products obtained were at a lower level of purity containing vast amount of impurities, a combination of manganese formate dihydrate and a second polymorph of **1Mn**. This is thought to be due to increased water in the reaction, possibly due to aging of the formic acid reagent solution. A Post-Synthetic Purification (PSP) procedure was therefore attempted (see Section 2.1.1) in order to purify these samples for QENS. The patterns of before and after PSP are displayed below in Figures 3.3 and 3.4, respectively.

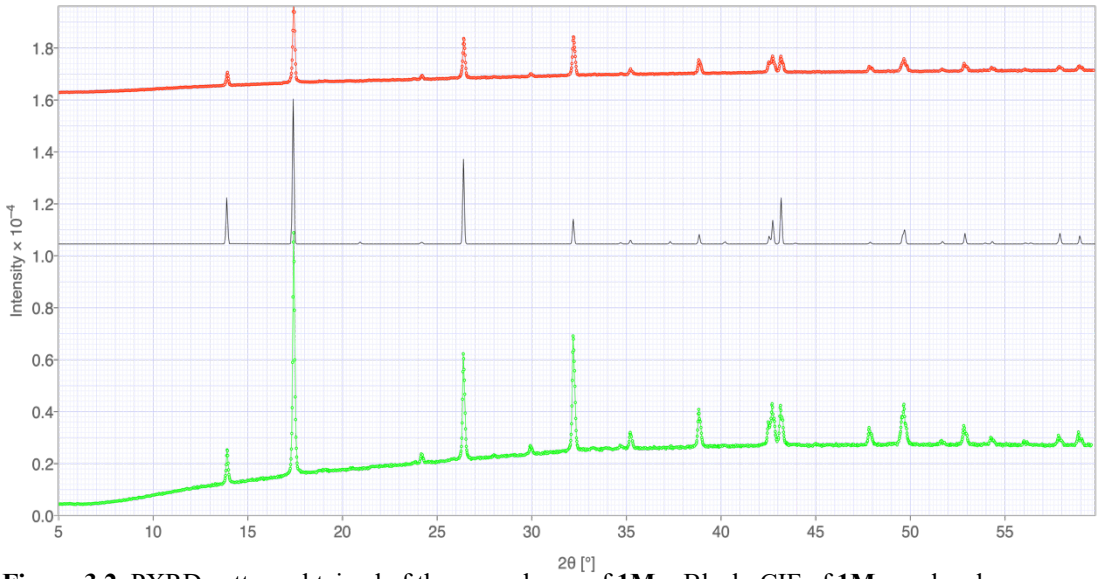


Figure 3.2. PXRD pattern obtained of the pure phases of **1Mn**. Black: CIF of **1Mn**, red and green: PXRD pattern of pure phases.

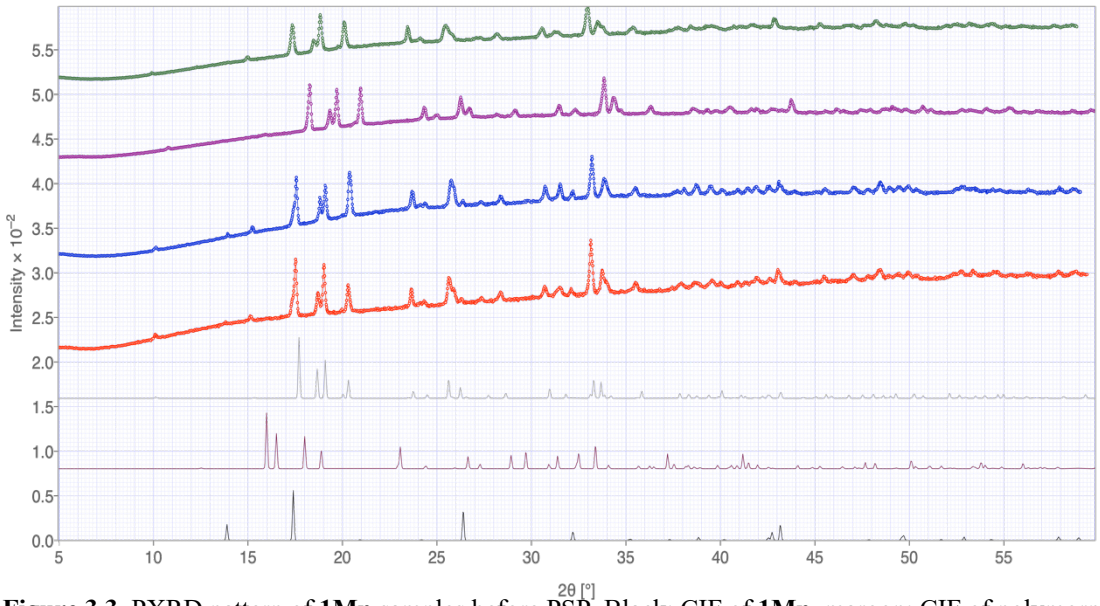


Figure 3.3. PXRD pattern of **1Mn** samples before PSP. Black: CIF of **1Mn**, maroon: CIF of polymorph of **1Mn**, grey: CIF of manganese formate dihydrate, blue, green, purple and red: all PXRD patterns taken from separate vials used in the scale up to make a QENS sample of **1Mn**.

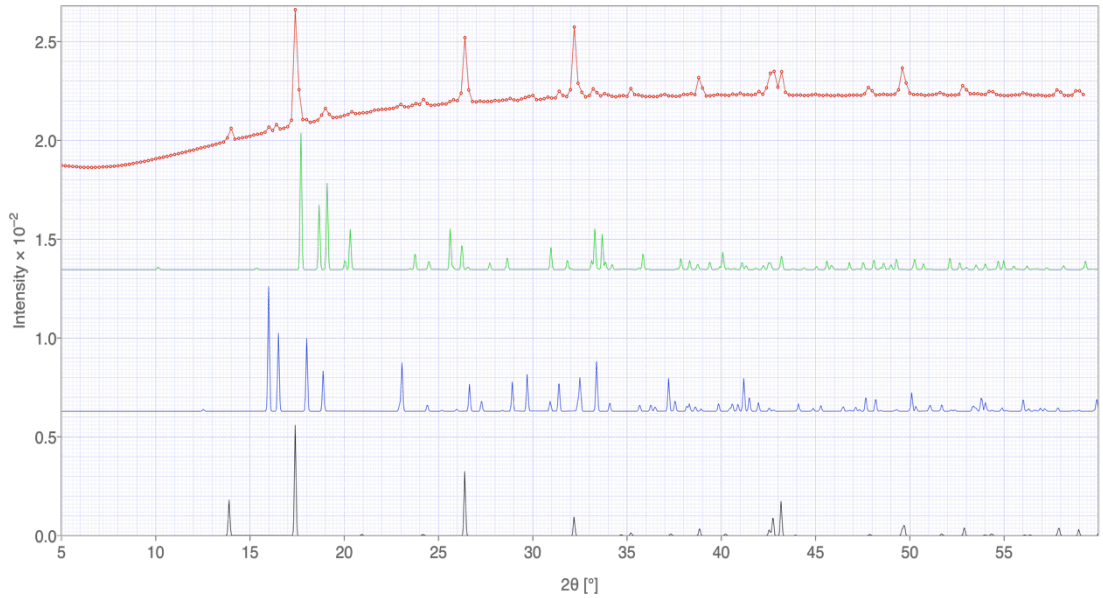


Figure 3.4. PXRD pattern of **1Mn** samples after PSP. Black: CIF of **1Mn**, red: PXRD of **1Mn** after PSP, blue: polymorph of **1Mn** and green: manganese formate dihydrate.

Figure 3.4 clearly shows a significant increase in the purity of **1Mn** following PSP. The impurity peaks have decreased so the resulting sample was an acceptable level of purity to be used for QENS. Le Bail refinements were carried out on the powder X-ray diffraction (PXRD) patterns of the purest phases synthesised.

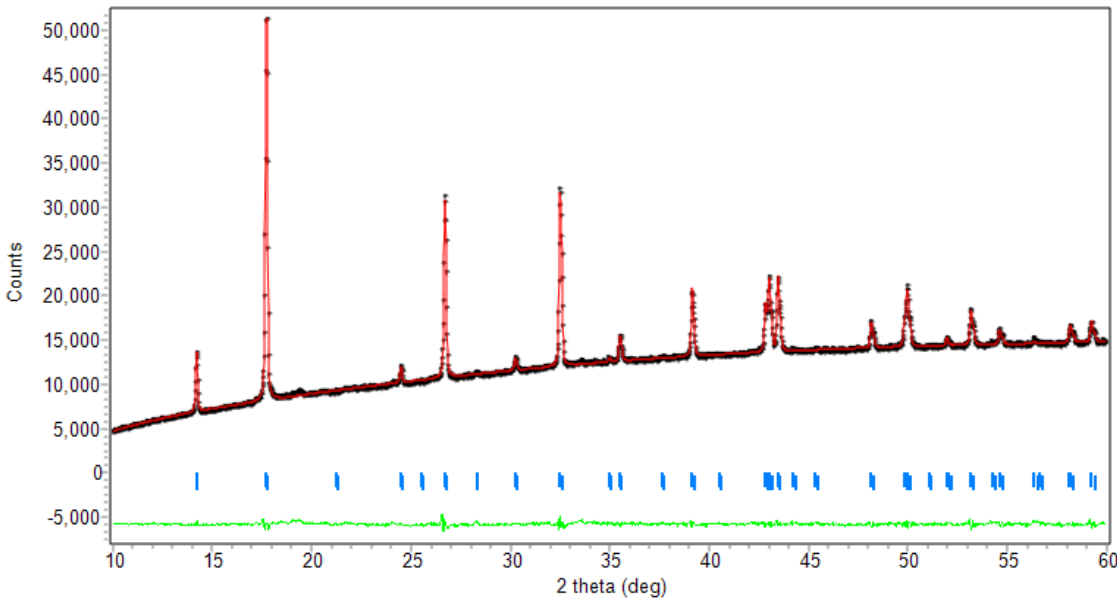


Figure 3.5. Le Bail refinement of **1Mn**. R_p = 0.944, R_{wp} = 1.268 and χ^2 = 1.959. Lattice parameters: a = 7.362(2) and c = 8.486(8). Black: experimental pattern, red: calculated pattern, green: difference between calculated and experimental pattern and blue: Bragg reflections.

As seen in Figure 3.5 the Le Bail fit is very good for **1Mn**, which is evidenced by the statistics and the smoothness between the calculated and experimental pattern (see

Section 2.2.2) confirming the high level of purity for this sample. A similarly good fit is obtained for **2Zn** indicating this material has also been made in pure form.

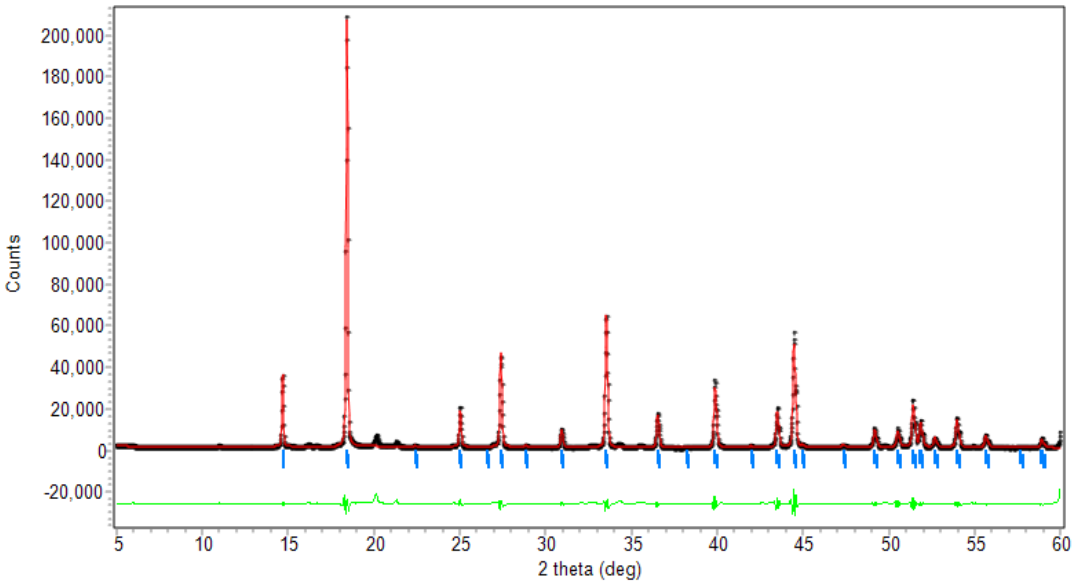


Figure 3.6. Le Bail refinement of **2Zn**. R_p = 8.674, R_{wp} = 13.05 and χ^2 = 61.93. Lattice parameters: *a* = 7.323(2) Å and *c* = 8.185(3) Å. Colour scheme is the same as seen in Figure 3.5.

3.2 Single Crystal Neutron Diffraction

Neutron diffraction was exploited here to gain crystallographic structures, specifically the H atoms, in both **1Mn** and **2Zn** below their transition temperatures, from $P6_322$ to $P6_3$ [58, 60]. Single crystals of 1 mm^3 and 4 mm^3 were grown of **1Mn** and **2Zn** respectively. The low temperature phases of these materials have 22 atoms in the asymmetric unit for **1Mn** and **2Zn** respectively, based on the previously reported X-ray crystal structures [58, 60]. These are too complex to be refined precisely with neutron powder diffraction. Crystallographically, the data (see Tables 3.2-3.9) does not suggest any clear disorder on the NH_4^+ cation of both materials within the cavities of the framework. This conclusion for **1Mn** is taken with caution due to the size limitation of the crystal, particularly for **1Mn**, affecting the quality of data which was obtained. Remnant disorder cannot be dismissed for **1Mn** as no model could fit the positions of an apical hydrogen atom in one out of three ammonium cations within the asymmetric unit nor was there any obvious nuclear density unaccounted for. It is thought unlikely that the hydrogen is not present in the material, so it has been assumed its position is obscured by the modest data available. It is therefore unknown whether this hydrogen is of an ordered or disordered nature. In contrast the NH_4^+ molecules in **2Zn** are clearly modelled, with no evidence of disorder. However, there was evidence of disorder of one

of the formate hydrogen atoms in **2Zn**, which was unusual and unexpected. The origin of this is unclear. This is likely a result of a small degree of thermal motion between two alternative positions, but we cannot exclude this may contribute to the dielectric properties of these materials.

Table 3.1. Crystallographic information of **1Mn** and **2Zn**.

	1Mn	**2Zn**
Empirical Formula	$Mn_3C_9N_3O_{18}H_{20}$	$ZnC_3NO_6H_7$
Formula Weight/g mol^{-1}	623.10	218.49
Crystal System	Hexagonal	Hexagonal
Space Group	$P6_3$	$P6_3$
Radiation	Neutrons	Neutrons
Temperature	22 K	22 K
Lattice Parameters	a = 12.65(10) Å b = 12.65(10) Å c = 8.55(10) Å α = 90° β = 90° γ = 120°	a = 12.6178(3) Å b = 12.6178(3) Å c = 8.2344(3) Å α = 90° β = 90° γ = 120°
Cell Volume/Å^3	1184.989(2)	1135.35(2)
Density/g cm^{-1}	1.7463	1.9172
Z value	2	6
μ/cm^{-1}	0.034	0.041
Reflections	3837/3837	18201/18201
Parameters Refined	73	89
R_1, wR_2 (all)	0.1010, 0.2556	0.1010, 0.2590
R_1, wR_2 (obs)	0.1010, 0.2556	0.1010, 0.2590
χ^2	1.096	1.032

R_{int} values have been omitted due to significant deviations between the intensities of symmetry equivalent reflections caused by absorption, as a result of using time-of-flight single crystal neutron diffraction. For the same reason it is not relevant to state the wavelength of neutrons used.

Table 3.2. Mn-O bond lengths in the low temperature crystal structure of **1Mn**.

Mn-O1: 2.16(6) Å	**Mn-O2**: 2.18(8) Å	**Mn-O3**: 2.24(8) Å
Mn-O4: 2.14(8) Å	**Mn-O5**: 2.19(7) Å	**Mn-O6**: 2.19(8) Å

Table 3.3. Bond lengths of the organic components in the low temperature crystal structure of **1Mn**.

Bond	**Length/Å**
C-O	1.21(4)-1.34(4)
H···O	1.79(6)-1.89(6)

Table 3.4. O-Mn-O bond angles in the low temperature crystal structure of **1Mn**

O1-Mn-O2: 102(3)°	**O1-Mn-O6**: 92(2)°	**O4-Mn-O1**: 85(3)°	**O4-Mn-O5**: 88(3)°	**O6-Mn-O3**: 88(2)°
O4-Mn-O6: 175(4)°	**O2-Mn-O3**: 165(4)°	**O4-Mn-O2**: 94(2)°	**O5-Mn-O6**: 96(3)°	**O1-Mn-O3**: 90(2)°
O1-Mn-O5: 167(5)°	**O2-Mn-O6**: 83(4)°	**O4-Mn-O3**: 96(4)°	**O5-Mn-O3**: 79(3)°	**O2-Mn-O5**: 90(2)°

Table 3.5. Range of other significant bond angles in the low temperature crystal structure of **1Mn**.

Angle	**Range in angle/°**
O-C-O	118(3) – 133(3)
$\mathbf{H_{equatorial}}$**-N-**$\mathbf{H_{equatorial}}$	99(4) – 118(3)
$\mathbf{H_{equatorial}}$**-N-**$\mathbf{H_{apical}}$	102(3) – 116(2)

The poor precision in the **1Mn** crystal structure prevents drawing significant conclusions from the bond distances obtained (see Tables 3.2 and 3.3). The range of bond angles in both the apical and equatorial angles suggest some distortion of the octahedra of the manganese environments, see Table 3.4. Also, the range of bond angles within the NH_4^+ tetrahedra indicate these are likely to be distorted, see Table 3.5, possibly due to the strong hydrogen bonding in these materials. The structure of **1Mn** determined by SCND can be seen in Figure 3.7-2.9. The hydrogen bond network is constructed via only the equatorial hydrogen positions of the ammonium cations which are positioned along the *c*-axis, see Figures 3.7 and 3.8. Along these channels, the ammonium cations are orientated in such a way which resembles an anti or gauche conformation, so six hydrogen bonds are seen down this *c*-axis.

Table 3.6. Zn-O bond lengths in the low temperature crystal structure of **2Zn**.

Zn-O1: 2.112(5) Å	**Zn-O2**: 2.103(5) Å	**Zn-O3**: 2.096(5) Å
Zn-O4: 2.116(5) Å	**Zn-O5**: 2.112(5) Å	**Zn-O6**: 2.106(5) Å

Table 3.7. Range of other significant bond lengths in the low temperature crystal structure of **2Zn**.

Bond	**Range in length/Å**
C-O	1.251(5)-1.265(4)
H···O	1.79(1)-1.83(1)

Table 3.8. O-Zn-O bond angles in the low temperature crystal structure of **2Zn**.

O1-Zn-O4: 81.5(2)°	**O2-Zn-O5**: 169.7(3)°	**O3-Zn-O2**: 82.7(2)°	**O5-Zn-O1**: 91.76(18)°	**O6-Zn-O5**: 81.9(2)°
O2-Zn-O1: 96.3(2)°	**O2-Zn-O6**: 90.87(18)°	**O3-Zn-O5**: 90.61(18)°	**O5-Zn-O4**: 96.5(2)°	**O3-Zn-O4**: 170.3(3)°
O2-Zn-O4: 91.08(19)°	**O3-Zn-O1**: 91.71(18)°	**O3-Zn-O6**: 95.7(2)°	**O6-Zn-O4**: 91.82(18)°	**O6-Zn-O1**: 170.3(3)°

Table 3.9. Range of other significant bond angles in the low temperature crystal structure of **2Zn**.

Angle	**Range in angle/°**
O-C-O	124.1(4) – 124.7(4)
$\mathbf{H_{equatorial}}$**-N-**$\mathbf{H_{equatorial}}$	109.86(7) – 111.27(8)
$\mathbf{H_{equatorial}}$**-N-**$\mathbf{H_{apical}}$	107.6(8) – 109.1(7)

The structure of **2Zn** determined by SCND can be seen in Figure 3.10-3.12. NH_4^+ and ZnO_6^- polyhedra appear to have limited distortion from the ideal for **2Zn**, as the measured bond angles of O-Zn-O and H-N-H environments deviate from those in undistorted structures. (see Tables 3.6-3.9). It should be noted that the standard deviations of the bonds for **2Zn** are far more precise tan for **1Mn** reflecting the better quality of data. Alongside the intermediate bond lengths for the C-O bonds, due to the delocalised nature, similarly to **1Mn**.

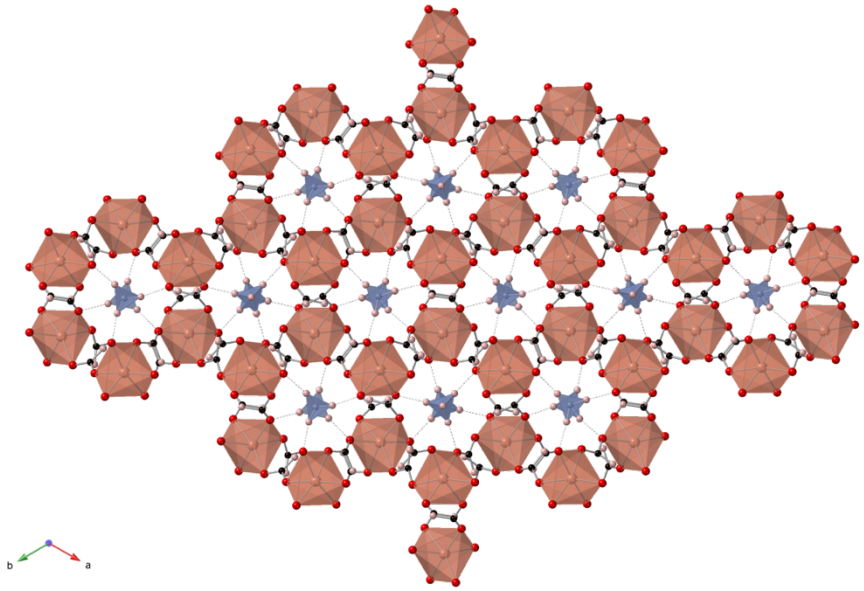


Figure 3.7. Crystal structures of **1Mn** along the *c*-axis. Mn octahedra shown in peach, O: red, C: black, H: pink, N tetrahedra: blue.

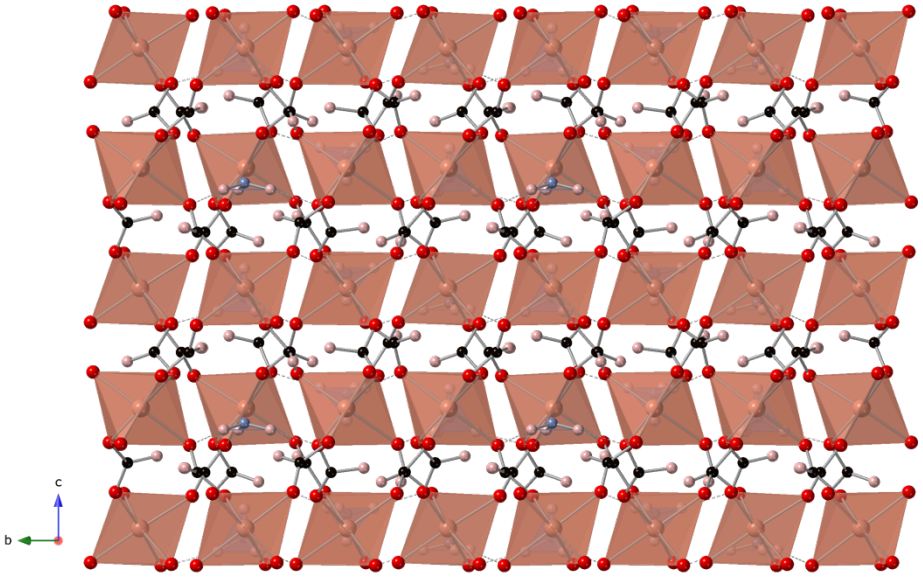


Figure 3.8. Crystal structures of **1Mn** along the *a*-axis, colour scheme the same as in Figure 3.7.

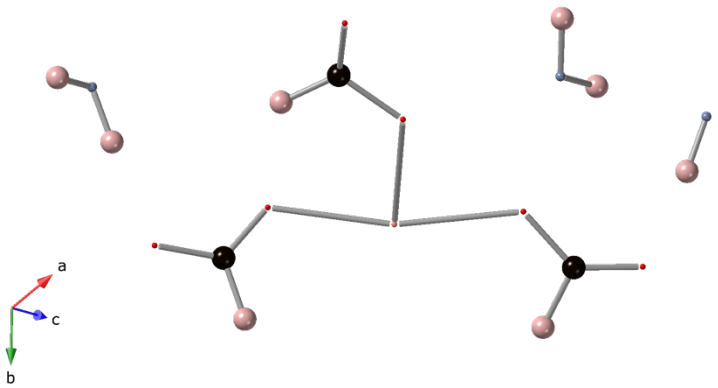


Figure 3.9. Asymmetric unit of **1Mn**. Atoms shown as ellipsoids. Colour scheme the same as Figure 3.7.

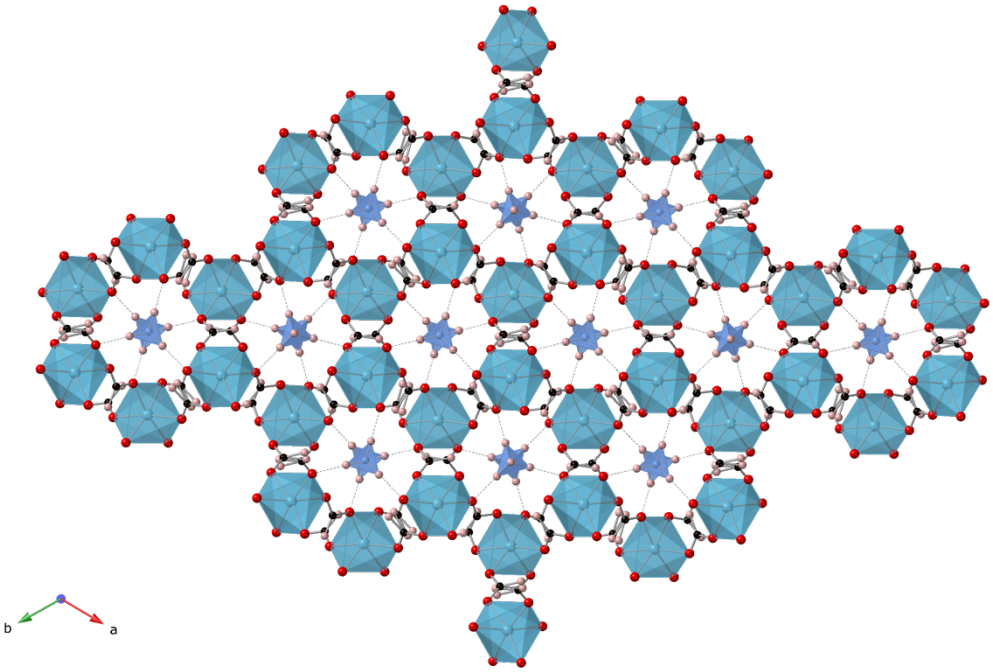


Figure 3.10. Crystal structure of **2Zn** along the *c*-axis. Zn octahedra shown in turquoise, O: red, C: black, H: pink, N tetrahedra: blue.

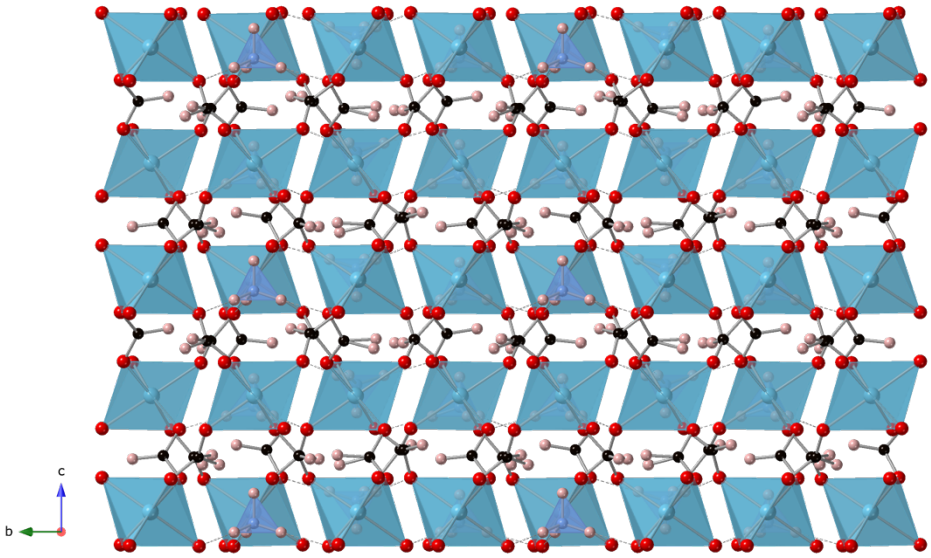


Figure 3.11. Crystal structure of **2Zn** along the *a*-axis. Colour scheme the same as Figure 3.10.

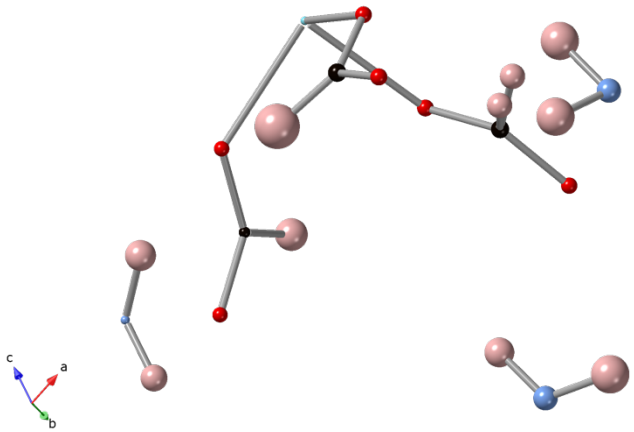


Figure 3.12. Asymmetric unit of **2Zn**. Atoms shown as ellipsoids. Colour scheme the same as Figure 3.10.

The disorder of the hydrogen atoms on one of the formate linkers is clearly seen in Figure 3.12. No other disorder is found in this crystal structure suggesting the NH_4^+ molecules are well ordered from a crystallographic perspective. Much like in **1Mn** the hydrogen bonding network is constructed between only the hydrogen atoms in the equatorial positions on the cation along the *c*-axis, and again, the cations are assembled resembling an anti or gauche conformation, which can be seen in Figure 3.10.

3.3 Quasi-elastic Neutron Scattering (QENS)

QENS was used to determine whether there was any evidence of significant dynamics of the NH_4^+ cations within **1Mn** and **2Zn** in the low temperature phase and when this is heated through the crystallographic phase transition. A Mean Square Displacement (MSD) fit is a linear fit of the log of elastic intensity with respect to Q^2. This is a direct measure of the amount of motion of the hydrogen atoms in the material as the quasi-elastic scattering is dominated by hydrogen atoms. Plots of this versus temperature are shown in Figure 3.13.

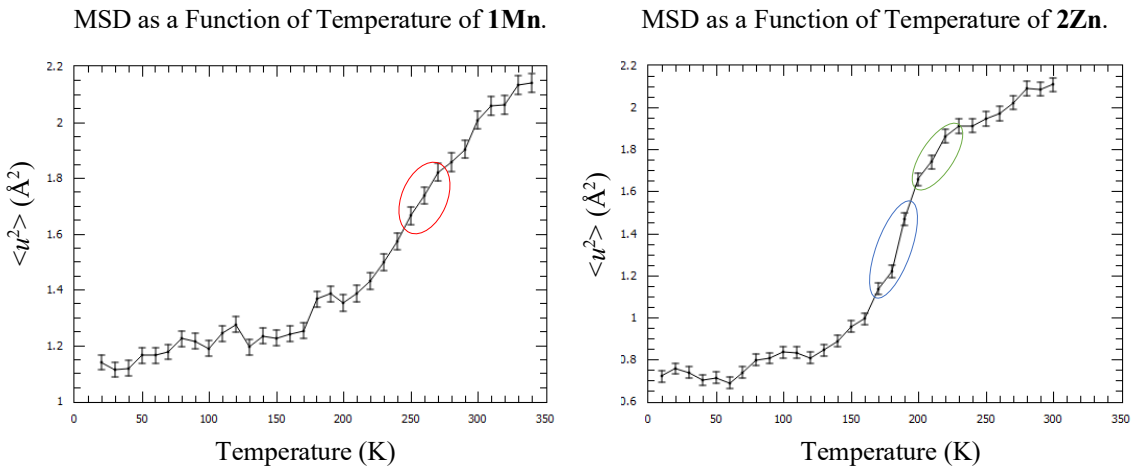


Figure 3.13. MSD as a function of temperature of both **1Mn** (left) and **2Zn** (right).

The errors in the plot of MSD as a function of temperature for **2Zn** are significantly smaller than those in the plot for **1Mn**, suggesting that the data is better quality for **2Zn.** In both cases, however, the errors are relatively small and consistent. In the plot of **1Mn**, there is no significant increase in thermal motion until around 200 K where the MSD begins to increase rapidly. This suggests the hydrogen atoms begin to exhibit a significant amount of movement at which point the structure is still in the low temperature $P6_3$ phase, consistent with presence of some dynamic disorder. This could be the form of the equatorial hydrogen atoms rotating around a 3-fold axis. These

crystallographically sites are equivalent so such motion would not be detected in the crystal structure. There is also a small 'kink', a deviation from the trend between 250 K and 270 K, highlighted in red, which the ammonium cation is likely culpable for, given the phase transition occurs at 254 K in **1Mn** [58, 60]. At temperatures above around 330 K the plot appears to flatten out which is most likely due to the thermal motion of the atoms being too fast for the OSIRIS time window, such that additional motion is not detected.

For **2Zn**, a similarly phenomenon occurs, with motion relatively constant to 150 K, above which it begins to increase significantly. This is again well below the crystallographic transition, which occurs in **2Zn** at 191 K [58, 60]. This also suggests some form of dynamical disorder below the phase transition. Again, there is another deviation between 200 K and 220 K, highlighted in green, suggesting a change in motion of the hydrogen atoms, most likely in the NH_4^+ groups. Again, the plot appears to flatten as the temperature nears 300 K and can be assumed that this is also because the movement of hydrogen atoms is too fast for the OSIRIS time window.
A plot of the EISF as a function of Q shows the relationship between Q and the extent of QENS within the system. As discussed previously (see Section 2.4) the EISF is a ratio relating the integrated intensities of the quasi-elastic and elastic intensities and lies between 0 and 1. So therefore, as EISF value closer to 1 suggests a more elastic nature, and at higher Q values, the extent of QENS increases. This is evidenced in both **1Mn** and **2Zn**, see below.

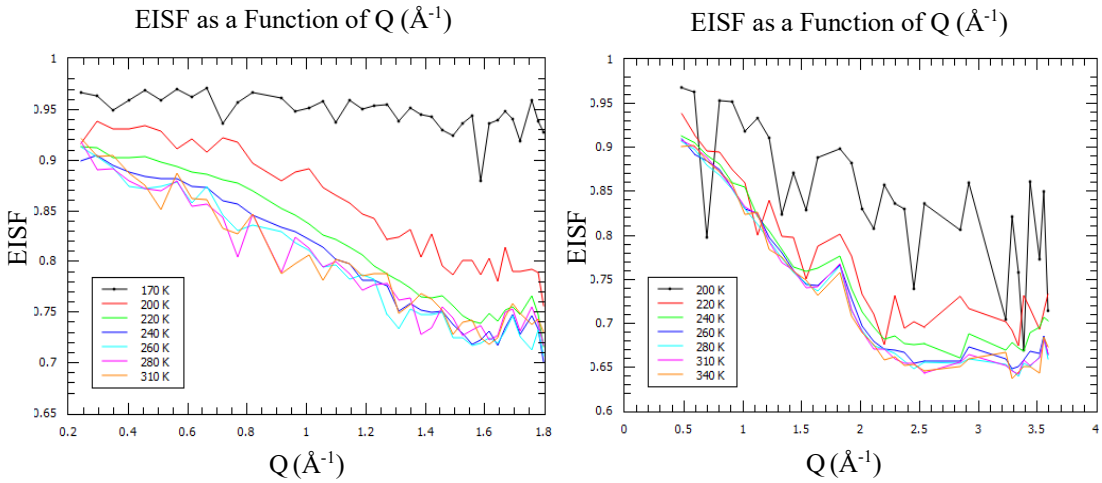


Figure 3.14. EISF as a function of Q for **1Mn** using the resolution of (002) (left) and (004) (right) setting of the OSIRIS monochromator.

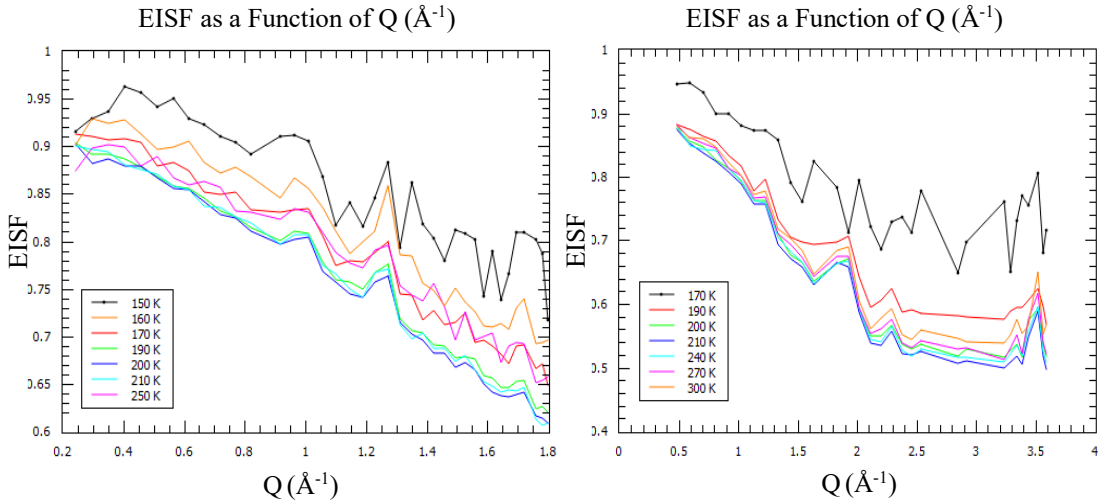


Figure 3.15. EISF as a function of Q for **2Zn** using the resolution of (002) (left) and (004) (right) setting of the OSIRIS monochromator.

Both Figure 3.14 and 3.15 show an identical downwards trend of increasing Q for both (002) and (004) settings and displays no significant chance in the shape across the phase transition implying there is no change in the dominant type of motion of these hydrogen atoms. This is indicative of dynamic disorder below T_C, which was not seen crystallographically because the atoms may be moving between already known crystallographic sites, and therefore appear equivalent. No clear minimum in Q is seen for either the (002) setting, because this is outside the range it can detect, but also in for the (004) setting due to Bragg reflections interfering with the spectra making it difficult to determine the nature of this motion and which axis the atoms are rotating around.

3.4 Infrared Spectra

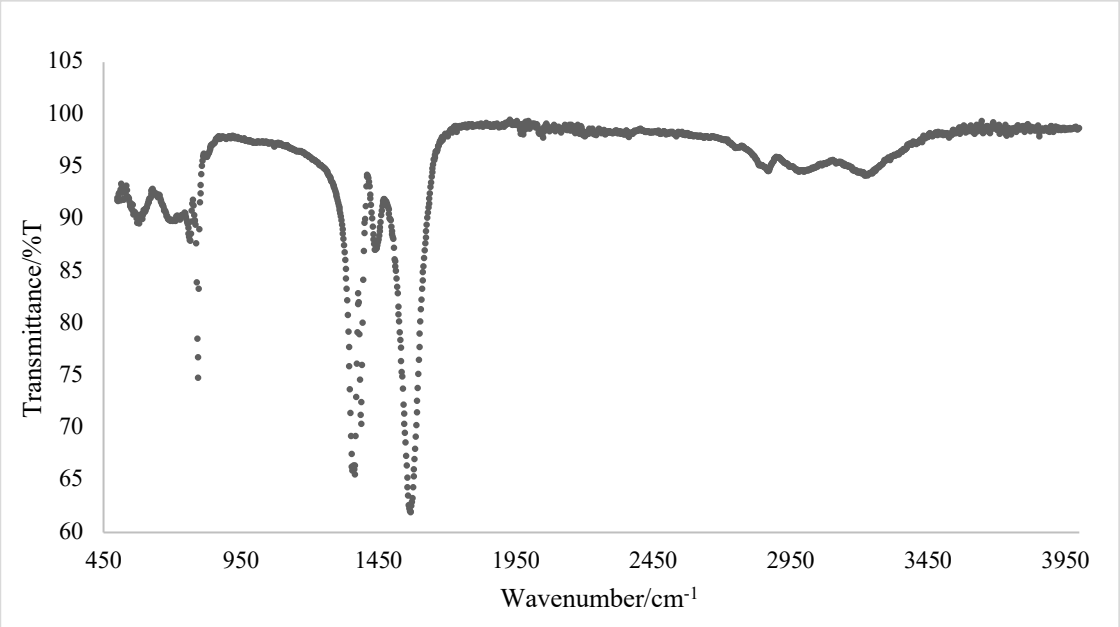


Figure 3.16. IR spectrum of **1Mn**.

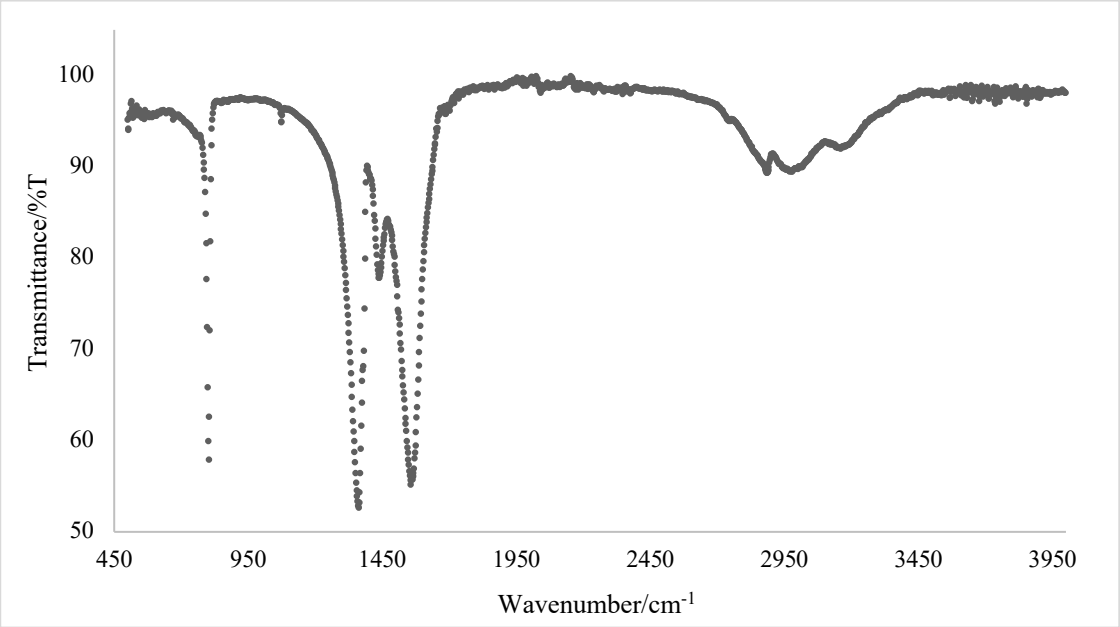


Figure 3.17. IR spectrum of **2Zn**.

The isostructural nature of these systems results in almost identical IR spectra therefore the vibrational frequencies appear in the same regions for both spectra. They will therefore be discussed together. In both materials the peak at the highest wavenumber are assigned to a N-H stretching vibrational mode, the peaks in the region of ~2950 cm^{-1} and between 1500 and 1400 cm^{-1} suggest C-H stretching modes while the peak at ~800 cm^{-1} is suggestive of a C-H bending mode. The intense peak around 1500 cm^{-1} is typical of a C-O stretching mode in carbonyls.

3.5 Conclusion

To conclude, only limited static disorder of the ammonium cations can be detected crystallographically using single crystal neutron diffraction. No crystallographic disorder of the $NH4^+$ cation has been observed for **2Zn**. The only presence of disorder was found in the hydrogen atom of one of the formate linker in **2Zn**, which may contribute to the dielectric properties. Conclusions for **1Mn** are less clear as one of the hydrogen atoms in one of the ammonium cations within the asymmetric unit cannot be modelled, most likely due to the quality of the data obtained. There was evidence of significant dynamic disorder below the transition temperatures of both these materials using QENS, displaying motion of the hydrogen atoms leading up to T_C. The inability to identify a minimum in the EISF plots means the axis at which these rotations occur is unknown. It is also noted that the nature of the EISF plot did not change significantly between the low and high temperature crystallographic phases, suggesting that the dominant type of the motion does not change either side of the phase transition. It is thus more likely that these dynamics will contribute to the relaxor-like behaviour than the static disorder.

Chapter 4

Structural Determination and Physical Properties of $((CH_3)_2NH_2)Ln(C_2O_4)_x(HCO_2)_y$ phases

4.1 Structural Determination and Physical Properties of $((CH_3)_2NH_2)Er(C_2O_4)(HCO_2)_2$

The novel phase, **1Er**, which has the chemical formula $((CH_3)_2NH_2)Er(C_2O_4)(HCO_2)_2$, was discovered initially by a previous masters student in the Saines group but only briefly characterised. It is highly interesting due to the fact that the dimethylammonium is ordered at room temperature suggesting a route towards room temperature ferroelectrics if related materials with polar space groups can be made. This chapter analyses the $((CH_3)_2NH_2)Er(C_2O_4)(HCO_2)_2$ phase and new related $ALn(C_2O_4)_{1.5}(HCO_2)$ phases in detail using a range of techniques such as single crystal and powder X-ray diffraction, inelastic neutron spectroscopy and SQUID magnetometry. In the case of the $ALn(C_2O_4)_{1.5}(HCO_2)$ phases, while the A-site cation cannot be identified crystallographically, allied techniques strongly suggest this is disordered dimethylammonium.

4.1.1 Crystal Structures of the $((CH_3)_2NH_2)Er(C_2O_4)(HCO_2)_2$ phase

Pale pink single crystals were synthesised that were about 0.2 mm in all dimensions. These were used for single crystal X-ray structure determination (see Table 4.1 for crystallographic details and 4.2-4.5 for bond distances). At 293 K, this system adopts the centrosymmetric space group *P*2/*n* with monoclinic symmetry. Within the asymmetric unit of this material there are two erbium sites, one distinct dimethylammonium molecule, two distinct formate linkers and one distinct oxalate linker, with a total of 27 sites within the asymmetric unit, see Figure 4.1. The erbium

sites within the asymmetric unit are distorted square antiprism polyhedra, with all the formate ligands bridging in an *anti-anti* formation. Deviations in the bond lengths and angles from ideal geometries is most likely due to competing effects between electrostatics and covalent bonding interactions of the ligand, which have restricted the geometries.

Table 4.1. Crystallographic information of **1Er** at 293 K.

	1Er
Empirical Formula	$ErC_6NO_8H_{10}$
Formula Weight/g mol^{-1}	391.41
Crystal System	Monoclinic
Space Group	*P* 2/n
Radiation	Mo Kα, λ = 0.71 Å
Temperature	293 K
Lattice Parameters	a = 9.1733(3) Å b = 8.9831(3) Å c = 13.1873(4) Å α = 90° β = 96.948(3)° γ = 90°
Cell volume/Å^3	1078.71(6)
Density/g cm^{-1}	2.4104
Z value	4
μ/cm^{-1}	7.807
Reflections	8769/2702
R_{int}	0.0253
Parameters Refined	148
R_1, wR_2 (all)	0.0218, 0.0396
R_1, wR_2 (obs)	0.0182, 0.0383
χ^2	1.061

Formate ligands connect the erbium sites along the *c*-axis, and interestingly along the *b*-axis alternate oxalate and formate ligands connect the erbium polyhedra and along the *a*-axis alternate chains of formate and oxalate ligands connect erbium polyhedra. The

dimethylammonium cations occupy octagonal channels along the *c*-axis, as seen in Figure 4.2.

Table 4.2. Er-O bond lengths in **1Er** of both erbium sites in asymmetric unit at 293 K.

Er1-O		**Er2-O**	
Er1-O1A: 2.3696(18) Å	**Er1-O1A**: 2.3697(18) Å	**Er2-O1B**: 2.3256(19) Å	**Er2-O1B**: 2.3257(19) Å
Er1-O3B: 2.3458(19) Å x2	**Er1-O3A**: 2.3808(19) Å	**Er2-O3C**: 2.3579(19) Å x2	**Er2-O3D**: 2.3856(19) Å x2
Er1-O2B: 2.277(2) Å x2	**Er1-O3A**: 2.3809(19) Å	**Er2-O2A**: 2.288(2) Å x2	

Table 4.3. O-Er1-O bond angles in **1Er** at 293 K.

O2B-Er1-O3A: 139.74(7)° x2	**O1A-Er1-O3A**: 118.85(7)° x2	**O3B-Er1-O1A**: 137.86(7)° x2	**O1A-Er1-O3A**: 74.54(7)° x2
O3B-Er1-O1A: 75.06(7)° x2	**O3B-Er1-O3A**: 82.16(7)° x2	**O3B-Er1-O3A**: 67.90(6)° x2	**O2B-Er1-O3A**: 76.19(8)° x2
O3A-Er1-O3A: 140.45(11)°	**O3B-Er1-O3B**: 81.46(11)°	**O2B-Er1-O2B**: 78.41(13)°	**O1A-Er1-O1A**: 142.79(10)°
O2B-Er1-O3B: 150.83(7)° x2	**O2B-Er1-O3B**: 107.53(9)° x2	**O2B-Er1-O1A**: 80.45(7)° x2	**O2B-Er1-O1A**: 70.82(7)° x2

Table 4.3. O-Er2-O bond angles in **1Er** at 293 K.

O1B-Er2-O3C: 142.20(7)° x2	**O1B-Er2-O3C**: 76.95(7)° x2	**O3C-Er2-O3C**: 80.59(10)°	**O1B-Er2-O1B**: 136.58(11)°
O1B-Er2-O3D: 78.35(7)° x2	**O1B-Er2-O3D**: 118.07(8)° x2	**O3C-Er2-O3D**: 67.94(6)°	**O3C-Er2-O3D**: 79.73(7)°
O2A-Er2-O3C: 142.35(7)° x2	**O2A-Er2-O1B**: 75.01(8)° x2	**O2A-Er2-O1B**: 74.21(7)° x2	**O3D-Er2-O3D**: 137.42(11)°
O2A-Er2-O3C: 107.62(9)° x2	**O2A-Er2-O3D**: 70.43(9)° x2	**O2A-Er2-O3D**: 148.86(8)° x2	**O2A-Er2-O2A**: 88.31(15)°

Table 4.4. Range of other significant bond lengths in **1Er** at 293 K.

Bond	**Range in length/Å**
C-O (formate)	1.209(4)-1.255(3)
C-O (oxalate)	1.243(3)-1.250(3)

Table 4.5. Range of other significant bond angles in **1Er** at 293 K.

Bond	Range in angle/°
O-C-O (formate)	126.7(2)-127.4(2)
O-C-O (oxalate)	124.7(3)-125.7(3)

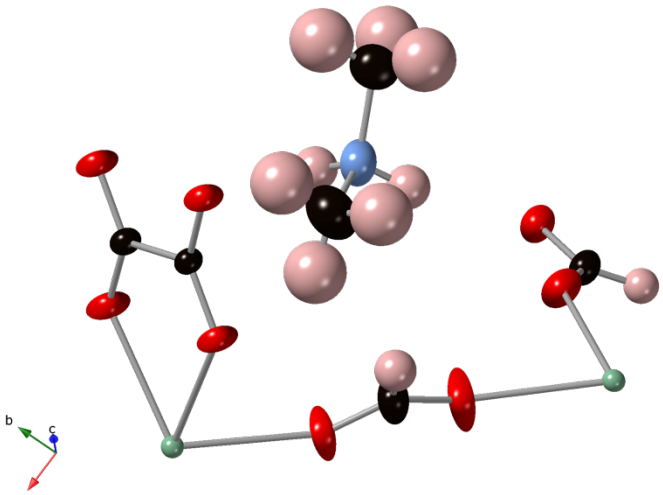


Figure 4.1. Asymmetric unit of **1Er** at 293 K. Er: green, O: red, C: black, H: pink and N: blue.

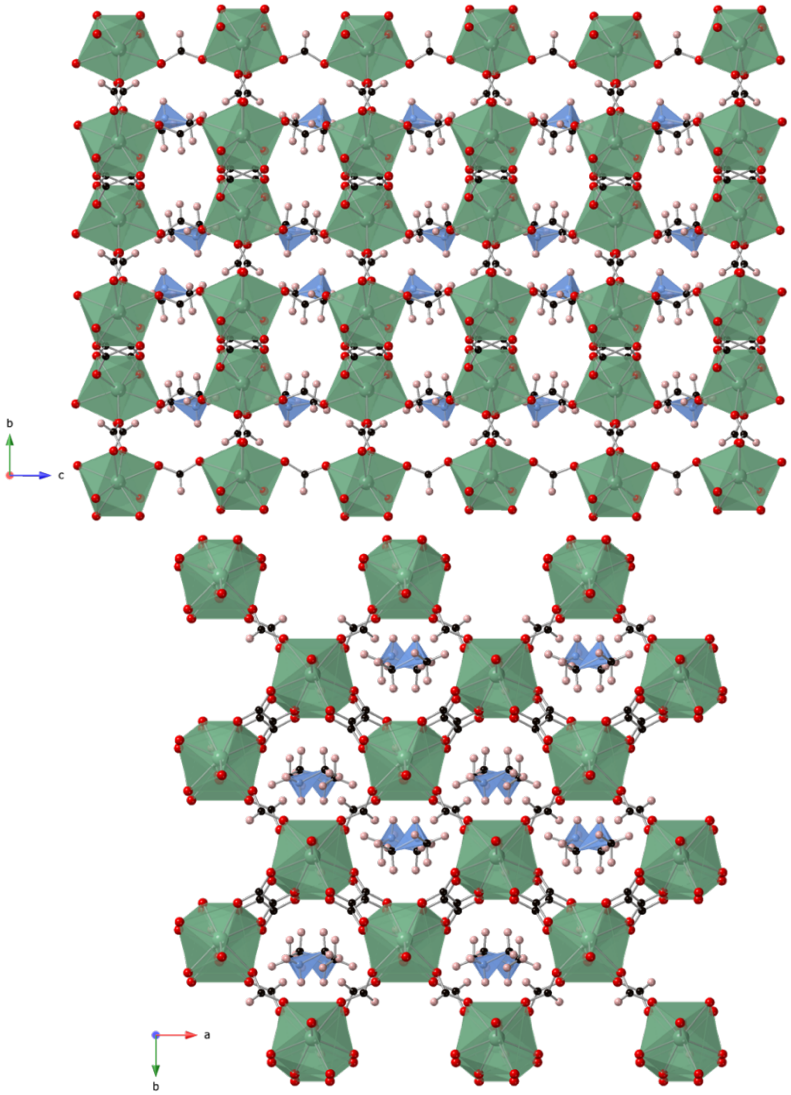


Figure 4.2. Crystal structure of **1Er** at 293 K along the *a*-axis (top) and *c*-axis (bottom). Colour scheme same as in Figure 4.1.

SCXRD measurements were collected at intermediate temperatures every ~ 25 K, between 270 and 90 K, to deduce whether there was a phase transition of this material, on cooling. No phase transition was apparent and the change in the structure down to 90 K is minimal neglecting displacement parameters. Further variable temperature measurements were collected between 293 K and 500 K, the limit of the in-house cryostream, to determine up to what temperature the dimethylammonium cations remained ordered. Interestingly, up to 500 K the dimethylammonium cations remain ordered, which is an extremely promising property for above room temperature ferroelectric properties, if with further synthetic effort the dimethylammonium can be replaced with a different amine, that forms polar structures at room temperature.

Figure 4.3 shows no significant increase in the cell dimensions as a function of temperature and remains almost consistent from 90 K up to 500 K. There is also no correlation between angle β and temperature as well as between the cell volume and temperature, see appendix. However, as the temperature increases from room temperature to 500 K, the displacement parameters increase also, due to the increased thermal motion the atoms exhibit at higher temperatures.

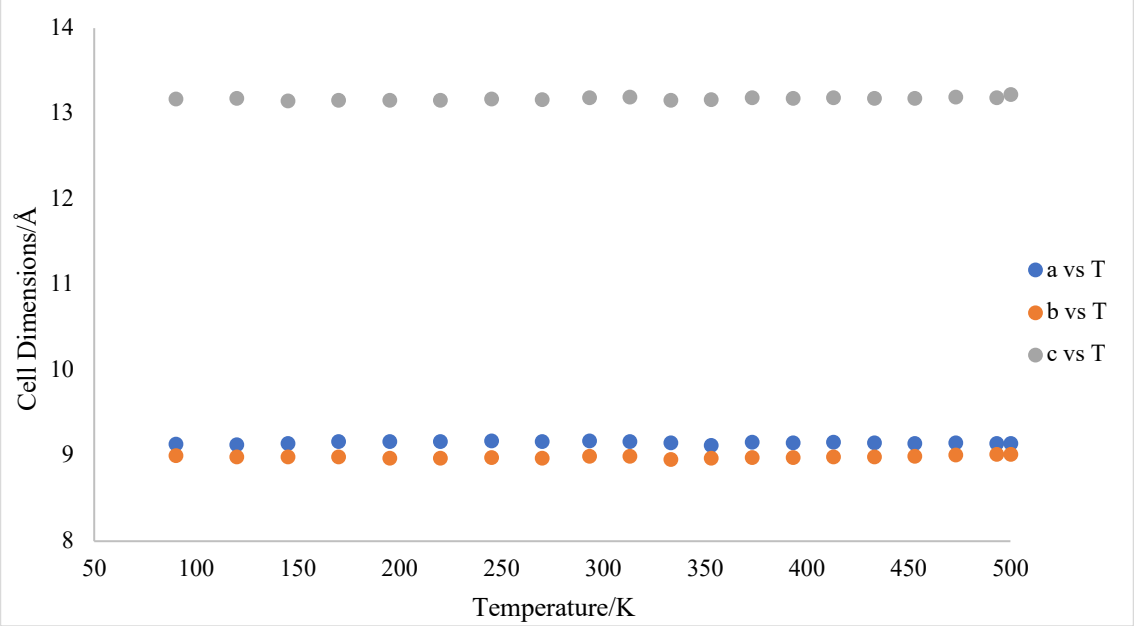


Figure 4.3. A plot of the lattice parameters, *a, b* and *c* as a function of temperature of **1Er** between 90 and 500 K.

4.1.2 Determination of Phase Purity using Powder X-ray Diffraction and Microanalysis

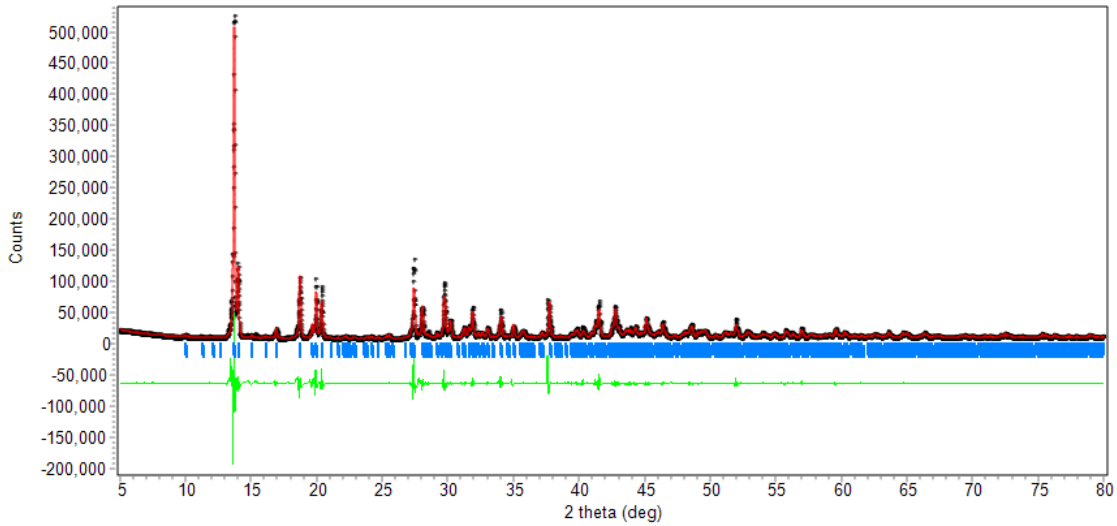


Figure 4.4. Le Bail fit of **1Er**. R_p = 6.465, R_{wp} = 11.17 and χ^2 = 195.06. Lattice parameters: a = 9.185(34) Å, b = 8.985(25) Å and c = 13.195(31) Å, β = 90°. colour scheme same as in Figure 3.5.

Once a pure phase of this material was obtained a Le Bail refinement was used to confirm this, see Figure 4.4. The difference plot shows a lack of additional reflections not allowed by the crystal structure confirming the lack of significant impurities within this sample. The conditions used to make this sample (see Section 2.1.2) were used hereafter for producing multigram samples for further analysis, by multiple batches.

Numerous attempts were made to incorporate varying protonated amines into the pores of this $[Er(C_2O_4)(HCO_2)]^-$ framework, including methylammonium, ethylammonium and hydroxylammonium, but unfortunately, all were unsuccessful. This was suspected to be a result of the decomposition of DMF producing dimethylammonium in such an excess, so the reaction favoured the inclusion of dimethylammonium over the other protonated amines into the product.

Microanalysis was performed on this material by Dr Stephen Boyer at the London Metropolitan to confirm the purity and molecular formula. Microanalysis identifies the percentage of C, H and N within a given material. The expected results were 18.41 %, 2.58 % and 3.58 % for C, H and N, respectively, and the results were 18.38 %, 2.56 % and 3.52 % for C, H and N respectively. These results are extremely similar to the

expected values; therefore, it can be concluded that the molecular formula is correct and confirms the phase purity of the sample.

4.1.3. Magnetic Properties

A plot of χ versus temperature shows the susceptibility gradually increasing on cooling and show no divergence of the zero field-cooled (ZFC) and field-cooled (FC) measurements, see Figure 4.5, this is consistent with paramagnetic behaviour. However, the insert in Figure 4.5 shows a decreasing Curie constant on cooling, as $\chi = \frac{C}{T}$ where C is the Curie constant. This is indicative of a decreasing effective magnetic moment, suggesting antiferromagnetic interactions have arisen on a decrease in temperature.

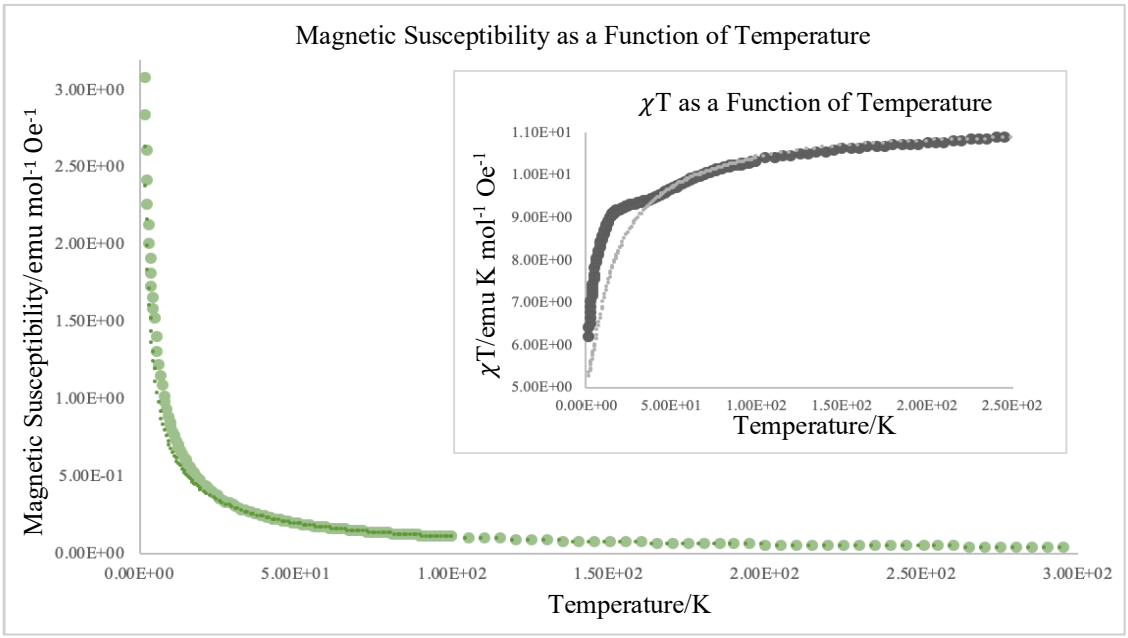


Figure 4.5. Magnetic susceptibility as a function of temperature of **1Er**. The insert is of magnetic susceptibility multiplied by T as a function of T. Pale green and dark grey: ZFC, dark green and pale grey: FC.

The Curie-Weiss plot, see Figure 4.6, shows a strong linear correlation between the inverse magnetic susceptibility and the increasing temperature which is consistent with Curie-Weiss paramagnetism. This fit can be used to calculate the Curie constant, Weiss temperature and effective magnetic moment of the magnetic metal atom within the structure. The Curie constant, Weiss temperature and effective magnetic moment were calculated to be 11.09, -5.81 K and 9.42 u_B, respectively corresponding to the effective magnetic moment (μ_{eff}) which is close to the value of 9.58 u_B expected for by Russel-Saunders coupling. The calculated negative value of the Weiss constant is consistent with short range antiferromagnetic interactions becoming apparent on cooling.

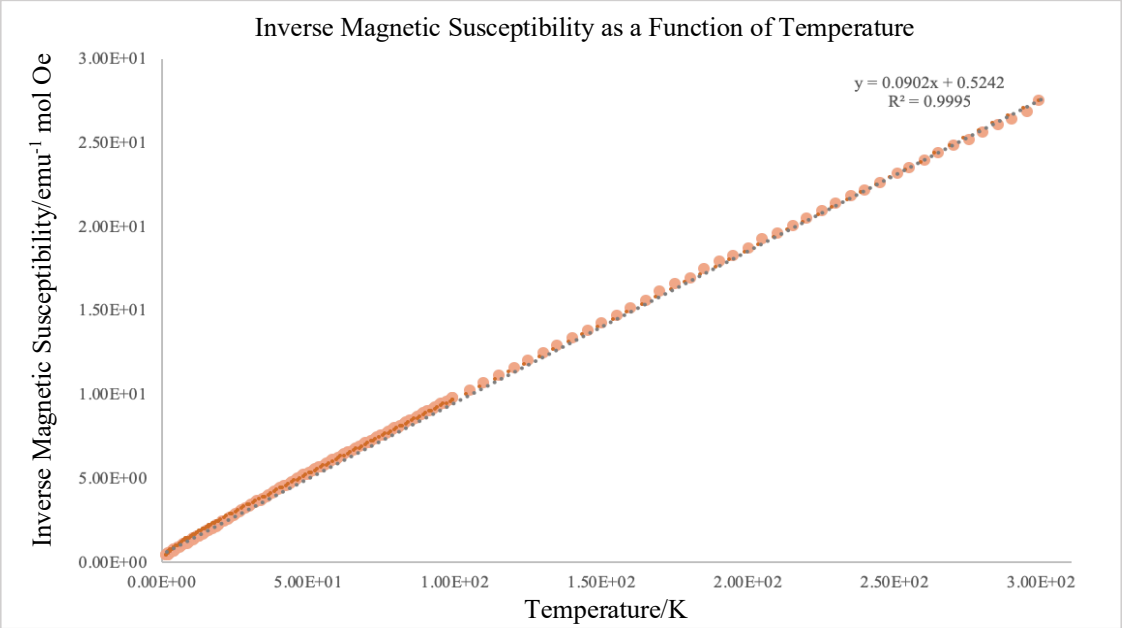


Figure 4.6. Curie-Weiss plot of **1Er**. Pale orange: ZFC and dark orange: FC.

Figure 4.7 shows a linear increase in magnetisation with the applied magnetic field, up to ~10 kOe where the magnetisation reaches a threshold and is saturated, displayed by the plot flattening out. There is no indication of hysteresis, only a slight deviation in the 0 – 50 kOe measurement when the field is first applied, from the remainder of the curve, which is assumed to be an artefact. This is consistent with paramagnetic behaviour being retained at low temperature.

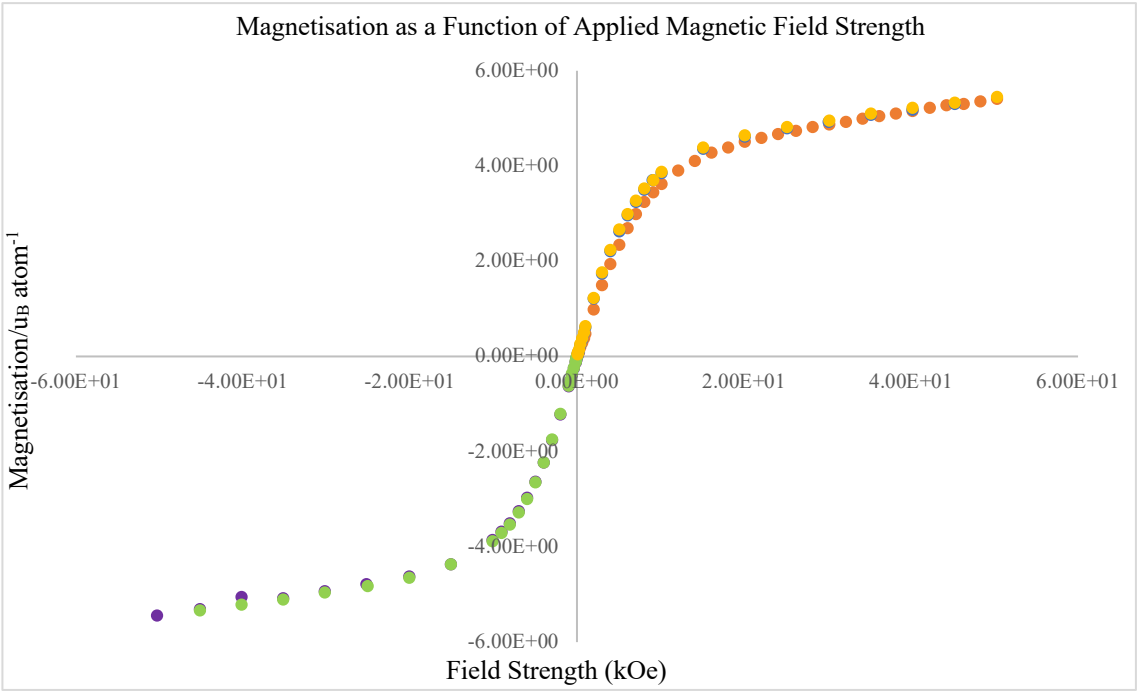


Figure 4.7. Magnetisation as a function of applied magnetic field strength of **1Er**.

4.1.4. Thermal Stability

Figure 4.8 and 4.9 display the TGA-DSC data of **1Er**. The data shows that **1Er** is thermally stable up to ~ 288 °C where the species undergoes an endothermic decomposition, which is complete by 400 °C.

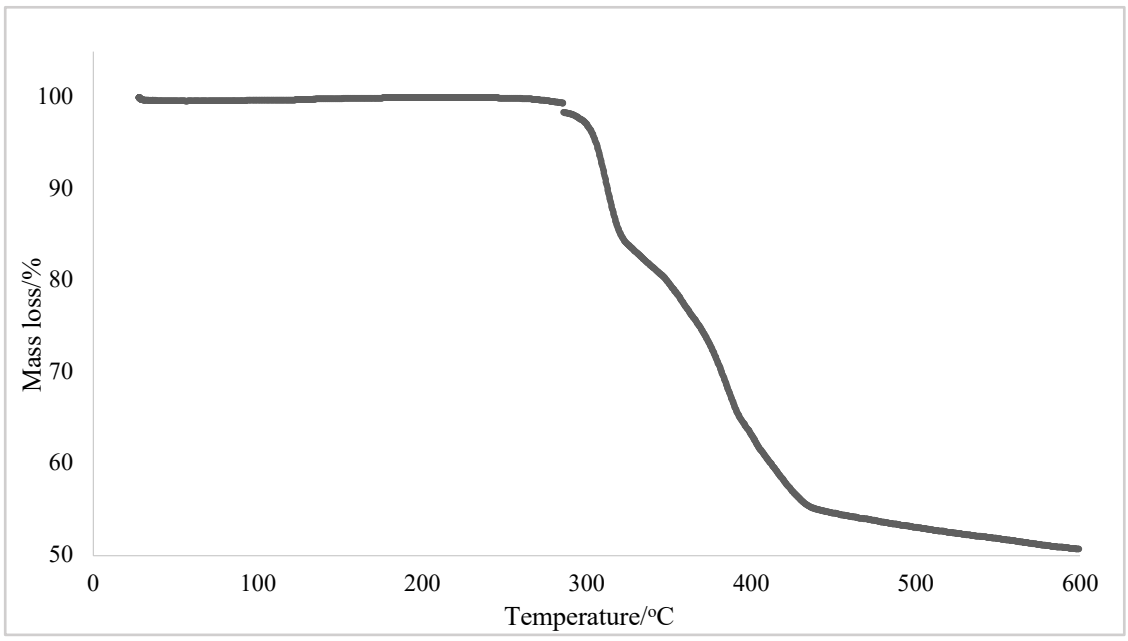


Figure 4.8. Percentage mass loss (%) of **1Er** as a function of temperature (°C) measured using Thermogravimetric Analysis (TGA).

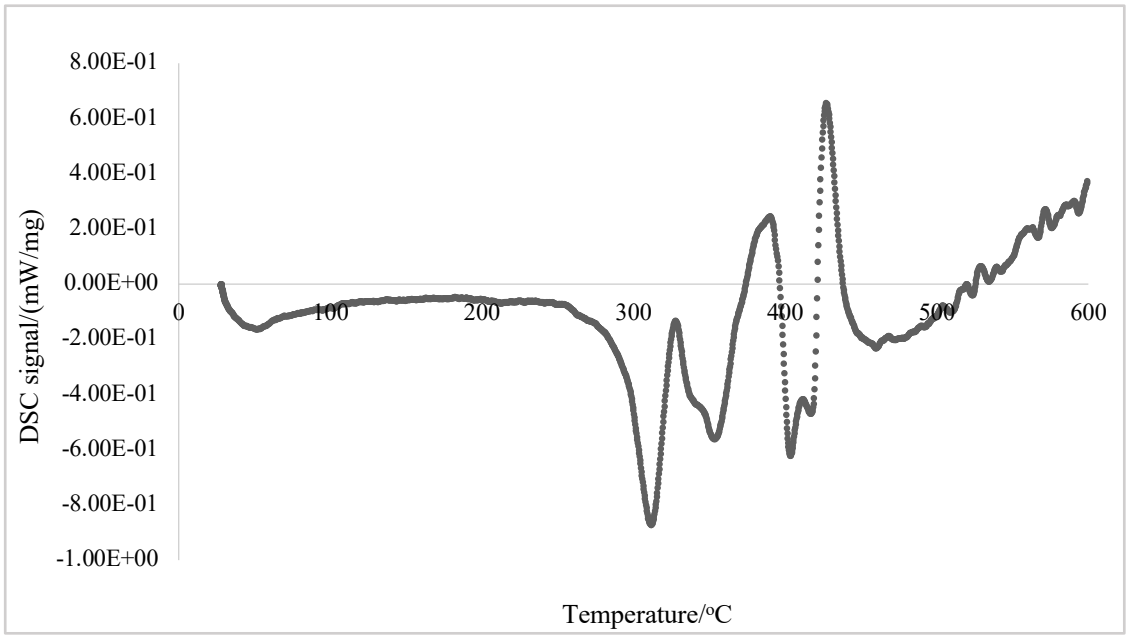


Figure 4.9. Heat capacity (mW/mg) of **1Er** as a function of temperature (°C) using Differential Scanning Calorimetry (DSC).

4.1.5. Infrared Spectra

The infrared spectrum of **1Er** features a weak peak at ~3500 cm^{-1}, suggestive of a N-H stretch in the material consistent with the dimethylammonium molecule. (See Figure 4.10). The moderately intense peaks around 2900-3000 cm^{-1} consistent with C-H stretching vibration while the more intense peak at ~800 cm^{-1} and weaker peaks around 1300-1450 cm^{-1} are consistent with a C-H bending vibration. The intense peak at 1500 cm^{-1} and weakly intense peak at ~800 cm^{-1} is suggestive of a C-O stretching vibrations in which the former is typically observed with materials containing carbonyl functional groups, such as the formate and oxalate ligands.

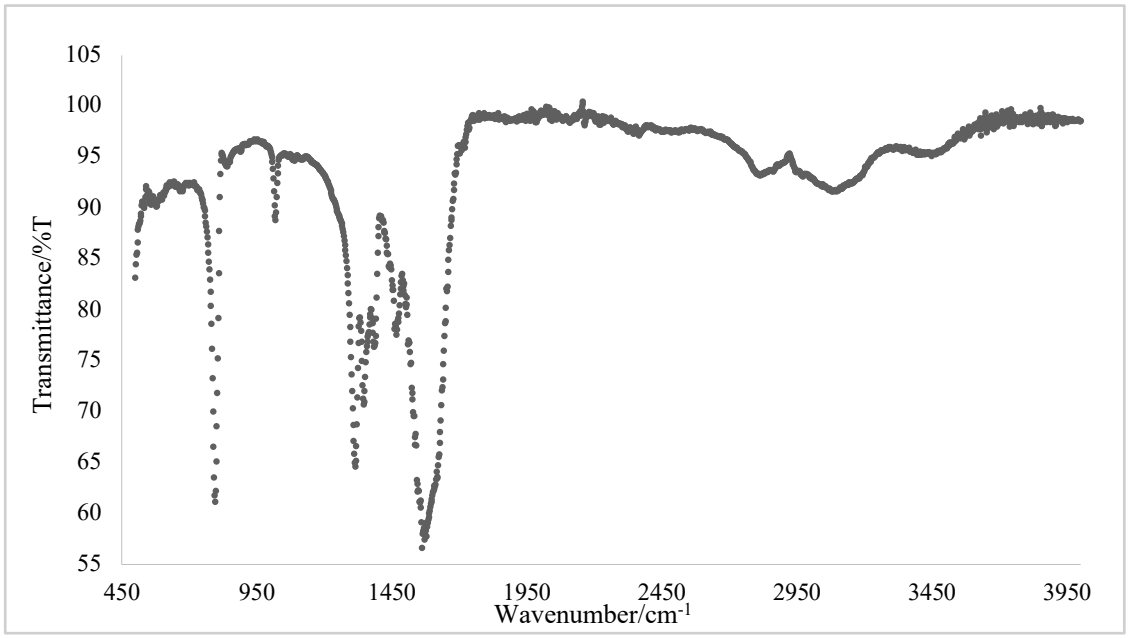


Figure 4.10. IR spectrum of **1Er**.

4.1.6. Conclusion

To conclude, this novel phase has been charactersied showing no phase transition between room temperature and 90 K, as well as the dimethylammonium, guest molecule remaining ordered up to 500 K. This material is paramagnetic but suggets antiferromagnetic interactions becoming prominent on cooling, and is thermally stable up to ~288 °C.

4.2 Structural Determination and Physical Properties of the $((CH_3)_2NH_2)Ln(C_2O_4)_{1.5}(HCO_2)$ Family

A novel series of compounds was synthesised to further explore the structural properties of mixed-ligand perovskite-like MOFs. A series was created with the inclusion of four different lanthanides: Tb, Dy, Ho and Er, as mentioned in Chapter 3, and these will hereafter be referred to as **2Tb**, **3Dy**, **4Ho** and **5Er**. **5Er** was the first in the series that was formed, and therefore will be discussed in detail.

4.2.1 Crystal Structures

White single crystals produced were of only ~100 microns in size in all dimensions for all four isostructural members of the series. SCXRD measurements were collected at both room temperature and 100 K and all systems were found to belong to space group *Cmce* with orthorhombic symmetry at both temperatures (see Tables 4.6 and 4.7). Interestingly, **4Ho** and **5Er** show evidence of weak reflections consistent with modulation of the basic structure described here. Unfortunately, in all members the A-site cation species required to be monovalent for charge balance, is not visible in the X-ray crystal structure, displayed in Figure 4.11 and 4.12. Unlike **1Er** all members have one lanthanide atom in the asymmetric unit which adopt a distorted square antiprism polyhedra and all formate ligands bridging these polyhedra (see Tables 4.7 and 4.8 for bond distances and angles) in an *anti-anti* formation. Also within the asymmetric units of all four members, are six oxygen atoms, three carbon atoms and one hydrogen atom, which comprise 2 x 0.5 oxalate ligands and 1 formate ligand. (See Figure 4.13).

Table 4.6. Crystallographic information of **2Tb**, **3Dy**, **4Ho** and **5Er** at 293 K.

	2Tb	**3Dy**	**4Ho**	**5Er**
Empirical Formula	$TbNC_6O_8H_9$	$DyNC_6O_8H_9$	$HoNC_6O_8H_9$	$ErNC_6O_8H_9$
Molecular Weight/g mol^{-1}	382.074	385.644	388.074	390.404
Crystal System	Orthorhombic	Orthorhombic	Orthorhombic	Orthorhombic
Space Group	*Cmce*	*Cmce*	*Cmce*	*Cmce*
Radiation	Mo Kα, λ = 0.71 Å	Mo Kα, λ = 0.71 Å	Mo Kα, λ = 0.71 Å	Mo Kα, λ = 0.71 Å
Temperature	293 K	293 K	293 K	293 K
Lattice parameters	a = 11.7797(11) Å b = 12.9131(17) Å c = 15.8828(19) Å α = 90° β = 90° γ = 90°	a = 11.7341(6) Å b = 12.9072(5) Å c = 15.8646(8) Å α = 90° β = 90° γ = 90°	a = 11.6610(2) Å b = 12.8820(7) Å c = 15.4450(5) Å α = 90° β = 90° γ = 90°	a = 11.6176(5) Å b = 12.8177(6) Å c = 15.8531(6) Å α = 90° β = 90° γ = 90°
Cell volume/Å^3	2416.0(5)	2402.75(19)	2320.1(15)	2360.70(17)
Density/g cm^{-1}	1.8472	1.8773	1.9579	1.9378
Z value	8	8	8	8
μ/cm^{-1}	28.971	33.578	50.162	13.318
Reflections	3197/1217	4928/1233	2417/1171	4413/1163
R_{int}	0.0504	0.0507	0.0600	0.0475
Parameters Refined	71	71	71	70
R_1, wR_2 (all)	0.1429, 0.3910	0.0743, 0.2192	0.1406, 0.3266	0.0701, 0.2214
R_1, wR_2 (obs)	0.0995, 0.2990	0.0682, 0.2113	0.0920, 0.3266	0.0663, 0.2142
χ^2	1.520	1.100	1.021	1.150

The bond lengths and angles of the formate and oxalate ligands of all members of the series are only moderately distorted from ideal geometry (see Tables 4.9 and 4.10 for **5Er**). The average *Ln*-O bond lengths for **2Tb**, **3Dy**, **4Ho** and **5Er** range from, 2.36 Å, 3.35 Å, 2.32 Å and 2.33 Å respectively, and given the atomic radii of these 3+ ions the distances should decrease at 0.01 Å from **2Tb** to **5Er**, however **5Er** has some deviation from this trend [115]. Minor distortions of the LnO_8 coordination polyhedra and organic ligands are seen in **2Tb**, **3Dy** and **4Ho** (see Tables 4.7 and 4.8 and Tables A.1-6).

Formate ligands connect the lanthanide sites along the *b*-axis while oxalate ligands connect the lanthanide polyhedra along the *a*-axis and *c*-axis. Interestingly, along the *c*-axis oxalate are only present at alternate binding sites resulting in larger cavities which may play a key role in the disorder of the A-site cation that prevents it being seen crystallographically. Initially the A-site cation was thought to be hydronium (H_3O^+) but as indicated by microanalysis and INS the identity is more likely to be dimethylammonium, see Sections 4.2.2 and 4.2.3, forming from the decomposition of DMF at higher temperatures.

Table 4.7. *Ln*-O bond lengths in **2Tb**, **3Dy**, **4Ho** and **5Er** at 293 K.

Tb-O	**Dy-O**	**Ho-O**	**Er-O**
Tb-O3B: 2.42(2) Å	**Dy-O3B**: 2.395(10) Å	**Ho-O1B**: 2.20(2) Å	**Er-O1B**: 2.287(13) Å
Tb-O3A: 2.45(3) Å	**Dy-O3A**: 2.389(11) Å	**Ho-O3A**: 2.38(2) Å	**Er-O1A**: 2.277(14) Å
Tb-O1A: 2.30(3) Å	**Dy-O1A**: 2.325(14) Å	**Ho-O2**: 2.35(2) Å	**Er-O2B**: 2.371(9) Å
Tb-O1B: 2.24(3) Å	**Dy-O1B**: 2.268(14) Å	**Ho-O1A**: 2.287(14) Å	**Er-O2A**: 2.350(10) Å
Tb-O2B: 2.370(15) Å x2	**Dy-O2A**: 2.357(9) Å x2	**Ho-O2A**: 2.342(13) Å x2	**Er-O3A**: 2.331(8) Å x2
Tb-O2A: 2.370(19) Å x2	**Dy-O2B**: 2.371(9) Å x2	**Ho-O2B**: 2.329(14) Å x2	**Er-O3B**: 2.359(8) Å x2

Table 4.8. O-Er-O bond angles in **5Er** at 293 K.

O1B-Er-O2B: 70.2(4)°	**O1A-Er-O2B**: 142.0(4)°	**O3A-Er-O3A**: 146.4(4)°
O1B-Er-O2A: 138.6(4)°	**O1A-Er-O2A**: 73.6(4)°	**O3B-Er-O3B:** 75.9(5)°
O1A-Er-O1B: 147.8(4)°	**O2A-Er-O2B**: 68.4(3)°	**O1B-Er-O3B**: 79.4(4)° x2
O3A-Er-O3B: 68.6(3)° x2	**O1A-Er-O3A**: 98.0(2)° x2	**O1B-Er-O3A**: 90.9(3)° x2
O3B-Er-O2B: 131.3(3)° x2	**O3A-Er-O3B**: 144.4(3)° x2	**O3A-Er-O2A**: 78.3(2)° x2
O3A-Er-O2B: 74.6(2)° x2	**O2A-Er-O3B**: 130.1(3)° x2	**O1A-Er-O3B**: 75.3(4) x2

Table 4.9. Range of other bond lengths in **5Er** at 293 K.

Bond	Range in length/Å
C-O (formate)	1.18(2)-1.19(2)
C-O (oxalate)	1.215(16)-1.253(15)

Table 4.10. Range of other bond angles in **5Er** at 293 K.

Angle	Range in Angle/°
O-C-O (formate)	129.8(18)
O-C-O (oxalate)	127.2(11)-128.6(12)

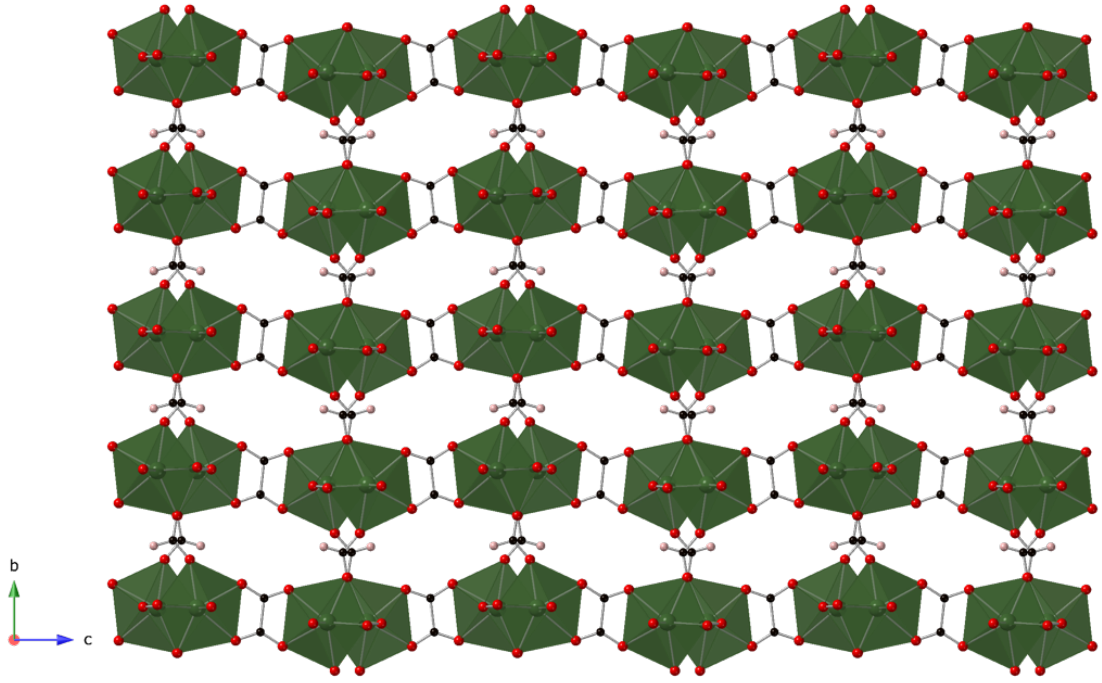


Figure 4.11. Crystal structure of **5Er** at 293 K along the *a*-axis. Erbium sites shown in dark green, C: black, O: red and H: pink.

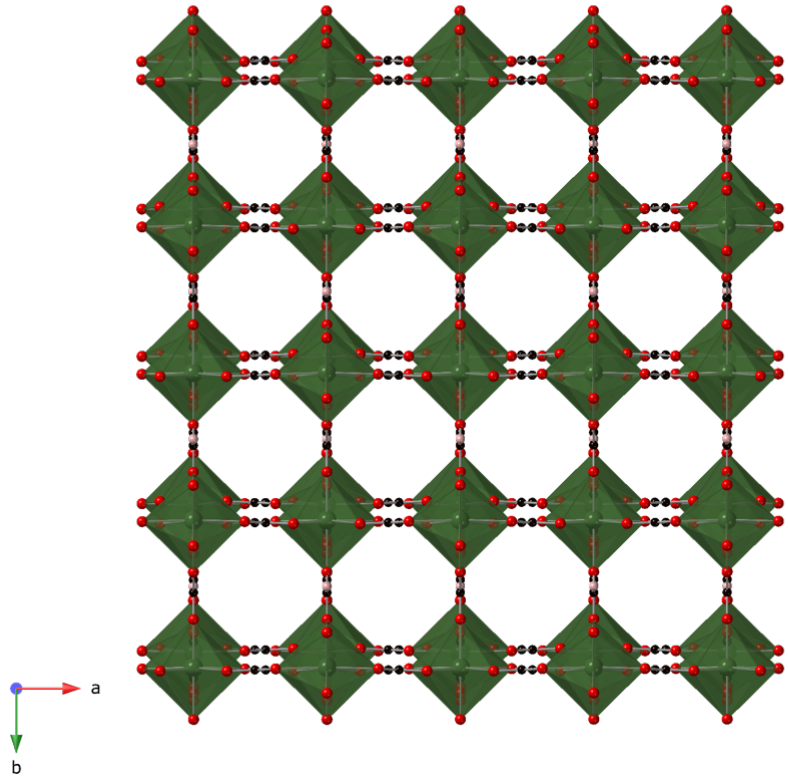


Figure 4.12. Crystal structure of **5Er** at 293 K along the *c*-axis. Colour scheme same as in Figure 4.11.

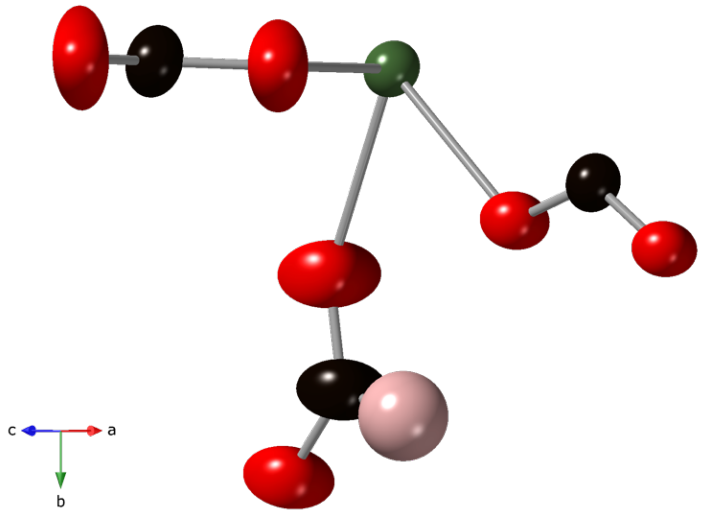


Figure 4.13. Asymmetric unit of **5Er** at 293 K, colour scheme same as in Figure 4.11. S

SQUEEZE was utilised for **3Dy**, **4Ho** and **5Er** in order to account for dimethylammonium cation within the pores [116, 117]. The number of electrons in the model determined by SQUEEZE is higher than expected, see Table 4.11. This could account for both dimethylammonium cations along with solvent, or the method overestimated the electron density.

Table 4.11. SQUEEZE results of **3Dy**, **4Ho** and **5Er** at both 100 K and 293 K.

Data set:	**3Dy at 100 K**	**3Dy at 293 K**	**4Ho at 100 K**	**4Ho at 293 K**	**5Er at 100 K**	**5Er at 293 K**
Electrons per cell	286.5	323.2	349.7	313.4	315.6	274.7
Expected DMA per cell	216.0	216.0	216.0	216.0	216.0	216.0
Percentage increase (%):	32.64	49.63	61.90	45.09	46.10	27.18
R_1	0.7003	0.9156	0.8757	0.6521	0.8590	0.9413
wR_2	0.9126	0.9667	0.9602	0.8857	0.9431	0.9644
χ^2	1.092	1.074	1.102	1.090	1.051	1.124

4.2.2 Determination of Bulk Composition using Powder X-ray Diffraction and Microanalysis

Le Bail fits to PXRD patterns obtained of the $AEr(C_2O_4)_{1.5}(HCO_2)$ phase confirm the high level of purity of the sample obtained as only very weak peaks in the experimental pattern are not fitted in the calculated pattern (see Figure 4.14). These conditions were consequently used hereafter to scale up the yield for further analysis by production of multiple batches. Similar results were obtained for fits to PXRD data from **2Tb**, **3Dy** and **4Ho**, confirming the level of high level of phase purity (see Figures A.14-16). **2Tb** was the least pure phase out of the three members, with a slight unidentified impurity which could not be removed by optimisation of the synthetic conditions within the scope of this project.

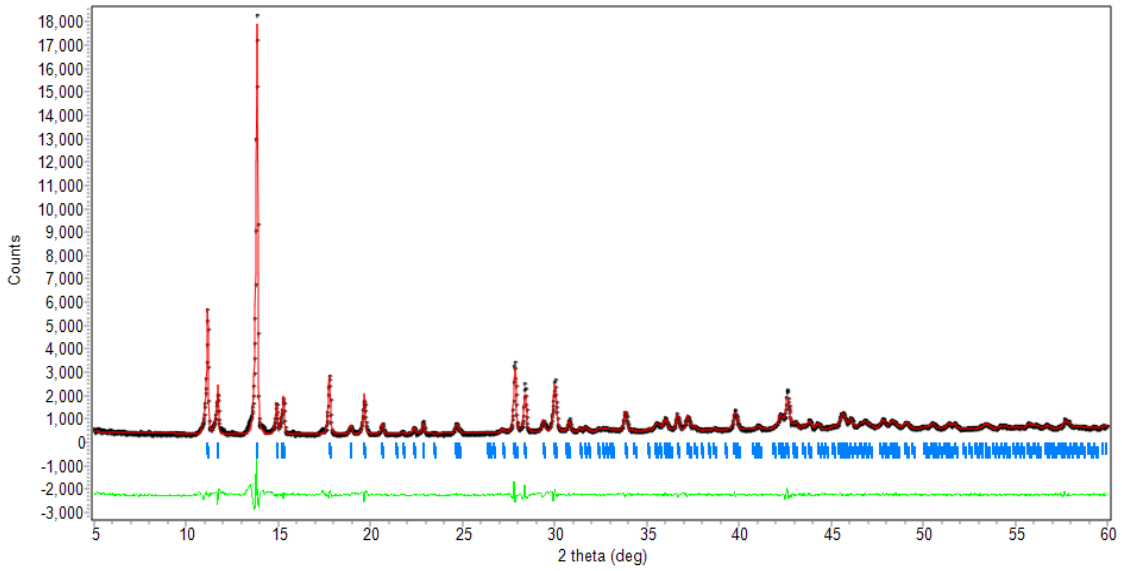


Figure 4.14. Le Bail refinement of **5Er**. R_p = 5.390, R_{wp} = 7.868 and χ^2 = 4.283. Lattice parameters: *a* = 11.63(13), *b* = 12.876(10) and *c* = 15.97(13). Colour scheme same as in Figure 3.5.

As mentioned in Section 4.2.1, the A-site cation was initially thought to be hydronium (H_3O^+) because the species could not be seen with X-ray diffraction and water may easily enter the system as a result of the metal salts and formic acid used containing this. Elemental microanalysis was utilised and revealed that there was nitrogen present in all members of this series suggesting that instead, dimethylammonium was more likely to be this species, see Table 4.12. The presence of dimethylammonium in the pores of **2Tb**, **3Dy**, **4Ho** and **5Er** indicates this must be greatly disordered, which may relate to the significantly larger pores of these phases compared to **1Er**.

Table 4.12. Microanalysis results of **2Tb**, **3Dy**, **4Ho** and **5Er**.

2Tb	**If A = H_3O^+**	**If A = DMA**	**Result**
C (%):	13.53	18.86	18.96
H (%):	1.14	2.37	2.54
N (%):	0	3.66	3.52
3Dy	**If A = H_3O^+**	**If A = DMA**	**Result**
C (%):	13.40	18.69	19.29
H (%):	1.12	2.35	2.50
N (%):	0	3.63	3.69
4Ho	**If A = H_3O^+**	**If A = DMA**	**Result**
C (%):	13.31	18.57	19.26
H (%):	1.12	2.34	2.49
N (%):	0	3.61	3.76
5Er	**If A = H_3O^+**	**If A = DMA**	**Result**
C (%):	13.22	18.45	18.64
H (%):	1.11	2.32	2.36
N (%):	0	3.59	3.64

Efforts were made to incorporate gadolinium (Gd) into this series, but numerous attempts were all unsuccessful in producing a pure phase and yielding single crystals. Remembering that **2Tb** was of lowest purity out of the four in the series, and with this in mind, it can be deduced that the increasing size of atomic radii leads to increasing difficulty in obtaining analogues of this series.

4.2.3. Inelastic Neutron Scattering and Infrared Spectra

An INS spectrum of one member of the series, **5Er**, was collected (see Figure 4.15) to help support the identification of the A-site cation. INS is highly sensitive to hydrogen atoms, so intense peaks produced in an INS spectrum represent vibration modes where hydrogen atoms are involved. The data can be interpreted similarly to IR data although INS is more beneficial due to its lack of selection rules and that it enables lower wavenumbers to be observed. If H_3O^+ was the A-site cation, only significant peaks above 3000 cm^{-1} would be expected, arising from O-H stretches. Similarly, these can be assigned to N-H stretching vibration modes. Additionally, strong peaks are observed in the region of ~ 1500-1600 cm^{-1} which are more clearly suggestive of N-H bending motions. The peaks in the region of ~800-1300 cm^{-1} are suggestive of C-H and, to a lesser extent given the techniques sensitivity to them, C-N vibration modes. Using only these conclusions so far, it can be thought with confidence that dimethylammonium occupies the pores, as if the species was H_3O^+ no N-H or C-N vibration modes would be observed. All the functional groups combined are characteristic of the bonds within dimethylammonium, formate ligands and oxalate ligands.

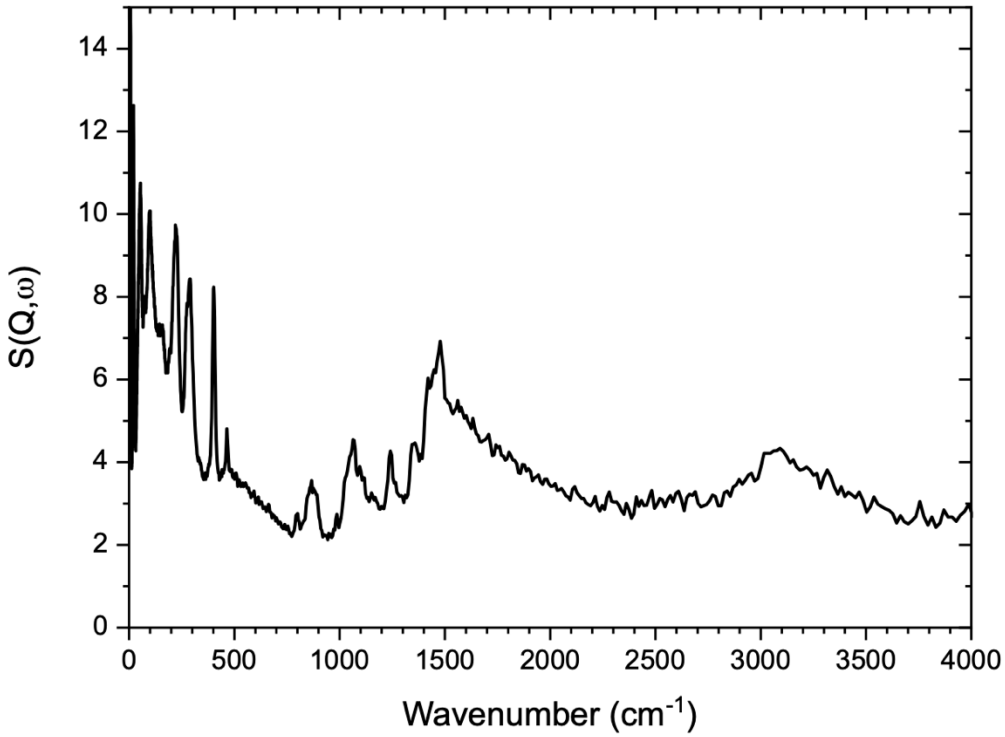


Figure 4.15. INS data collected on TOSCA at ISIS.

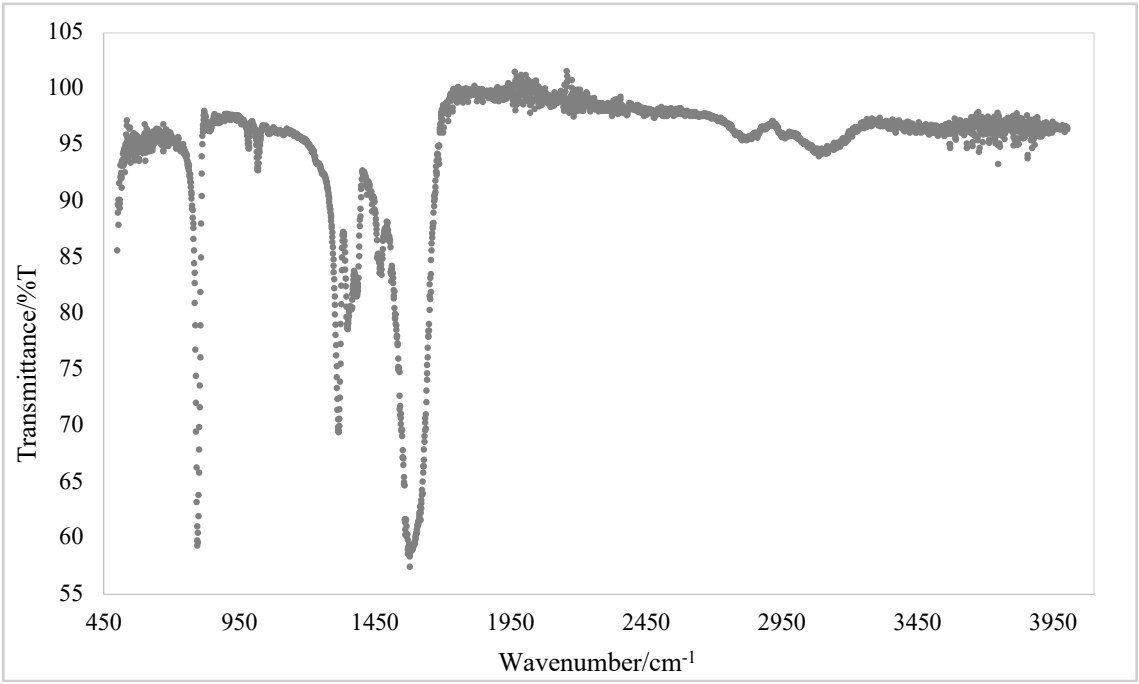


Figure 4.16. IR spectrum of **5Er.**

Infrared spectra of the $((CH_3)_2NH_2)Ln(C_2O_4)_{1.5}(HCO_2)$ phases were obtained when *Ln* = Dy, Ho and Er. These were all similar so only **5Er** will be described here, see Figures A.32 and 33. The spectra of **5Er** (see Figure 4.16) is almost identical to that of **1Er** in Figure 4.10 due to the similar molecular bonds in this material. The peak ~ 3100 cm^{-1} is

suggestive of an N-H stretching vibration mode, although it is very weak. Peaks ~2800-2900 cm^{-1} are suggestive of C-H stretching vibrations, while the peaks ~1300-1450 cm^{-1} and the very intense peak at ~800 cm^{-1} are suggestive of C-H bending modes. The intense peaks ~1500 cm^{-1} and weaker peak ~1000 cm^{-1} are characteristic and consistent with a C-O stretching mode.

4.2.4. Magnetic Properties

Figure 4.17 clearly shows paramagnetic behaviour, displayed by the decreasing magnetic susceptibility as a function of increasing temperature, as well as the overlapping ZFC and FC data. However, the insert, much like that in **1Er** shows a decrease in χT on cooling, which also suggest short-range antiferromagnetic interactions becoming prominent on cooling. This phenomenon is also seen in **2Tb**, **3Dy** and **4Ho**, see appendix for data.

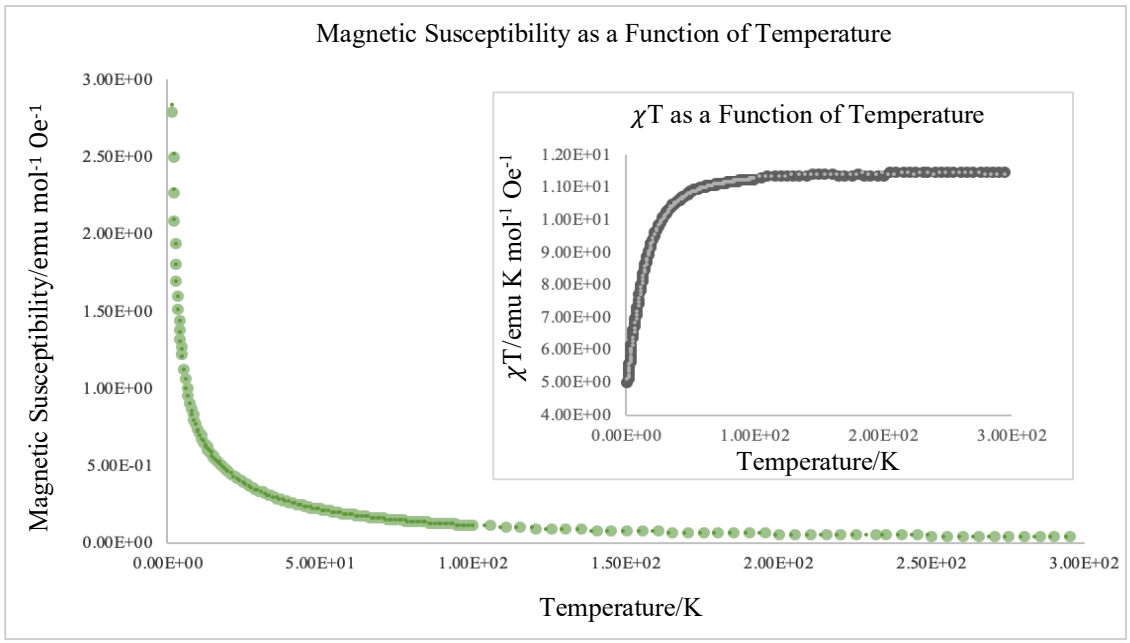


Figure 4.17. Magnetic susceptibility as a function of temperature of **5Er**. The insert is of magnetic susceptibility multiplied by T as a function of T. Pale green and dark grey: ZFC, dark green and pale grey: FC.

The linear relationship between inverse magnetic susceptibility and increasing temperature shown in Figure 4.18 displays behaviour characteristic of a Curie-Weiss paramagnet with overlapping FC and ZFC plots also. The Curie-Weiss fits were used to calculate the Curie constant, Weiss temperature and effective magnetic moment of the

erbium centre, these were 11.66, -4.31 K and 9.65 u_B respectively. This calculated negative Weiss temperature also indicates the emergence of antiferromagnetic interactions on cooling as suggested by the insert in Figure 4.17. As with **1Er**, the effective magnetic moment was approximately what is expected from an erbium atom also.

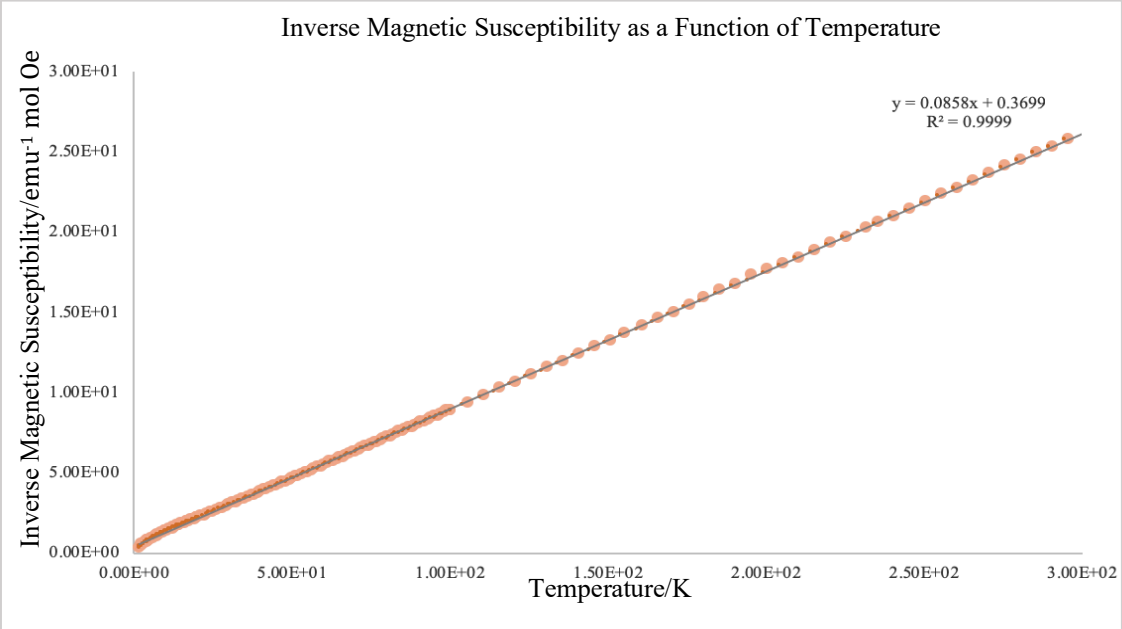


Figure 4.18. Curie-Weiss plot of **5Er**. Pale orange: ZFC and dark orange: FC.

Figure 4.19 indicates magnetisation increases linearly with applied magnetic fields and approaches saturation above 10 kOe, consistent with paramagnetic behaviour. Interestingly, the magnetisation continues to very gradually increase above 10 kOe. There is also an absence of a hysteresis loop.

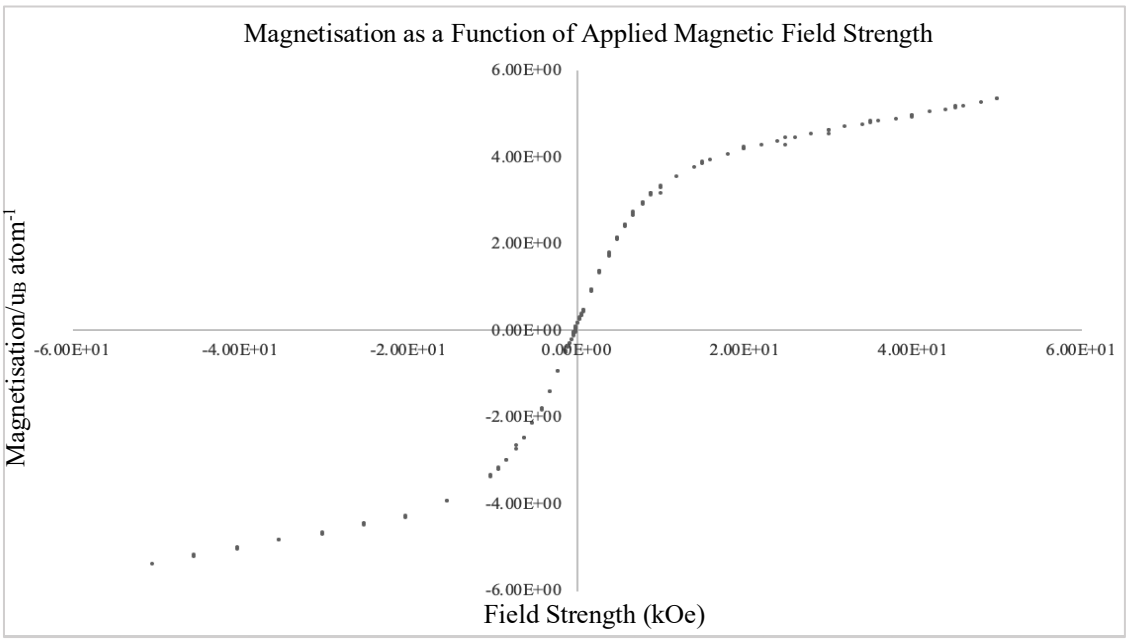


Figure 4.19. Magnetisation as a function of applied magnetic field strength of **5Er**.

The magnetic properties were also measured for **2Tb**, **3Dy** and **4Ho** and all three showed characteristic paramagnetic behaviour similarly to **5Er**, see appendix. Curie-Weiss plots display a linear relationship between the inverse magnetic susceptibility increasing with increasing temperature for all members. From these plots, see appendix, the Curie constants were calculated as 10.81, 12.08 and 12.20 for **2Tb**, **3Dy** and **4Ho** respectively. The associated Weiss temperatures were -4.50 K, -4.15 K and -6.54 for **2Tb**, **3Dy** and **4Ho** respectively. Effective magnetic moments of these metal centres were calculated to be 9.30 u_B, 9.83 u_B and 9.88 u_B, for **2Tb**, **3Dy** and **4Ho** respectively, all under the values of 9.72, 10.65 and 10.6 u_B, respectively, expected from Russel-Saunders coupling. This discrepancy may suggest that there are some impurities in the samples which were not readily detected by PXRD that reduce the magnetic moment from that which is expected. Plots of χT as a function of temperature, shown as inserts, also suggest short-range antiferromagnetic interactions arising at low temperatures, which is also suggested by the negative Weiss temperatures.

4.2.5. Thermal Stability

2Tb, **3Dy**, **4Ho** and **5Er** are thermally stable up until ~ 300 °C, ~285 °C, ~290 °C and ~300 °C where they decompose (see Figures 4.19, A.26, 28, 30) endothermically, (see Figures 4.20 A.27, 29 and 31). As mentioned in Section 2.6, TGA-DSC of **4Ho** was collected with an isothermal step at 30°C for 30 minutes, this was to study whether any

surface water or other solvent was present, and this showed no significant mass loss up until the temperature of decomposition indicative of a solvent evaporating.

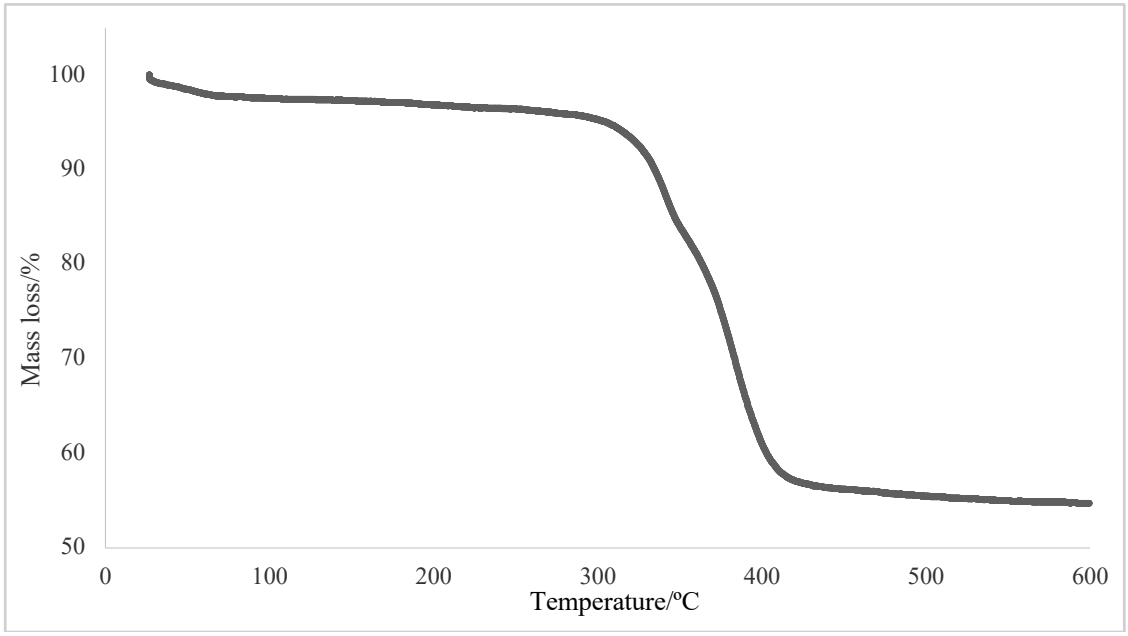


Figure 4.20. Percentage mass loss (%) of **5Er** as a function of temperature (°C) measured using Thermogravimetric Analysis (TGA).

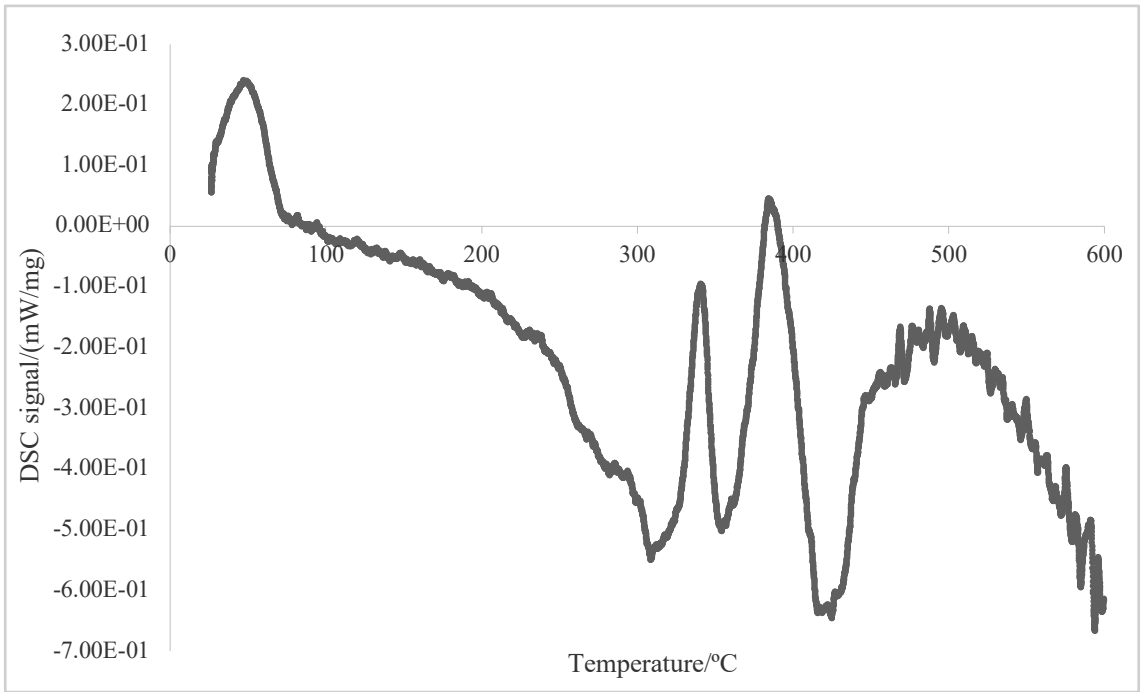


Figure 4.21. Heat capacity (mW/mg) of **5Er** as a function of temperature (°C) using Differential Scanning Calorimetry (DSC).

4.2.6. Conclusion

To conclude, a novel family of mixed-ligand perovskite-like MOFs have been successfully synthesised with the stoichiometry A*Ln*$(C_2O_4)_{1.5}(HCO_2)$ where the A-site cation is dimethylammonium and *Ln* = Tb, Dy, Ho and Er. Crystallographically the A-site cation cannot be seen, most likely due to the highly disordered nature of it, but inelastic neutron scattering, microanalysis and infrared spectroscopy highly suggest that the identity of the A-site cation is dimethylammonium. All these systems are paramagnetic to low temperature with antiferromagnetic interactions becoming prominent on cooling, and are thermally stable up to ~ 300 °C, ~285 °C, ~290 °C and ~300 °C for **2Tb**, **3Dy**, **4Ho** and **5Er**, respectively.

Chapter 5

Conclusion and Future Work

The work in this thesis can be split into work of the known $NH_4M(HCO_2)_3$ phases and the new $((CH_3)_2NH_2)Ln(C_2O_4)_x(HCO_2)_y$ phases. With regards to the former, this work probes the disorder of the ammonium cation below the characteristic transition temperatures of two isostructural AMFFS, **1Mn** and **2Zn**. Neutron diffraction was conducted while these systems were in the lower symmetry $P6_3$ phase, at 22 K, to identify crystallographically if any static disorder remained within the cations occupying the pores of the anionic framework. Single crystal neutron diffraction showed no disorder of the cation in **2Zn** but interestingly, disorder within **2Zn** originated from a hydrogen atom split from a formate linker, split between two sites. This suggests there is no clear crystallographic disorder of the NH_4^+ molecules that can be linked to relaxor-like properties of this material, although the disorder of the formate may. Due to size limitations of the single crystals synthesised for **1Mn**, the quality of the data cannot be used to clearly conclude this hypothesis for this phase. In particular it was also not possible to model one of the hydrogen atoms on one out of the three ammonium cations within the asymmetric unit, so it cannot be deduced whether this hydrogen atoms possesses disorder or not. QENS was used complementary to this to probe dynamical disorder and data were collected as the materials were warmed through T_C. Plots of MSD, for both members, as a function of temperature showed a degree of motion in the hydrogen atoms leading up to the transition temperature. Suggesting there are significant dynamics in the low temperature phase, this may be, for example, correspond to the hydrogen atoms in NH_4^+ undergoing a 3-fold rotation which would be consistent with the results obtained crystallographically. Plots of EISF as a function of Q show that at higher Q values, the degree of QENS increases progressively, and shows identical downwards trends for both (002) and (004) settings, suggesting the dominant motion of hydrogen atoms is not changing as the systems are warmed through T_C despite an increase in the amount of motion. This is more suggestive of remnant dynamical disorder as these motions cannot be seen crystallographically, however the nature and rotation axis of these motions is still unknown. This is a result of no clear minimum identified in the EISF. Further spectroscopic studies, such as solid-state NMR on this would be necessary to gain a full understanding of the dynamics of these

materials, as well as exploring the crystallographic details of other analogues of the $NH_4M(HCO_2)_3$ family using neutron diffraction. A novel mixed-ligand perovskite-like lanthanide MOF, $(DMA)Er(C_2O_4)(HCO_2)_2$ was characterised giving valuable information about the system and variable temperature SCXRD measurements show that the dimethylammonium cation remain ordered up to 500 K giving promise for more ordered systems above room temperature, potentially key to developing ferroelectric Metal-Organic Frameworks with properties at useful temperatures. SQUID data revealed the material was paramagnetic but short-range antiferromagnetic interactions become apparent on cooling and the system is thermally stable up to ~ 288 °C. Another novel series of mixed-ligand perovskite-like lanthanide MOFs were synthesised incorporating four lanthanides: Tb, Dy, Ho and Er, creating a new family of $(DMA)Ln(C_2O_4)_{1.5}(HCO_2)$ compounds. All four analogues displayed no phase transition between 100 K and room temperature and were all thermally stable up to ~285-300 °C. While SQUID data revealed all were paramagnetic with short-range antiferromagnetic interactions becoming apparent on cooling. Further efforts could be made to incorporate a variety of amines within the pores to explore whether this phenomenon appears in analogues of this family. This could be attempted be replacing the dimethylammonium solvent with other polar aprotic solvents that do not decompose to make dimethylamine. Further studies could investigate the limit of lanthanides which could be incorporated into this family, but as mentioned previously, the difficulty increases as the size of the lanthanide increases. Attempts should be made to understand the structural modulation exhibited by some of the materials, namely **4Ho** and **5Er**, which may provide further insights into the molecular A-site cation.

Bibliography

1. S. Pullen and G. H. Clever, *Acc. Chem. Res.*, 2018, **51**, 3052-3064.
2. B. Valizadeh, T. N. Nguyen and K. C. Stylianou, *Polyhedron*, 2018, **145**, 1-15.
3. V. F. Cheong and P. Y. Moh, *Mater. Sci. Tech.*, 2018, **34**, 1025-1045.
4. X. Lian, L. Xu, M. Chen, C. Wu, W. Li, B. Huang and Y. Cui, *J. Nanosci. Nanotechno.,* 2019, **19**, 3059-3078.
5. D-X. Xue, Q. Wang and J. Bai, *Coord. Chem. Rev.*, 2019, **378**, 2-16.
6. R. J. Drout, L. Robinson and O. K. Farha, *Coord. Chem. Rev.*, 2019, **381**, 151-160.
7. W. Li, A. Thirumuragan, P. T. Barton, Z. Lin, S. Henke, H. H-M. Yeung, M. T. Wharmby, E. G. Bithell, C. J. Howard and A. K. Cheetham, *J. Am. Chem. Soc*., 2014, **136**, 7801-7804.
8. J. F. Scott and C. A. Paz de Araujo, *Science*, 1989, **246**, 1400-1405.
9. D. Li and D. A. Bonnell, *Annu. Rev. Mater. Res.*, 2008, **38**, 351-368.
10. G. Rogez, N. Viart and M. Drillon, *Angew. Chem. Int. Ed*., 2010, **49**, 1921-1923.
11. M. Mączka, A. Pietraszko, B. Macalik and K. Hermanowicz, *Inorg. Chem.,* 2014, **53**, 787-794.
12. R. Shang, G-C. Xu, Z-M. Wang and S. Gao, *Chem. Eur. J.*, 2014, **20**, 1146-1158.
13. L. E. Smart and E. A. Moore, *Solid State Chemistry: An Introduction*, Chapman and Hall/CRC, New York, 2012.
14. A. Chauhan, S. Patel, R. Vaish and C. R. Bowen*, Materials*, 2015, **8**, 8009-8031.
15. Y. Yuan, Z. Xiao, B. Yang and J. Huang, *J. Mater. Chem. A.*, 2014, **2**, 6027-6041.
16. G. Rijnders and D. H. A. Blank, *Nature*, 2005, **433**, 369-370.
17. X. Solans, C. Gonzalez-Silgo and C. Ruiz-Pérez*, J. Solid State Chem.*, 1997, **131**, 350-357.
18. J. Valasek, *Phys. Rev.,* 1921, **17**, 475-481.
19. H. Mueller, *Phys. Rev*., 1940, **57**, 829-839.
20. F. Li, S. Zhang, D. Damjanovic, L-Q. Chen and T. R. Shrout, *Adv. Funct. Mater.,* 2018, **28**, 1801504-1801525.
21. A. von Hippel, R. G. Breckenridge, F. G. Chelsey and L. Tisza, *Ind. Eng. Chem*., 1946, **38**, 1097-1109.
22. M. Panjan, *Ferroelectric and Ferroelectric Domains*, University of Ljubljani, 2003.
23. E. A. Donlan, H. L. B. Boström, H. S. Geddes, E. M. Reynolds and A. L. Goodwin, *Chem. Commun*., 2017, **53**, 11233-11236.
24. M. Mączka, A. Pietraszko, L. Macalik, A. Sieradzki, J. Trzmiel and A. Pikul, *Dalton Trans.,* 2014, **43**, 17075-17084.
25. G. A. Smolenskii and A. I. Agranovskaya, *Sov. Phys. Solid State*, 1959, **1**, 1429-1437.
26. R. K. Pattnaik and J. Toulouse, *Phys. Rev. B*, 1999, **60**, 7091-7098.
27. N. N. Kolpakova, P. Czarnecki, W. Nawrocik, M. P. Shcheglov and A. O. Lebedev, *Ferroelectrics*, 2003, **291**, 125-132.
28. N. Abhyankar, M. Lee, M. Foley, E. S. Choi, G. Strouse, H. W. Kroto and N. S. Dalal*, Phys. Status Solidi RRL*, 2016, **10**, 600-605.

29. A. R. West, *Solid State Chemistry and Its Applications,* John Wiley & sons, Chichester, 2014.
30. William N. Parker, Lancaster Pa., 149 044, 1950, US Pat., 2 655 623, 1953.
31. X. Li, A. Lee, S. A. Razavi and H. Wu*, MRS BULLETIN*, 2018, **43**, 970-977.
32. N. A. Hill, *J. Phys. Chem. B,* 2000, **104**, 6694-6709.
33. P. Z. Moghadam, A. Li, S. B. Wiggin, A. Tao, A. G. P. Maloney, P. A. Wood, S. C. Ward and D. Fairen-Jimenez*, Chem. Mater.,* 2017, **29**, 2618-2625.
34. Z. Ajoyan, P. Marino and A. J. Howarth*, CrystEngComm.,* 2018, **20**, 5899-5912.
35. G. Xu, B. Ding, L. Shen, P. Nie, J. Han and X. Zhang*, J. Mater. Chem. A.,* 2013, **1**, 4490-4496.
36. W. Shi, X. Xu, L. Zhang, W. Liu and X. Cao*, Func. Mater. Lett.,* 2018, **11**, 1830006, 1-9.
37. G. Lan, K. Ni and W. Lin*, Coord. Chem. Rev.,* 2019, **379**, 65-81.
38. Goldschmidt V. M., *Naturwissenschaften*, 1926, **14**, 477-485
39. G. Kieslich, S. Sun and A. K. Cheetham*, Chem. Sci.,* 2015, **6**, 3430-3433.
40. Y. Li, H. Xu, H. Huang, L. Gao, Y. Zhao and T. Ma, *Electrochim. Acta*, 2017, **254**, 148.
41. M. Yoon and D. Moon, *Microporous and Mesoporous Materials*, 2015, **215**, 116-122.
42. M. Kondo, T. Yoshitomi, K. Seki, H. Matsuzaka and S. Kitagawa, *Angew. Chem. Int. Ed. Engl*., 1997, **36**, 1725-1727.
43. R-B. Lin, S. Xiang, H. Xing, W. Zhou and B. Chen, *Coord. Chem. Rev.*, 2019, **378**, 87-103.
44. S.C. King, R-B. Lin, H. Wang, H. D. Arman and B. Chen, *Mater. Chem. Front*., 2017, **1**, 1514-1519.
45. H. Zhang, X-W. Gao, L. Wang, X. Zhao, Q-Y. Li and X-J. Wang*, CrystEngComm*. 2019, **21**, 1358-1362.
46. T. Zhao, I. Boldog, Y. Spasojevic, A. Rotaru, Y. Garcia and C. Janiak, *J. Mater. Chem.*, 2016, 4, 6588-6601.
47. S-Y. Moon, G. W. Wagner, J. E. Mondloch, G. W. Peterson, J. B. DeCoste, J. T. Hupp and O. K. Farha*, Inorg. Chem.*, 2015, 54, 10829-10833
48. C. Y. Lee, O. K. Farha, B. J. Hong, A. A. Sarjeant, S. T. Nguyen and J. T. Hupp*, J. Am. Chem. Soc.,* 2011. **133**, 15858-15861.
49. Y. Bai, Y. Dou, L-H. Xie, W. Rutledge, J-R. Li and H-C. Zhou*, Chem. Soc. Rev.,* 2016, **45**, 2327-2367.
50. M. D. Allendorf, R. Medishetty and R. A. Fisher, *MRS BULLETIN*, 2016, **41**, 865-869.
51. S. Horike, K. Kishida, Y. Watanabe, Y. Inubishi, D. Umeyama, M. Sugimoto, T. Fukushima, M. Inukai and S. Kitagawa, *J. Am. Chem. Soc.*, 2012, **134**, 9852-9855.
52. P. Jain, A. Stroppa, D. Nabok, A. Marino, A. Rubano, D. Paparo, M. Matsubara, H. Nakotte, M. Fiebig, S. Picozzi, E. S. Choi, A. K. Cheetham, C. Draxl, N. S. Dalal and V. S. Zapf, *npj Quantum Materials*, 2016, **1**, 1-6.
53. N. A. Spaldin and M. Fiebig, *Science*, 2005, **309**, 391-392.
54. L. Zou, S. Yao, J. Zhao, D-S. Li, G. Li, Q. Huo and Y. Liu, *Cryst. Growth Des*., 2017, **17**, 3556-3561.
55. R. Liu, L. Zhao, S. Yu, X. Liang, Z. Li and G. Li, *Inorg. Chem.,* 2018, **57**, 11560-11568.
56. R. Sola-Llano, V. Martínez-Martínez, S. Furukawa, Y. Takashima and I. López-Arbeloa, *Polymers*, 2018, **10**, 188-197.

57. S. Chen, R. Shang, K-L Hu, Z-M. Wang and S. Gao, *Inorg. Chem. Front*., 2014, **1**, 83-98.
58. S. M. Bovill and P. J. Saines, *CrystEngComm*, 2015, **17**, 8319-8326.
59. J. M. M. Lawler, P. Manuel, A. L. Thompson and P. J. Saines, *Dalton Trans.*, 2015, **44**, 11613-11620.
60. G-C. Xu, X-M. Ma, L. Zhang, Z-M. Wang and S. Gao, *J. Am. Chem. Soc.*, 2010, **132**, 9588-9590.
61. G-C. Xu, W. Zhang, X-M. Ma, Y-H. Chen, L. Zhang, H-L. Cai, Z-M. Wang, R-G. Xiong and S. Gao, *J. Am. Chem. Soc.*, 2011, **133**, 14948-14951.
62. Z. Wang, K. Hu, S. Gao and H. Kobayashi, *Adv. Mater.*, 2010, **22**, 1526-1533.
63. A. V. Chitnis, H. Bhatt, M. Mączka, M. N. Deo and N. Garg, *Dalton Trans.*, 2018, **47**, 12993-13005.
64. G. Lurusso, J. W. Sharples, E. Palacios, O. Roubeau, E. K. Brechin, R. Sessoli, A. Rossin, F. Tuna, E. J. L. McInnes, D. Collison and M. Evangelisti, *Adv. Mater.*, 2013, **25**, 4653-4656.
65. R. Sibille, E. Didelot, T. Mazet, B. Malaman and M. François, *APL Mater.,* 2014, **2**, 1-7.
66. M. A. Gotthardt, S. Grosjean, T. S. Brunner, J. Kotzel, A. M. Gänzler, S. Wolf, S. Bräse and W. Kliest, *Dalton Trans.*, 2015, **44**, 16802-16809.
67. Y. Goto, H. Sato, S. Shinkai and K. Sada, *J. Am. Chem. Soc.*, 2008, **130**, 14354-14355.
68. Z-G. Gu, X-H. Zhou, Y-B. Jin, R-G. Xiong, J-L. Zuo and X-Z. You, *Inorg. Chem.,* 2007, **46**, 5462-5464.
69. A. García-Fernández, J. M. Bermúdez-García, S. Casto-García, R. Artiaga, J. López-Beceiro, M. A. Señarís-Rodríguez and M. Sánchez-Andújar*, Polyhedron 114*, 2016, **49**, 249-255.
70. W. Li, Z. Wang, F. Deschler. S. Gao, R. H. Friend and A. K. Cheetham, *Nat. Rev.*, 2017, **2**, 1-18.
71. M. Mączka, M. Ptak, A. Gągor, A. Sieradzki, P. Peksa, G. Usevicius, M. Simenas, F. F. Leite and W. Paraguassu*, J. Mater. Chem. C.*, 2019, **7**, 2408-2420.
72. T. Khan, M. A. Asghar, Z. Sun, A. Zeb, L. Li, L. Sijie, S. Zhao, C. Ji and J. Luo*, Chem. Asian J.*, 2016, **11**, 2876-2881.
73. M. Weller, T, Overton, J. Rourke and F. Armstrong, *Inorganic Chemistry*, Oxford University Press, Oxford, 2014.
74. B. Liu, H-B. Zheng, Z-M. Wang and S. Gao*, CrystEngComm.,* 2011, **13**, 5285-5288.
75. D. Feng, Y. Che and J. Zheng*, J. Rare Earth,* 2012, **30**, 798-801.
76. M. Li, B. Liu, B. Wang, Z. Wang, S. Gao and M. Kurmoo*, Dalton Trans.,* 2011, **40**, 6038-6046.
77. M. Ptak, M. Mączka, A. Gągor, P. Głuchowski and L. Macalik*, J. Mater. Chem. C,* 2016, **4**, 1019-1028.
78. T-M. Zhao, S. Chen, R. Shang, B-W. Wang, Z-M. Wang and S. Gao*, Inorg. Chem.,* 2016, **55**, 10075-10082.
79. A. Rossin, G. Giambastiani, M. Peruzzini and R. Sessoli, *Inorg. Chem*., 2012, **51**, 6962-6968.
80. M. I. Breeze, T. W. Chamberlain, G. J. Clarkson, R. Pires de Camargo, Y. Wu, J. Fonseca de Lima, F. Millange, O. A. Serra, D. O'Hare and R. I. Walton, *CrystEngComm*., 2017, **19**, 2424-2433.

81. Y. Wang, Z. Xue, Z. Sun, C. Tan, Y. Wen, S. Hu, Q. Zhu, T. Sheng and X. Wu, *Dalton Trans.,* 2015, **44**, 2217-2222.
82. Z-P Deng, L-H. Huo, H-Y. Wang, S. Gao and H. Zhai, *CrystEngComm*., 2010, **2**, 1526-1535.
83. D. Wang, Z. Hu, S. Xu, D. Li, Q. Zhang, W. Ma, H. Zhou, J. Wu and Y. Tian, *Dalton Trans.,* 2019, **48**, 1900-1905.
84. S. Romero, A. Mosset and J. C. Trombe*, J. Solid State Chem.,* 1996, **127**, 256-266.
85. R. Vaidhyanathan, S. Natarajan and C. N. R. Rao*, Inorg. Chem.,* 2002, **41**, 4496-4501.
86. W. Lin, *J. Solid State Chem*., 2005, **178**, 2486-2490.
87. C. Kittipong, P. Khemthong, F. Kierlar and Y. Zhou, *Acta Crystallogr. E. Cryst. Commun.*, 2016, **72**, 87-91.
88. I. E. Collings, M. Bykov, E. Bykova, M. G. Tucker, S. Petitgirad, M. Hanfland, K. Glazyrin, S. van Smaalen, A. L. Goodwin, L. Dubrovinsky and N. Dubrovinskaia, *CrystEngComm*, 2016, **18**, 8849-8857.
89. *CrysAlis Pro version 171.38.43,* Rigaku Oxford Diffraction, Oxfordshire, England 2016.
90. G. M. Sheldrick, *Acta Cryst. Section A,* 2008, **64**, 112-122.
91. G. M. Sheldrick, *Acta Cryst. Section A,* 2015, **71**, 3-8.
92. L. J. Bourhis, O. V. Dolomanov, R. J. Gildea, J. A. K. Howard and H. Puschmann, *Acta Cryst. Section A*, 2015, **71**, 59-75.
93. G. Sheldrick, *Acta Cryst. Section C*, 2015, **71**, 3-8.
94. O. V. Dolomanov, L. J. Bourhis, R. J. Gildea, J. A. K. Howard and H. Puschmann, *J. Appl. Crystallogr.*, 2009, **42**, 339-341.
95. Bruker, www.bruker.com, accessed June 2019.
96. H. M. Rietveld, *J. Appl. Cryst.*, 1969, **2**, 65-71.
97. A. Le Bail, *Powder Diffr.*, 2005, **20**, 316-326.
98. Rietica – a visual Rietveld program, www.rietica.org, accessed January 2019.
99. D. A. Keen and C. C. Wilson, *Single Crystal Diffraction at ISIS – User Guide for the SXD Instrument*, The Central Laboratory of the Research Councils, Didcot, 1996.
100. D. A. Keen, M. J. Gutmann and C. C. Wilson, *J. Appl. Crystallogr.*, 2006, **39**, 714-722.
101. M. J. Gutmann, *Nucl. Instrum. Meth.*, 2017, **A848**, 170-173.
102. Z-L. Xue, A. J. Ramirez-Cuesta, C. M. Brown, S. Calder, H. Cao, B. C. Chakoumakos, L. L. Daemen, A. Huq, A. I. Kolesnikov, E. Mamontov, A. A. Podlesnyak and X. Wang, *Eur. J. Inorg. Chem.*, 2019, 1065-1089.
103. M. Bée, *Quasielastic Neutron Scattering*, IOP Publishing Ltd, Bristol, 1988.
104. D. Martin, S. Cambell and C. J. Carlile, *J. Phys. Soc. Jpn.*, 1996, **65**, 245-248.
105. M. T. F. Telling and K. H. Anderson, *Phys. Chem. Chem. Phys.,* 2005, **7**, 1255-1261.
106. O. Arnold, J. C. Bilheux, J. M. Borreguero, A. Buts, S. I. Cambell, L. Chapon, M. Doucet, N. Draper, R. Ferraz Leal, M. A. Gigg, V. E. Lynch, A. Markvardsen, D. J. Mikkelson, R. L. Mikkelson, R. Miller, K. Palmen, P. Parker, G. Passos, T. G. Perring, P. F. Peterson, S. Ren, M. A. Reuter, A. T. Savici, J. W. Taylor, R. J. Taylor, R. Tolchenov, W. Zhou and J. Zikovsky, *Nucl. Instrum. Meth. A*, 2014, **764**, 156-166.

107. D. Colognesi, M. Celli, F. Cilloco, R. J. Newport, S. F. Parker, V. Rossi-Albertini, F. Sacchetti, J. Tomkinson and M. Zoppi, *Appl. Phys. A*, 2002, **74**, 64-66.
108. S. F, Parker, F. Fernandez-Alonso, A. J. Ramirez-Cuesta, J. Tomkinson, S. Rudic, R. S. Pinna, G. Gorini and J. Fernández Castañon, *J. .Phys.: Conf. Ser.*, **554**, 1.
109. OriginLab Corporation, www.OriginLab.com, accessed August 2019.
110. S. Blundell, *Superconductivity A Very Short Introduction*, Oxford University Press Inc., New York, 2009.
111. P. Hoffman, *Solid State Physics An Introduction*, Wiley-VCH Verlag GmbH & Co, Germany, 2015.
112. M. McElfresh, *Fundamentals of Magnetism and Magnetic Measurements Featuring Quantum Design's Magnetic Property Measurement System*, Quantum Design Inc., San Diego, 1994.
113. MultiVu A Cision Company, www.qdusa.com/support/software_upgrades.html, accessed August 2019.
114. S. M. Khopkar, *Basic Concepts of Analytical Chemistry*, The Control Centre, Tunbridge Wells, 2012.
115. R. D. Shannon, *Acta Crystallogr.*, 1976, **A32**, 751-767.
116. T. Spek, presented at Bruker User Meeting, Madison, 2006.
117. A. L. Spek, *Acta Cryst. Section C*, 2015, **71**, 9-18.

Appendix

Weighted R-factor, $wR_2 = \{\frac{\sum[w(F_{obs}^2 - F_{calc}^2)^2]}{\sum[w(F_{obs}^2)^2]}\}^{\frac{1}{2}}$ (Equation A.1)

Each reflection has its own weight, w.

$w = \frac{1}{\sigma^2(F_{obs}^2)+(aP)^2+bP}$ and $P = \frac{(\max(F_{obs}^2,0)2F_c^2)}{3}$ (Equation A.2)

Structure factor, $F_{hkl} = \sum_j f_i e^{2\pi i(hx_j+ky_j+lz_j)}$

The structure factor is dependant on atom position and the scattering factor, f_0, of each atom. j is the number of atoms in the unit cell.

Goodness of Fit, $S = \{\frac{\sum[w(F_{obs}^2 - F_{calc}^2)^2]}{(n-p)}\}^2$ (Equation A.3)

Where n = number of reflections and p = totally number of parameters refined.

Weighted profile R-factor, $R_{wp} = [\frac{\sum_i w_i(y_{obs}-y_{calc})^2}{\sum_i w_i y_{obs}^2}]^{\frac{1}{2}}$ (Equation A.4)

The weighed profile R-factor is determined by all the peaks, not only the most intense ones but it also depends on the background this is to increase the quality of the refinement.

Expected R-factor, $R_{exp} = [\frac{N-P}{\sum_i w_i y_{obs}^2}]^{\frac{1}{2}}$ (Equation A.5)

Where N = number of observations and P = number of parameters, but the expression is dictated by the size of N and R_{exp} is a measure of the data quality.

Goodness of fit, $\chi^2 = (\frac{R_{wp}}{R_{exp}})^2$ (Equation A.6)

The goodness of fit is the ratio between R_{wp} and R_{exp}, as demonstrated by equation A.5, it's value cannot be less than 1, but the nearer the 1, the better the fit of the model.

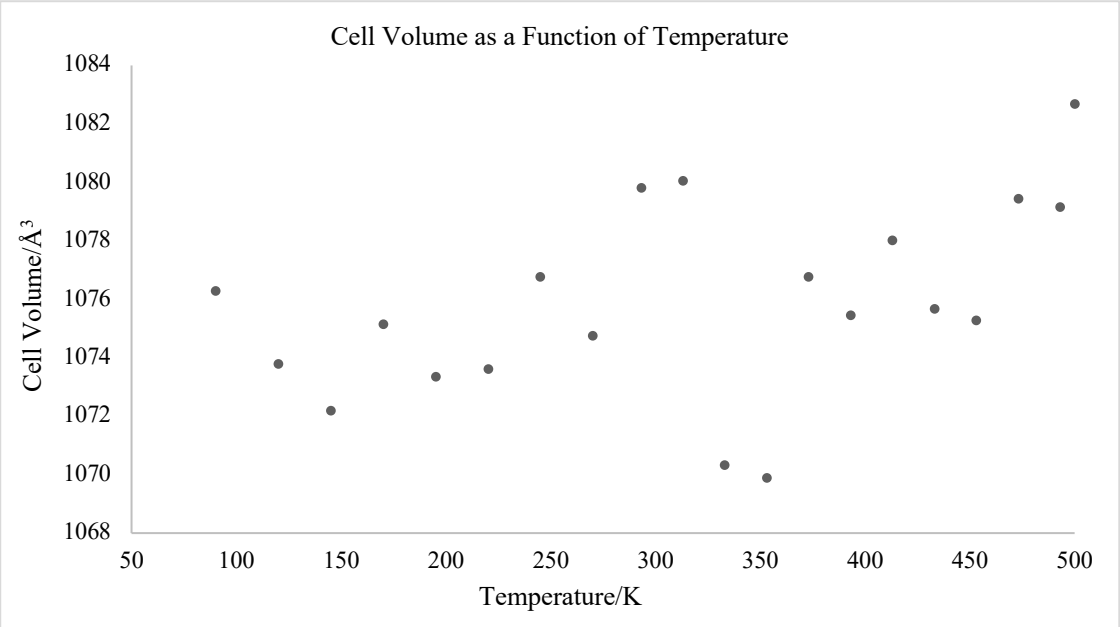


Figure A.1. Cell volume as a function of temperature of **1Er**.

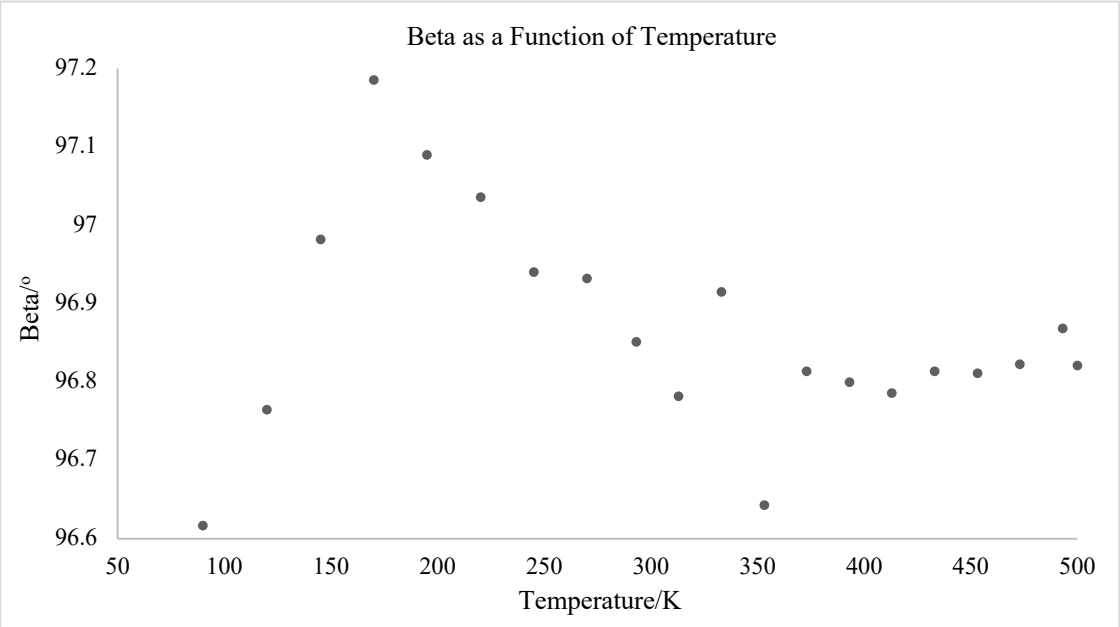


Figure A.2. Angle Beta as a function of temperature of **1Er**.

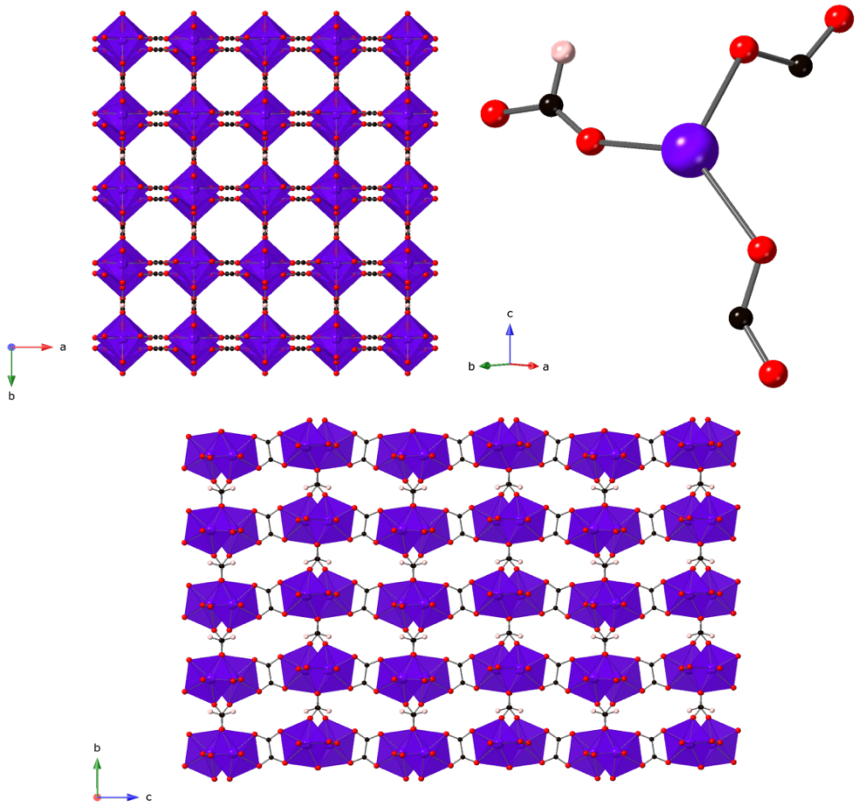


Figure A.3. Crystal structure of **2Tb** at 293 K, along the *c*-axis (top left), asymmetric unit (top right) and along the *a*-axis (bottom). Tb polyhedra shown in purple, C: black, O: red and H: pink.

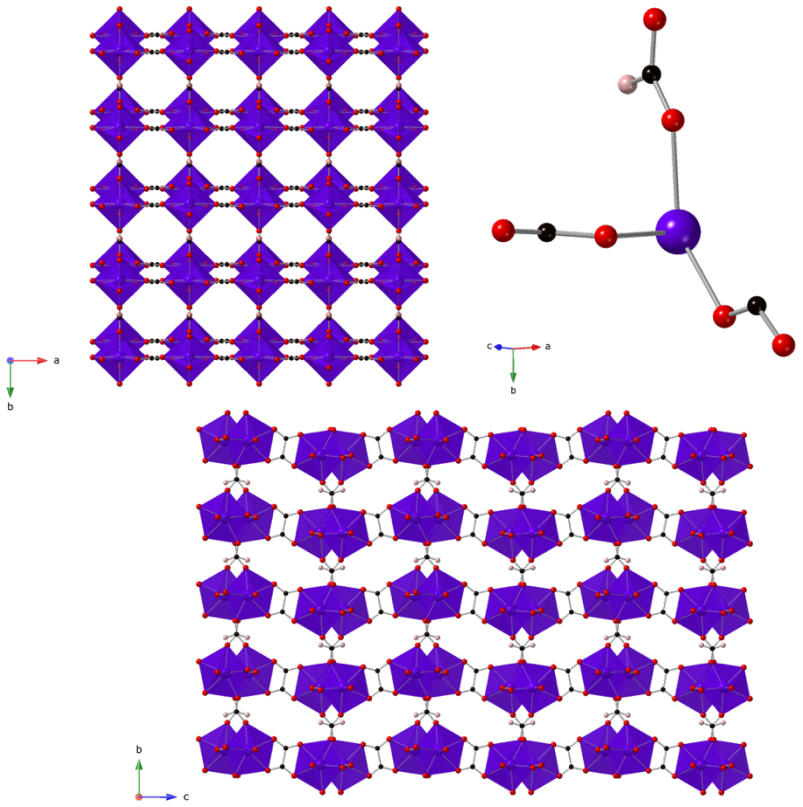


Figure A.4. Crystal structure of **2Tb** at 100 K, along the *c*-axis (top left), asymmetric unit (top right) and along the *a*-axis (bottom). Tb polyhedra shown in purple, C: black, O: red and H: pink.

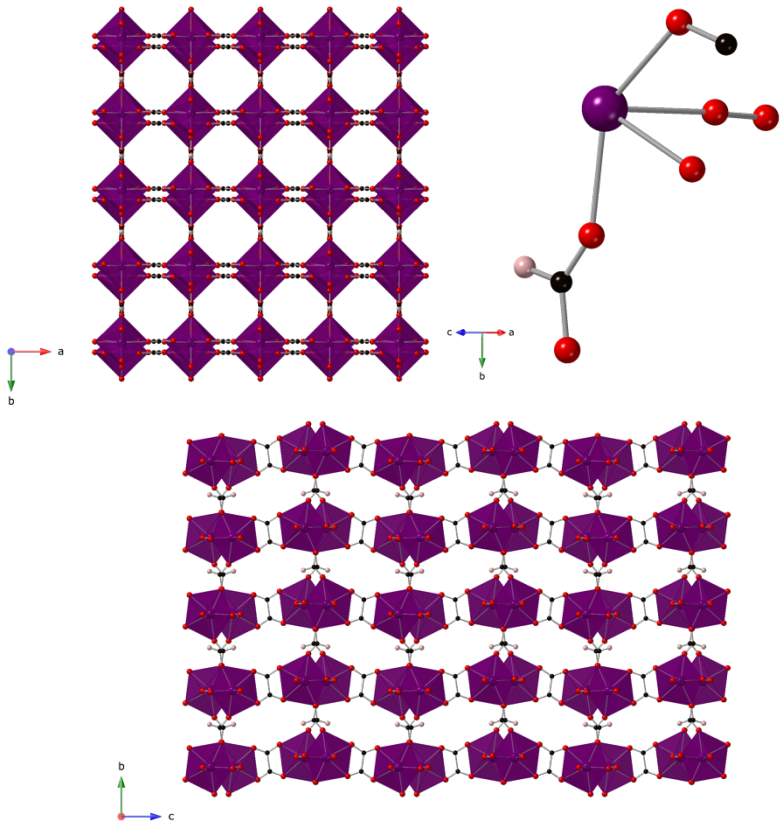


Figure A.5. Crystal structure of **3Dy** at 293 K, along the *c*-axis (top left), asymmetric unit (top right) and along the *a*-axis (bottom). Dy polyhedra shown in maroon, C: black, O: red and H: pink.

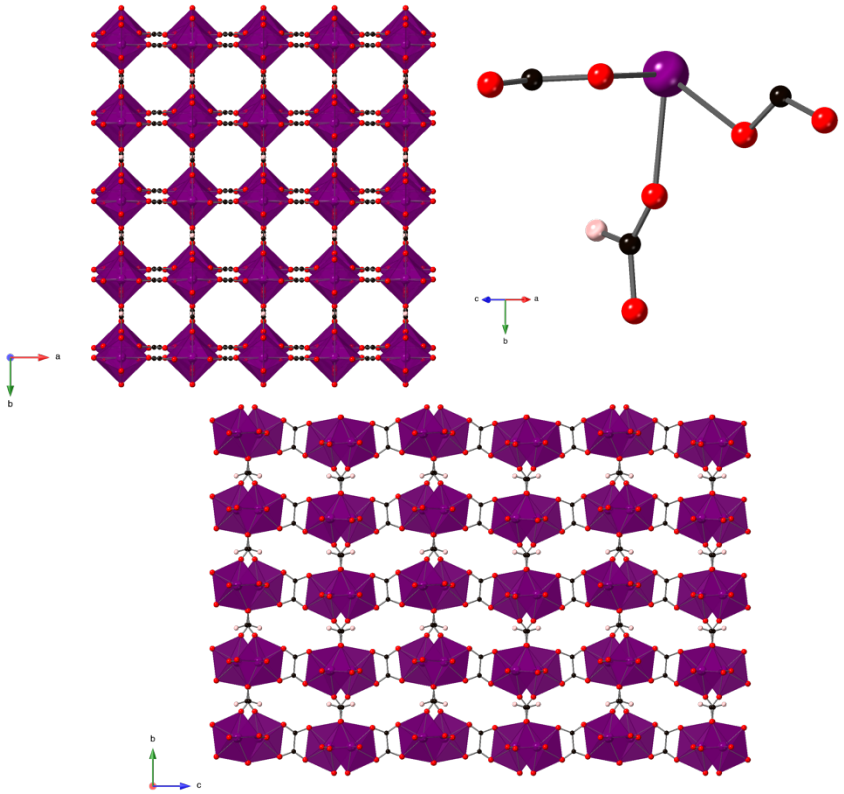


Figure A.6. Crystal structure of **3Dy** at 100 K, along the *c*-axis (top left), asymmetric unit (top right) and along the *a*-axis (bottom). Dy polyhedra shown in maroon, C: black, O: red and H: pink.

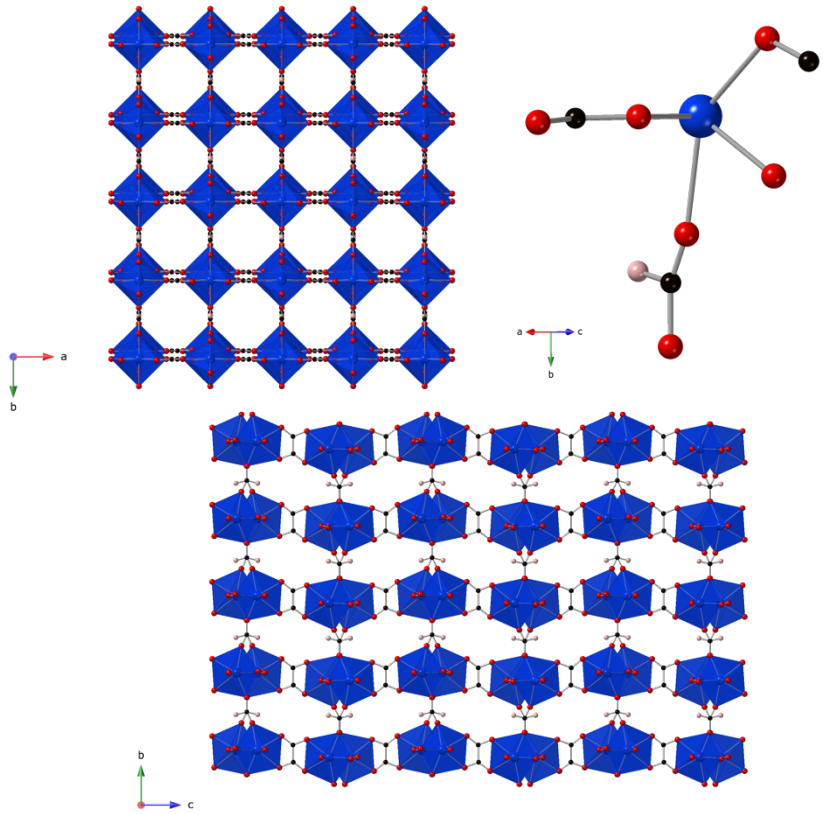


Figure A.7. Crystal structure of **4Ho** at 293 K, along the *c*-axis (top left), asymmetric unit (top right) and along the *a*-axis (bottom). Ho polyhedra shown in blue, C: black, O: red and H: pink.

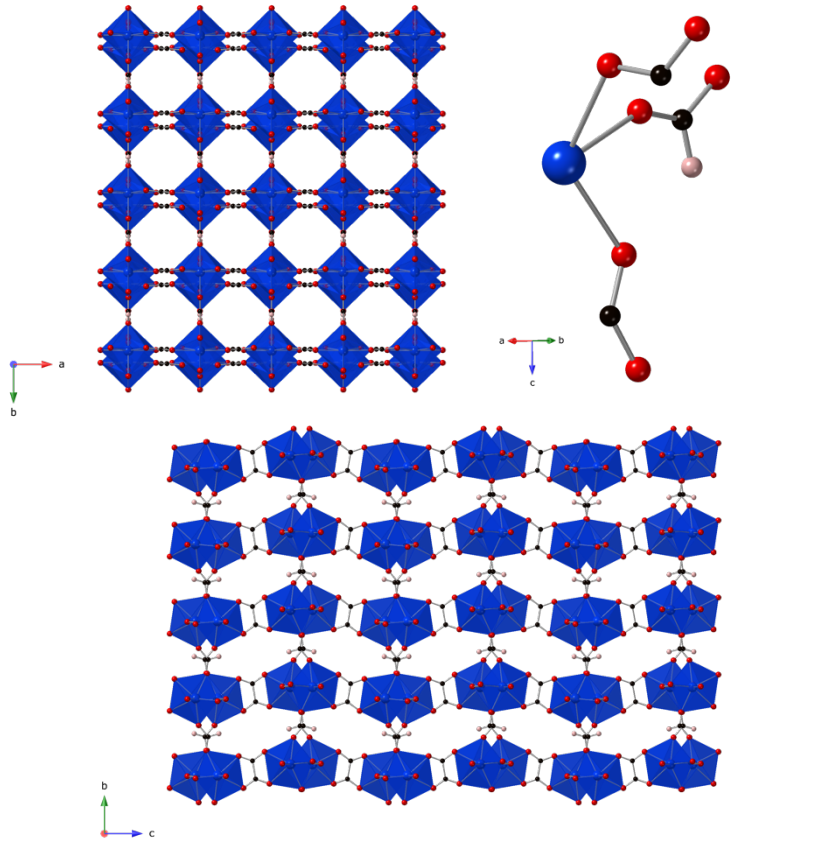


Figure A.8. Crystal structure of **4Ho** at 100 K, along the *c*-axis (top left), asymmetric unit (top right) and along the *a*-axis (bottom). Ho polyhedra shown in blue, C: black, O: red and H: pink.

Table A.1. Organic component bond distances and angles in **2Tb** at 293 K.

Bond	**Range in length/Å**
C-O (formate)	1.14(5)-1.28(6)
C-O (oxalate)	1.22(5)-1.28(3)
Angle	**Range in angle/°**
O-C-O (formate)	133(5)
O-C-O (oxalate)	124(4)-126(2)

Table A.2. Organic component bond distances and angles in **2Tb** at 100 K.

Bond	**Range in length/Å**
C-O (formate)	1.161(17)-1.97(15)
C-O (oxalate)	1.241(13)-1.252(12)
Angle	**Range in angle/°**
O-C-O (formate)	132.9(14)
O-C-O (oxalate)	126.8(8)-128(9)

Table A.3. Organic component bond distances and angles in **3Dy** at 293 K.

Bond	**Range in length/Å**
C-O (formate)	1.12(2)-1.24(2)
C-O (oxalate)	1.214(19)-1.253(19)
Angle	**Range in angle/°**
O-C-O (formate)	132(2)
O-C-O (oxalate)	127.1(13)-122.3(12)

Table A.4. Organic component bond distances and angles in **3Dy** at 100 K.

Bond	**Range in length/Å**
C-O (formate)	1.11(4)-1.22(4)
C-O (oxalate)	1.20(3)-1.26(3)
Angle	**Range in angle/°**
O-C-O (formate)	137(5)
O-C-O (oxalate)	124(3)-126(2)

Table A.5. Organic component bond distances and angles in **4Ho** at 293 K.

Bond	**Range in length/Å**
C-O (formate)	1.03(4)-1.23(4)
C-O (oxalate)	1.21(3)-1.25(3)
Angle	**Range in angle/°**
O-C-O (formate)	154(4)
O-C-O (oxalate)	122(3)-126(2)

Table A.6. Organic component bond distances and angles in **4Ho** at 100 K.

Bond	**Range in length/Å**
C-O (formate)	1.16(2)-1.24(2)
C-O (oxalate)	1.21(2)-1.259(19)
Angle	**Range in angle/°**
O-C-O (formate)	132(2)
O-C-O (oxalate)	124.8(14)-127(11)

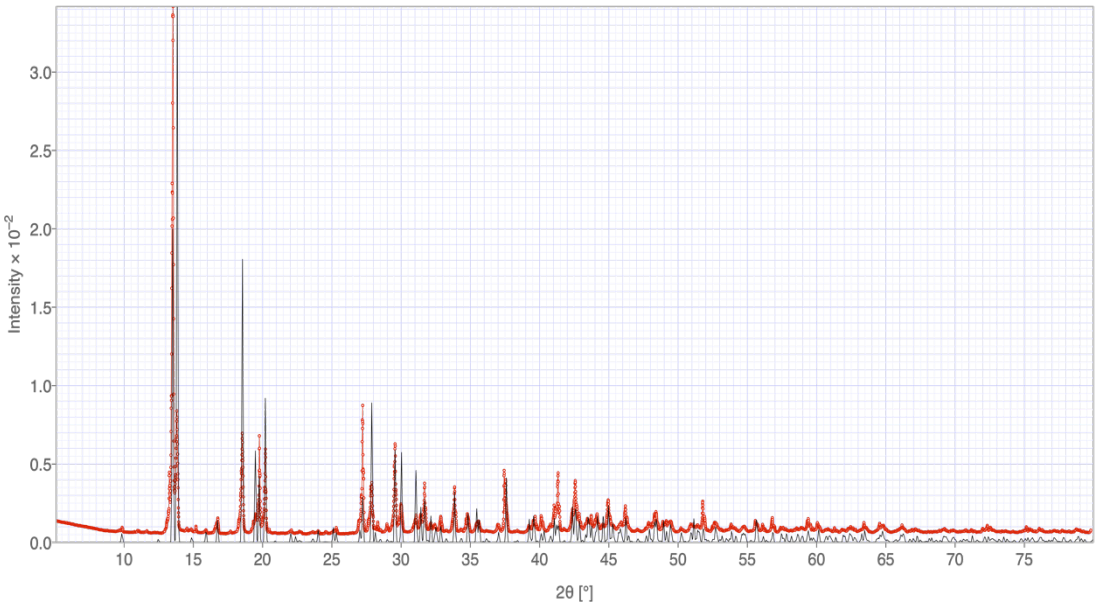


Figure A.9. PXRD pattern of **1Er**. Black: CIF of **2Tb**, red: PXRD pattern of pure phase.

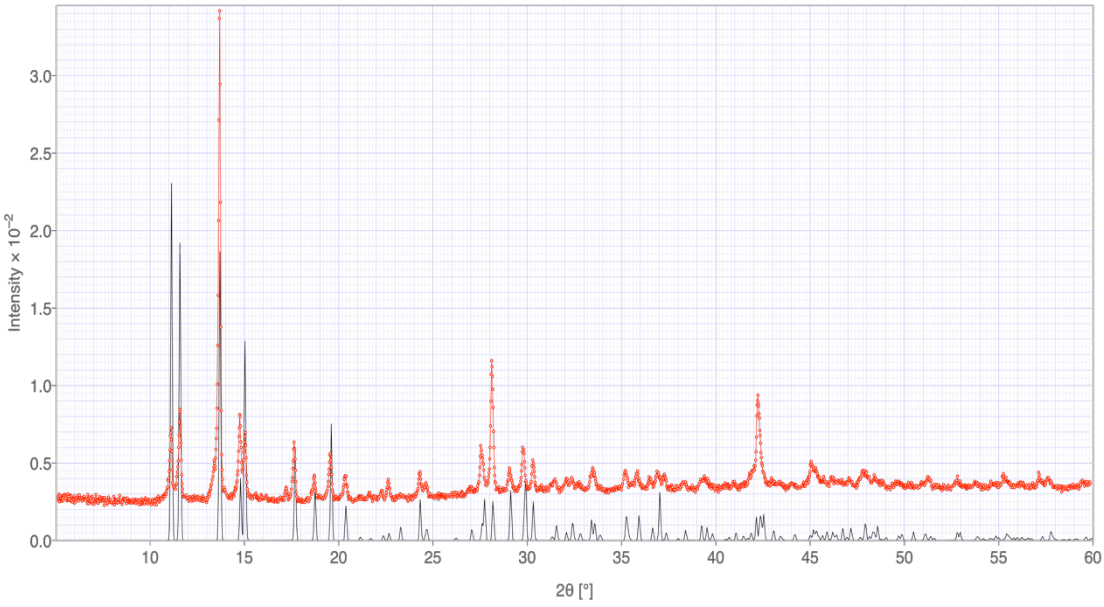


Figure A.10. PXRD pattern of **2Tb**. Black: CIF of **2Tb**, red: PXRD pattern of pure phase.

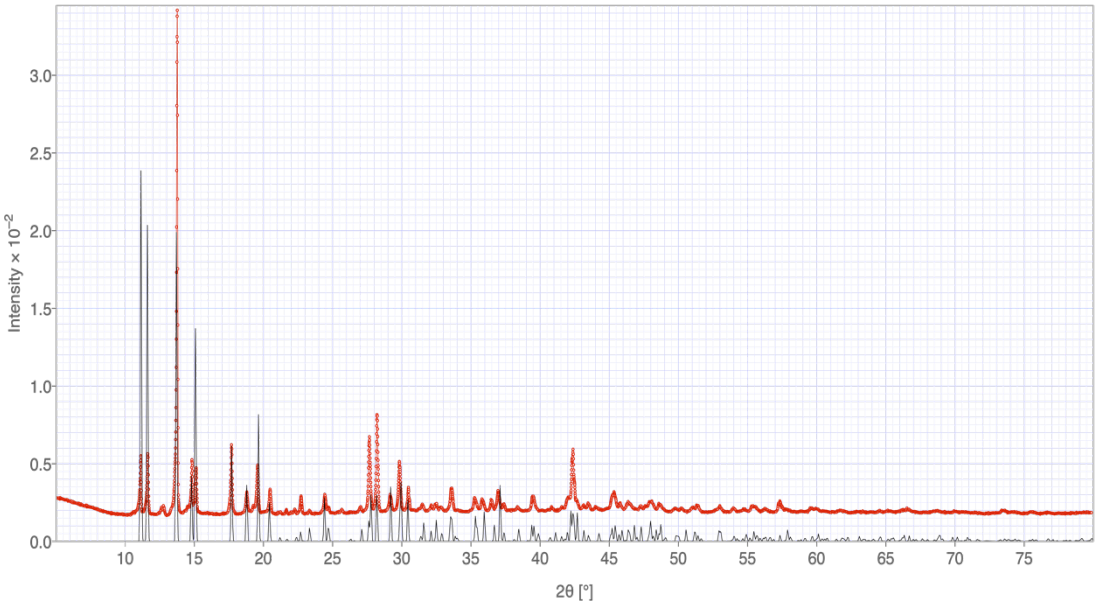


Figure A.11. PXRD pattern of **3Dy**. Black: CIF of **3Dy**, red: PXRD pattern of pure phase.

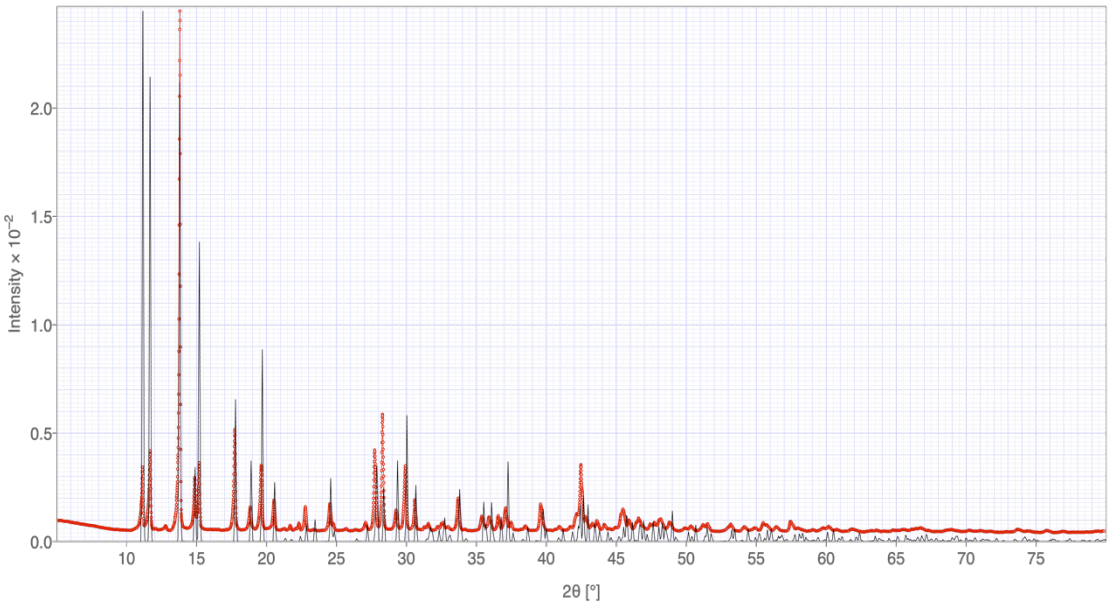


Figure A.12. PXRD pattern of **4Ho**. Black: CIF of **4Ho**, red: PXRD pattern of pure phase.

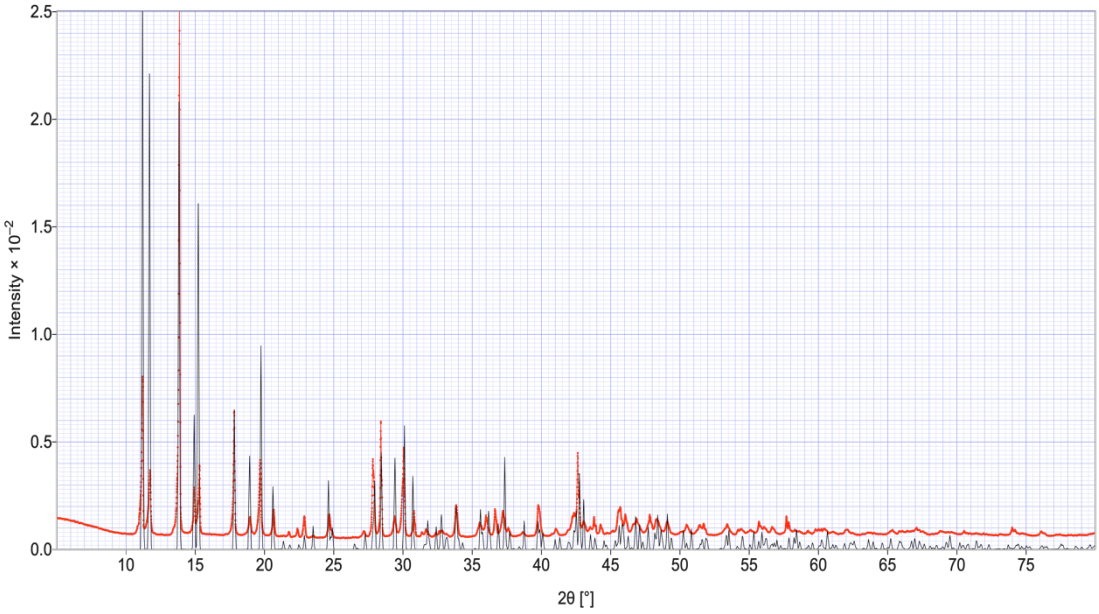


Figure A.13. PXRD pattern of **5Er**. Black: CIF of **5Er**, red: PXRD pattern of pure phase.

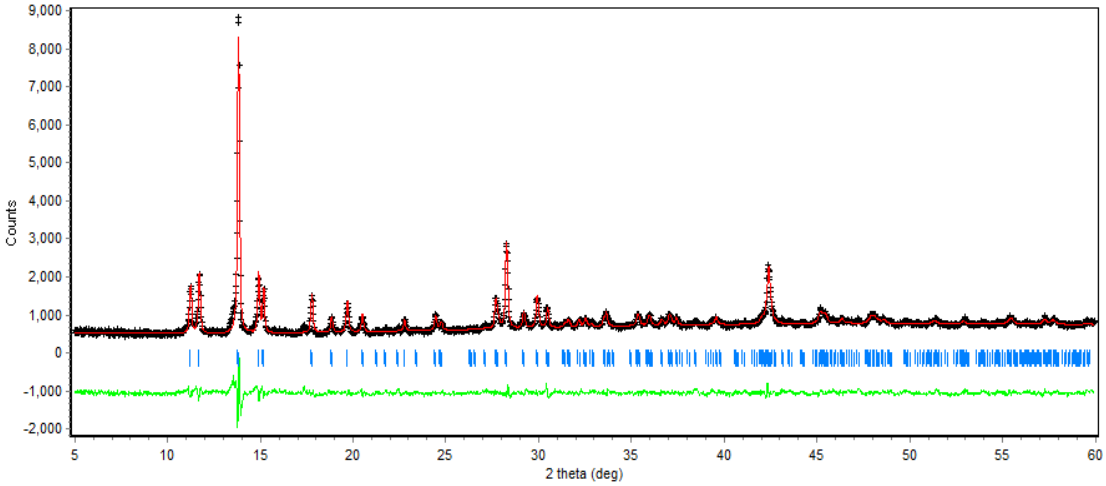


Figure A.14. Le Bail refinement of **2Tb**. R_p = 4.724, R_{wp} = 6.622 and χ^2 = 3.389. Lattice parameters: a = 11.79(13), b = 12.950(9) and c = 15.98(14). Colour scheme same as in Figure 3.5.

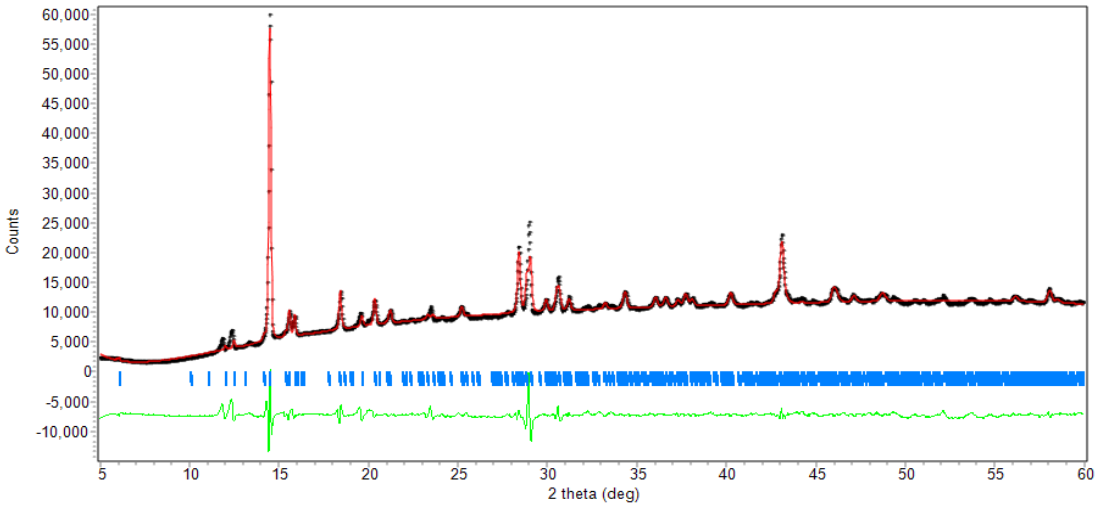


Figure A.15. Le Bail refinement of **3Dy**. R_p = 2.794, R_{wp} = 5.044 and χ^2 = 24.71. Lattice parameters: *a* = 11.62(3), *b* = 12.75(2) and *c* = 15.44(3). Colour scheme same as in Figure 3.5.

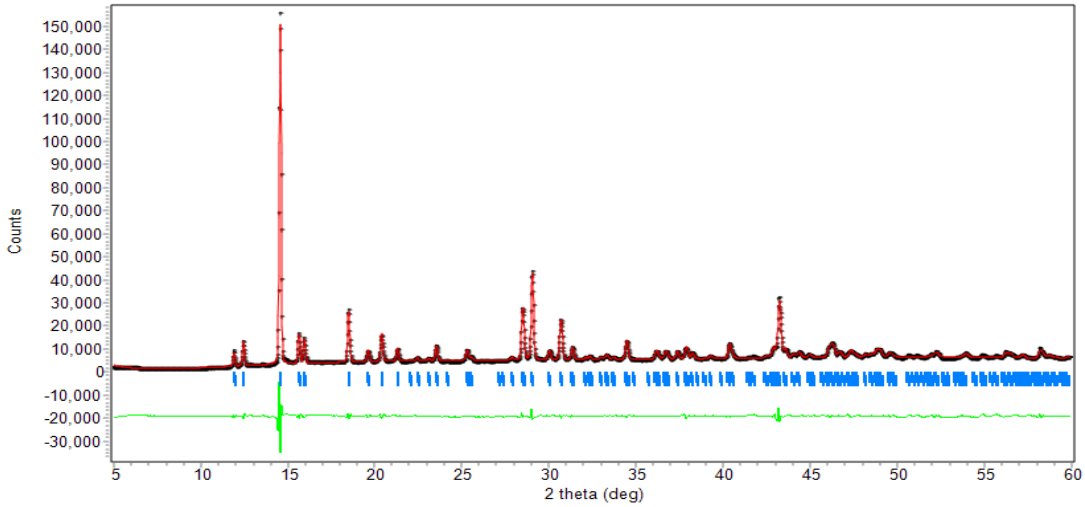


Figure A.16. Le Bail refinement of **4Ho**. R_p = 4.127, R_{wp} = 5.791 and χ^2 = 22.21. Lattice parameters: *a* = 11.746(6), *b* = 12.945(4) and *c* = 15.993(7). Colour scheme same as in Figure 3.5.

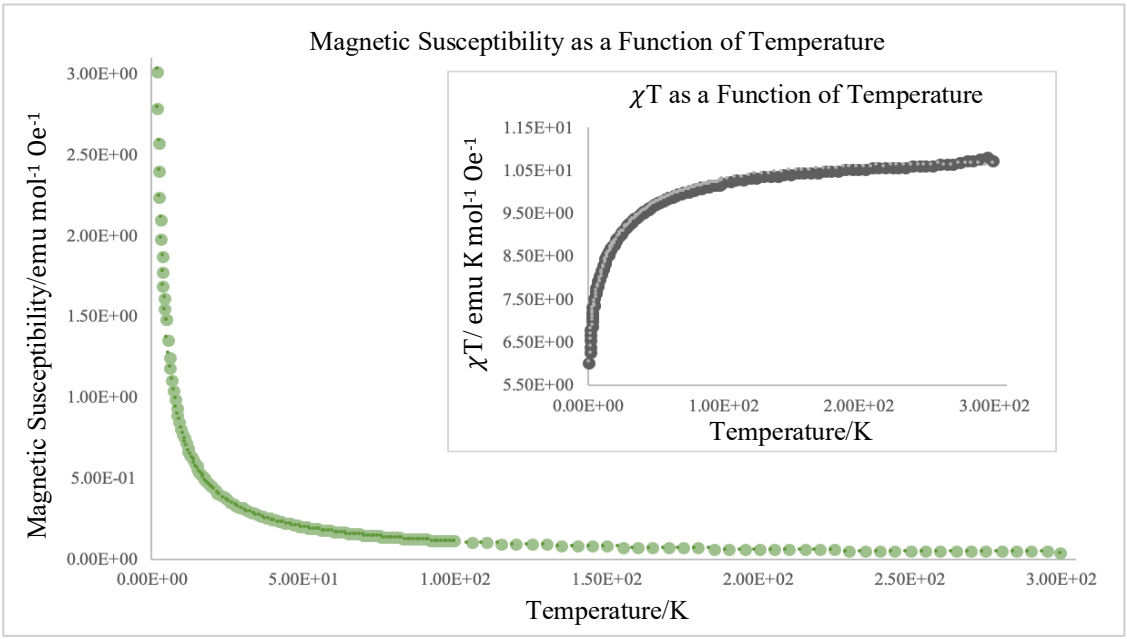


Figure A.17. Magnetic susceptibility as a function of temperature of **2Tb**. Pale green and dark grey: ZFC, dark green and pale grey: FC.

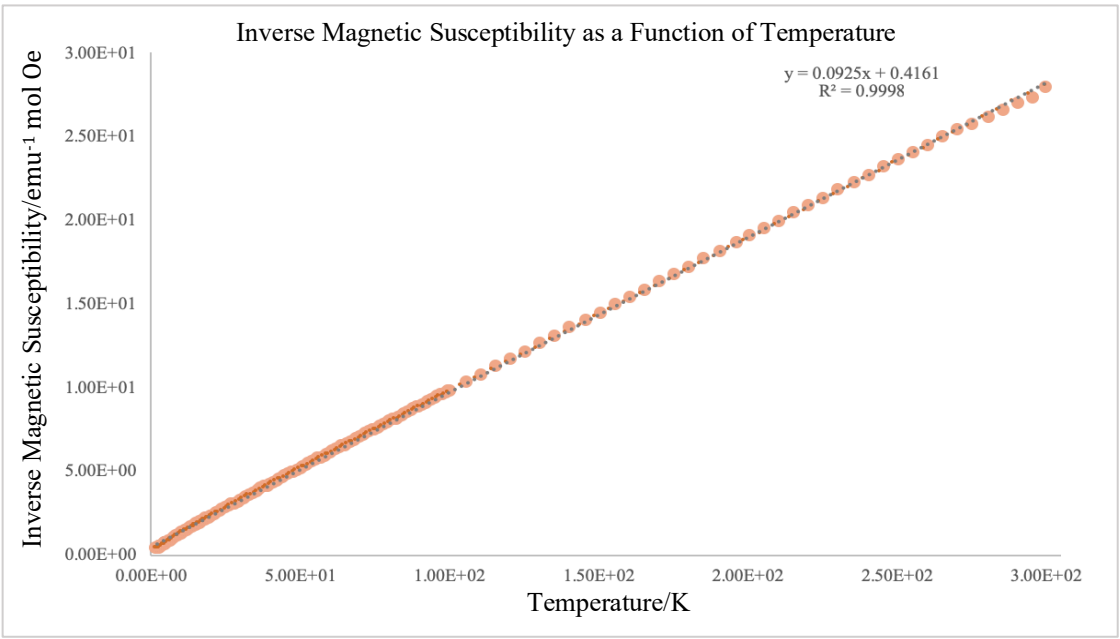


Figure A.18. Curie-Weiss plot of **2Tb**. Pale orange: ZFC and dark orange: FC.

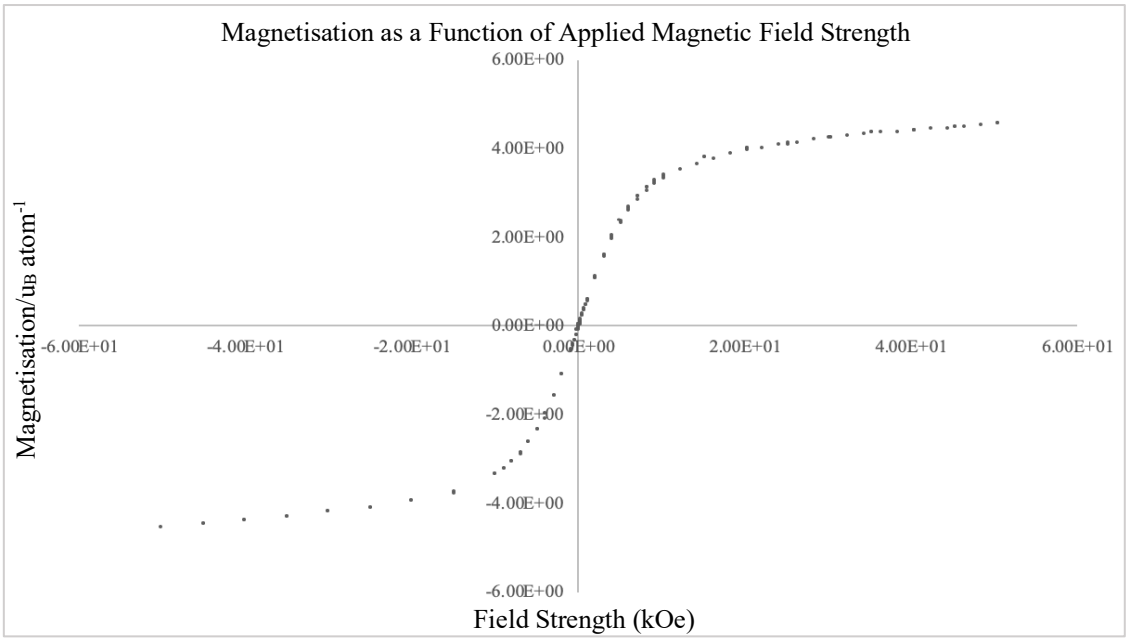


Figure A.19. Magnetisation as a function of applied magnetic field strength of **2Tb**.

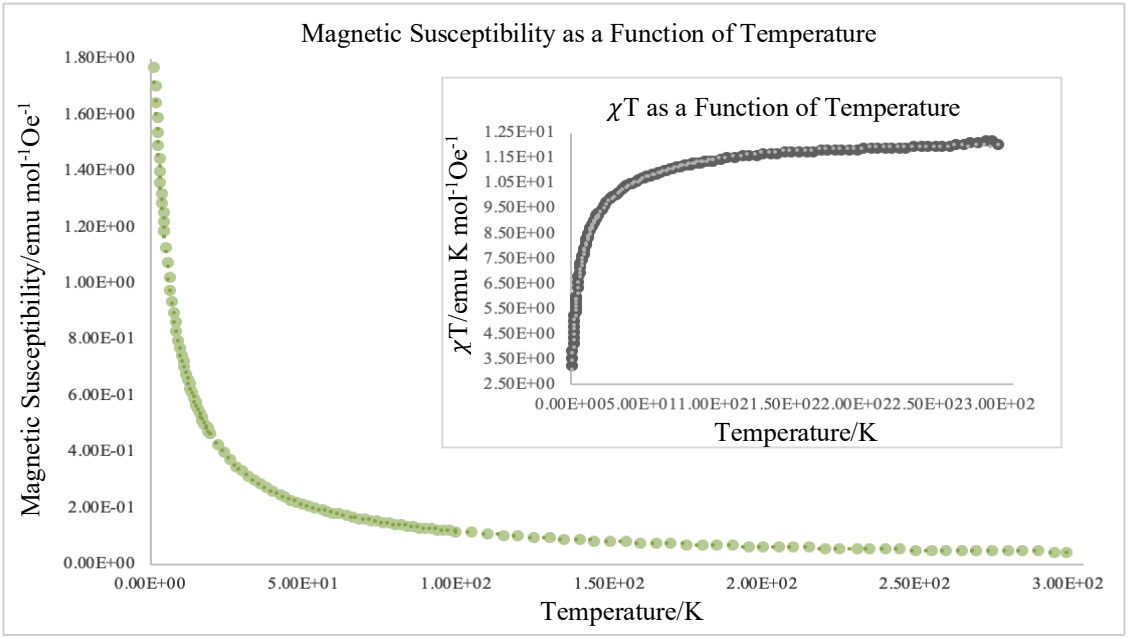


Figure A.20. Magnetic susceptibility as a function of temperature of **3Dy**. Pale green and dark grey: ZFC, dark green and pale grey: FC.

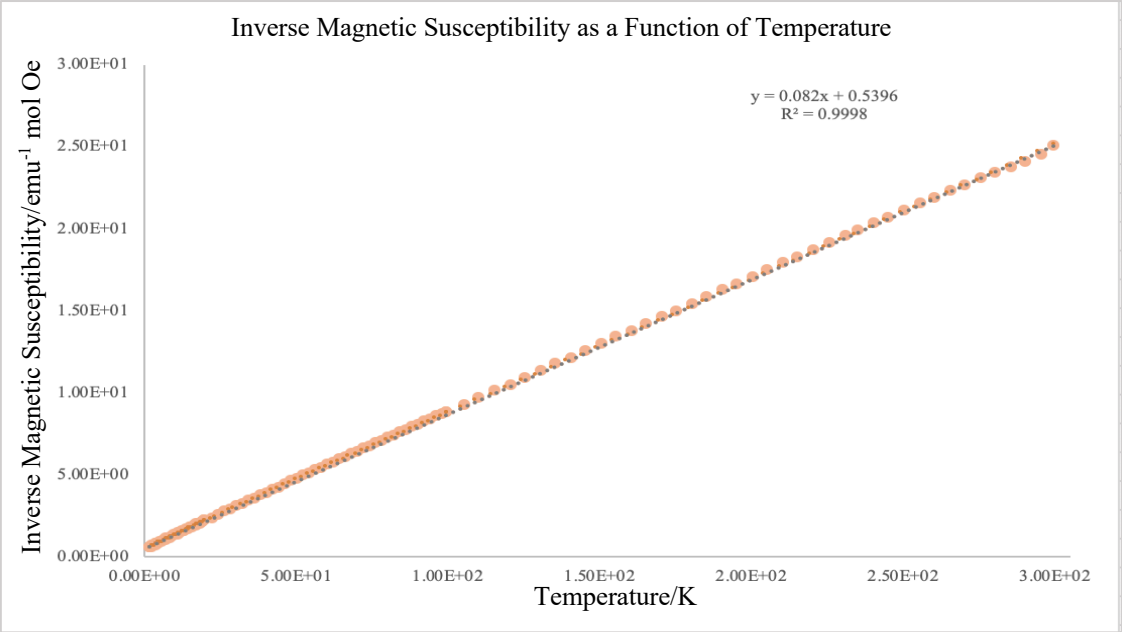


Figure A.21. Curie-Weiss plot of **3Dy**. Pale orange: ZFC and dark orange: FC.

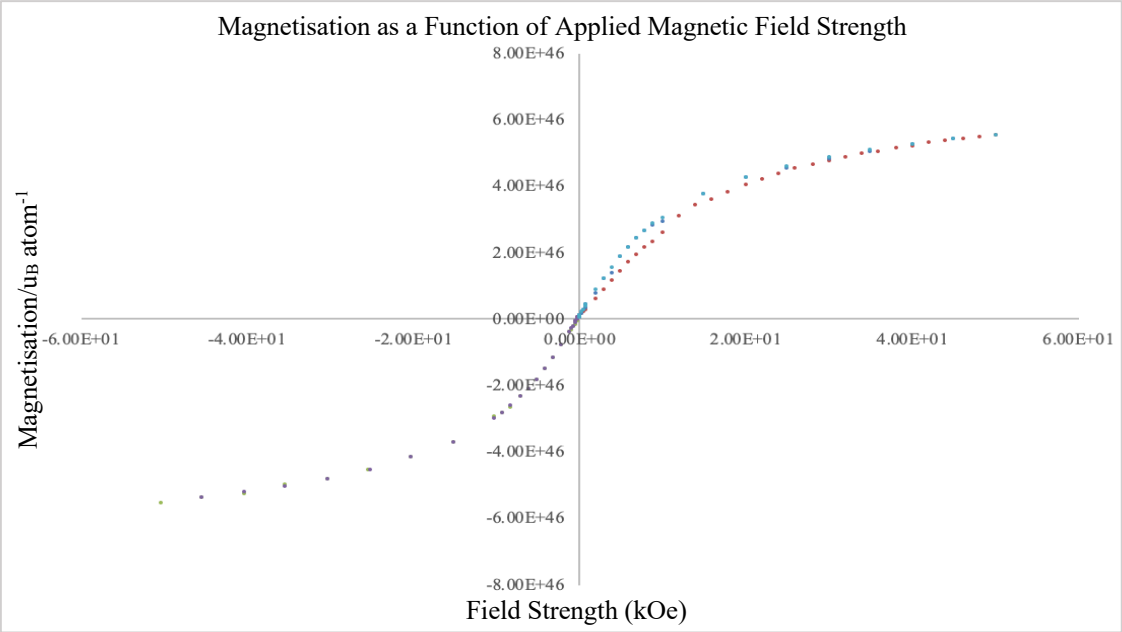


Figure A.22. Magnetisation as a function of applied magnetic field strength of **3Dy**.

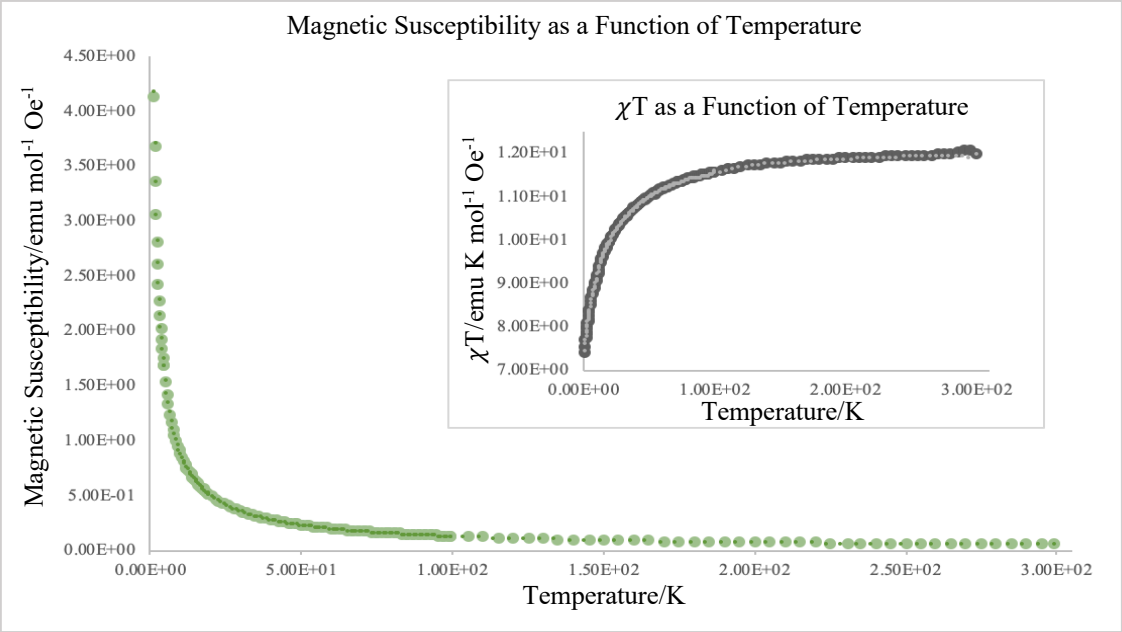


Figure A.23. Magnetic susceptibility as a function of temperature of **4Ho**. Pale green and dark grey: ZFC, dark green and pale grey: FC.

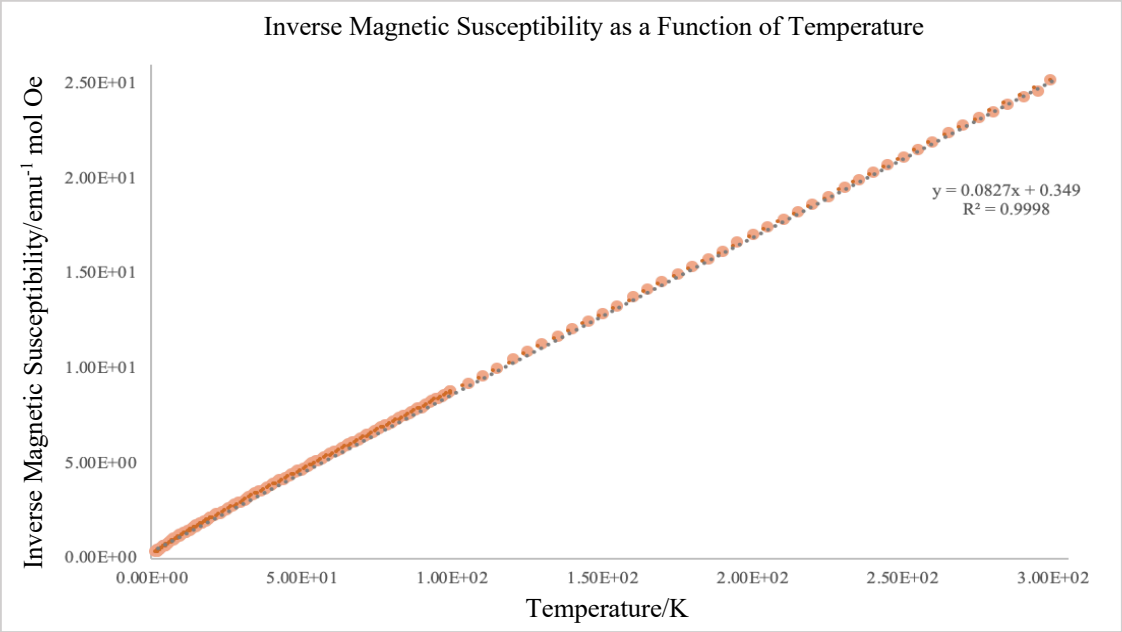


Figure A.24. Curie-Weiss plot of **4Ho**. Pale orange: ZFC and dark orange: FC.

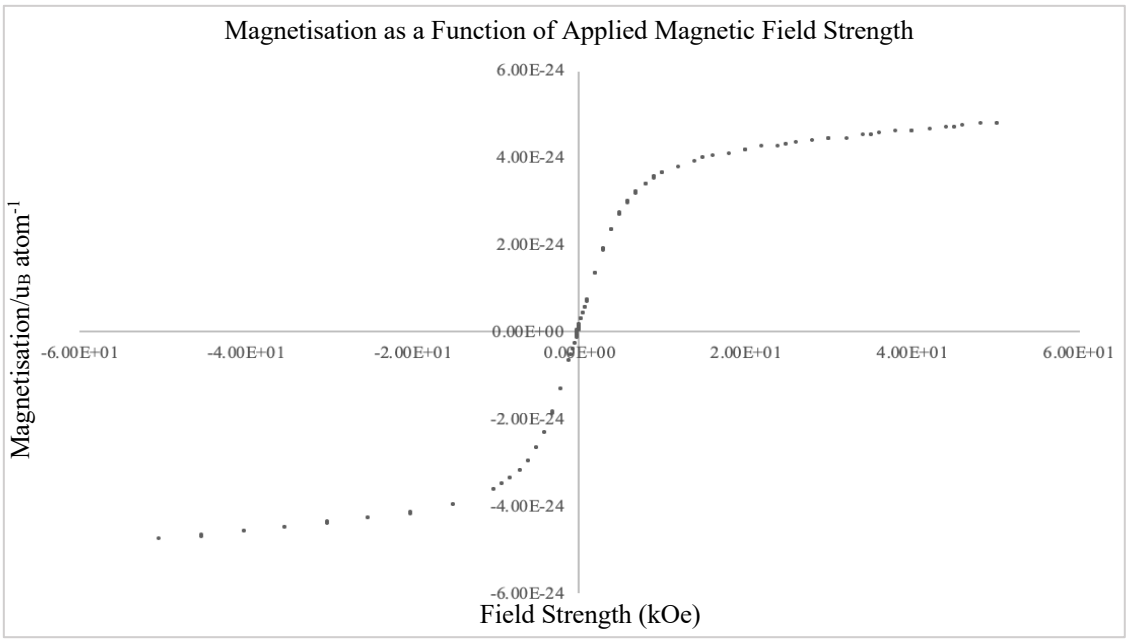


Figure A.25. Magnetisation as a function of applied magnetic field strength of **4Ho**.

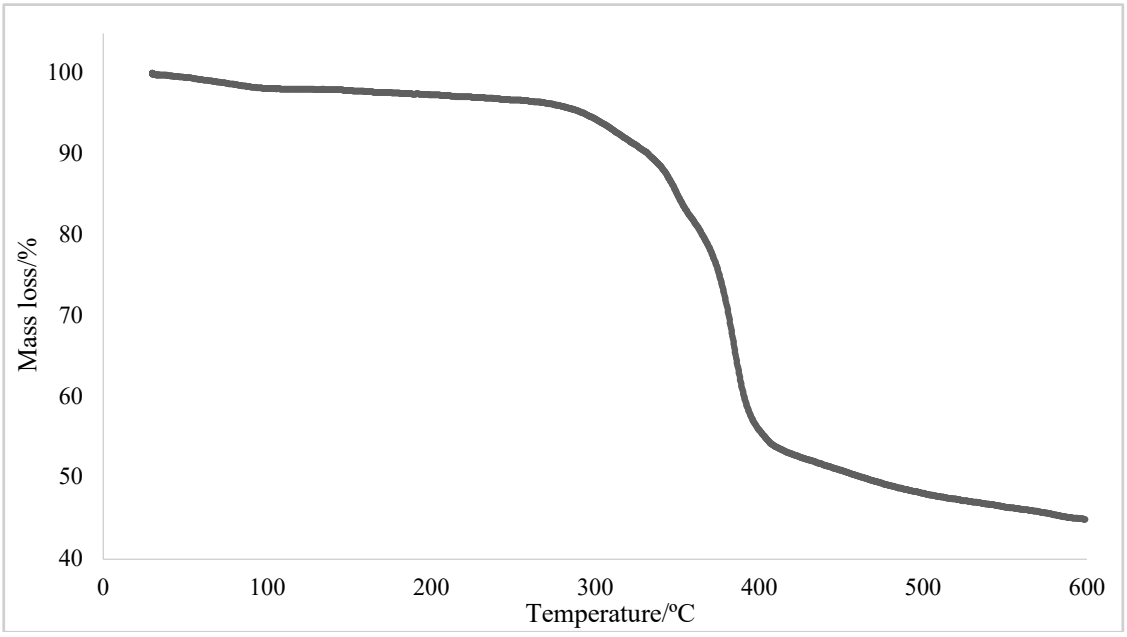


Figure A.26. Percentage mass loss (%) of **2Tb** as a function of temperature (°C) measured using Thermogravimetric Analysis (TGA).

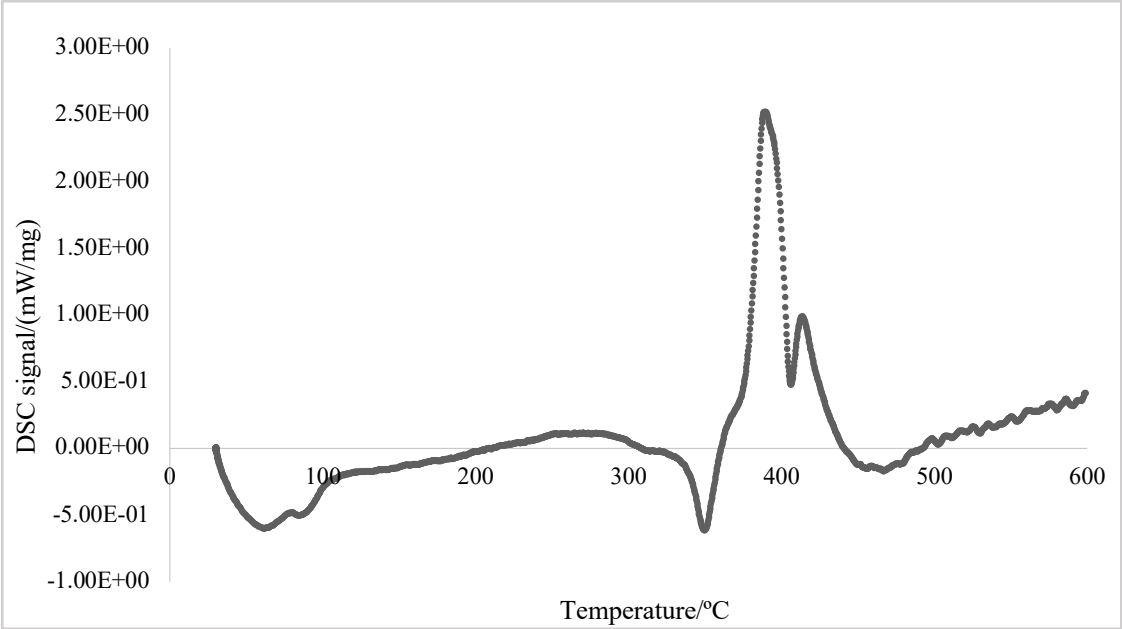


Figure A.27. Heat capacity (mW/mg) of **2Tb** as a function of temperature (°C) using Differential Scanning Calorimetry (DSC).

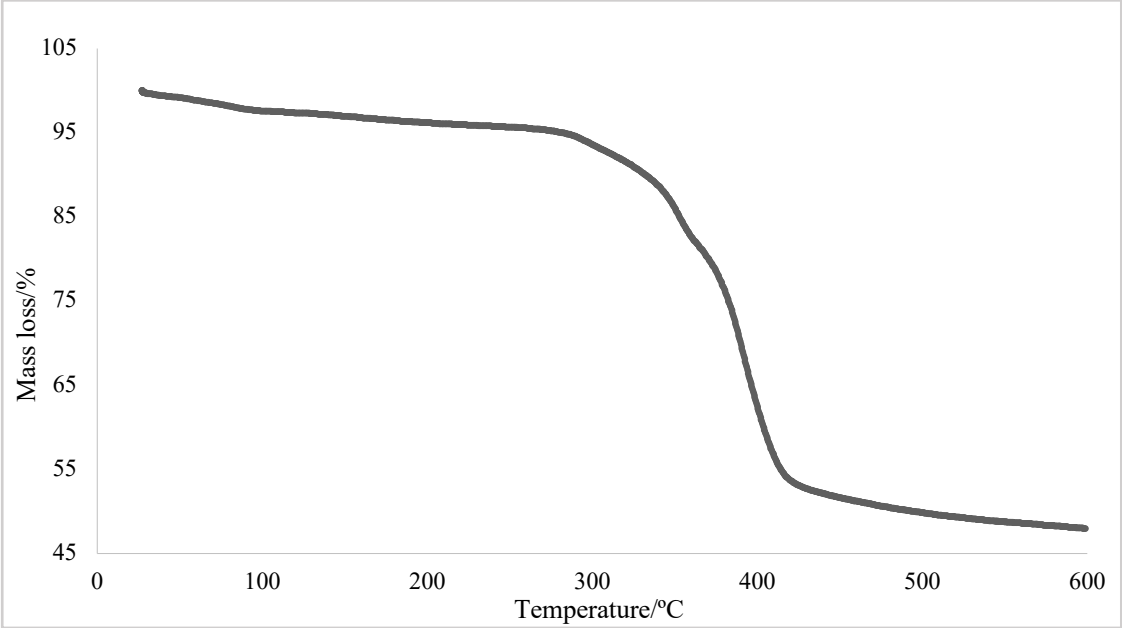


Figure A.28. Percentage mass loss (%) of **3Dy** as a function of temperature (°C) measured using Thermogravimetric Analysis (TGA).

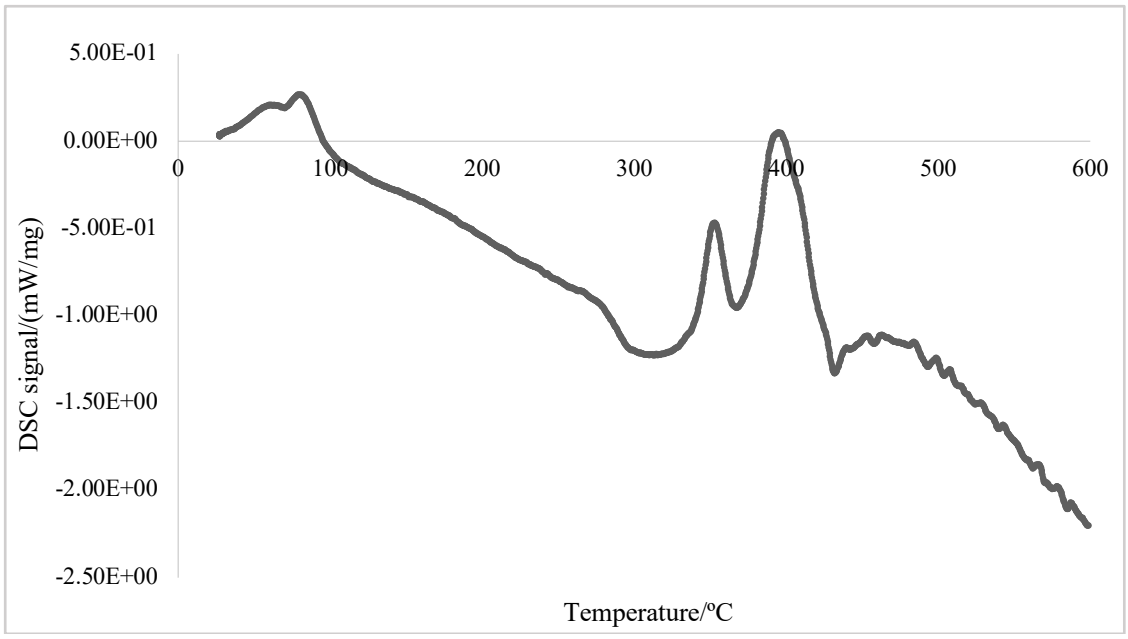


Figure A.29. Heat capacity (mW/mg) of **3Dy** as a function of temperature (°C) using Differential Scanning Calorimetry (DSC).

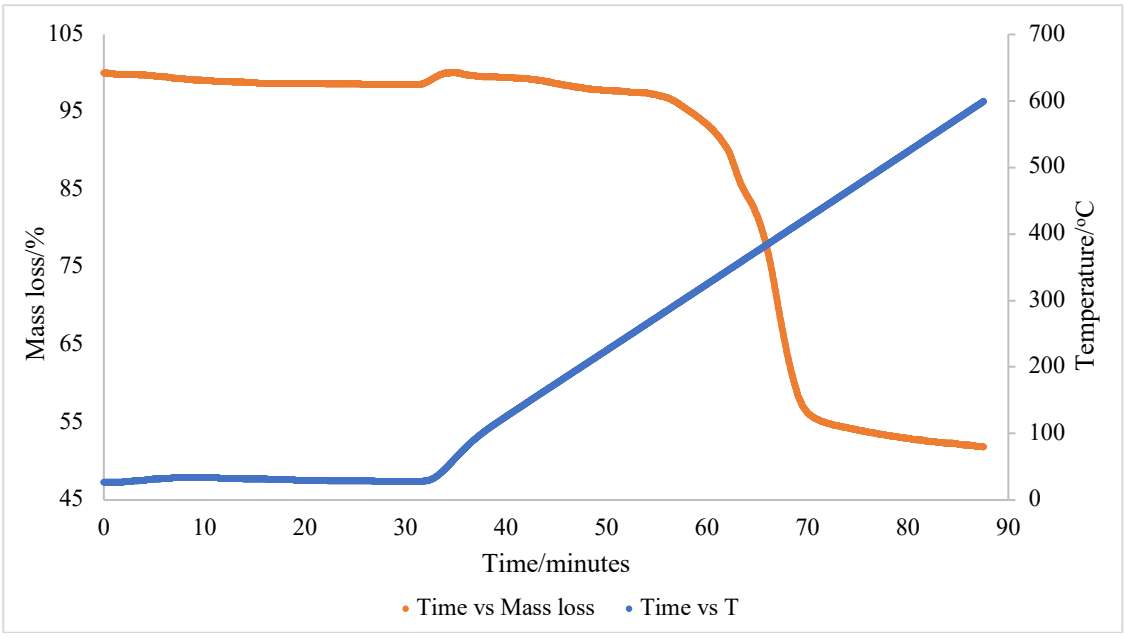


Figure A.30. Percentage mass loss (%) of **4Ho** as a function of temperature (°C) measured using Thermogravimetric Analysis (TGA).

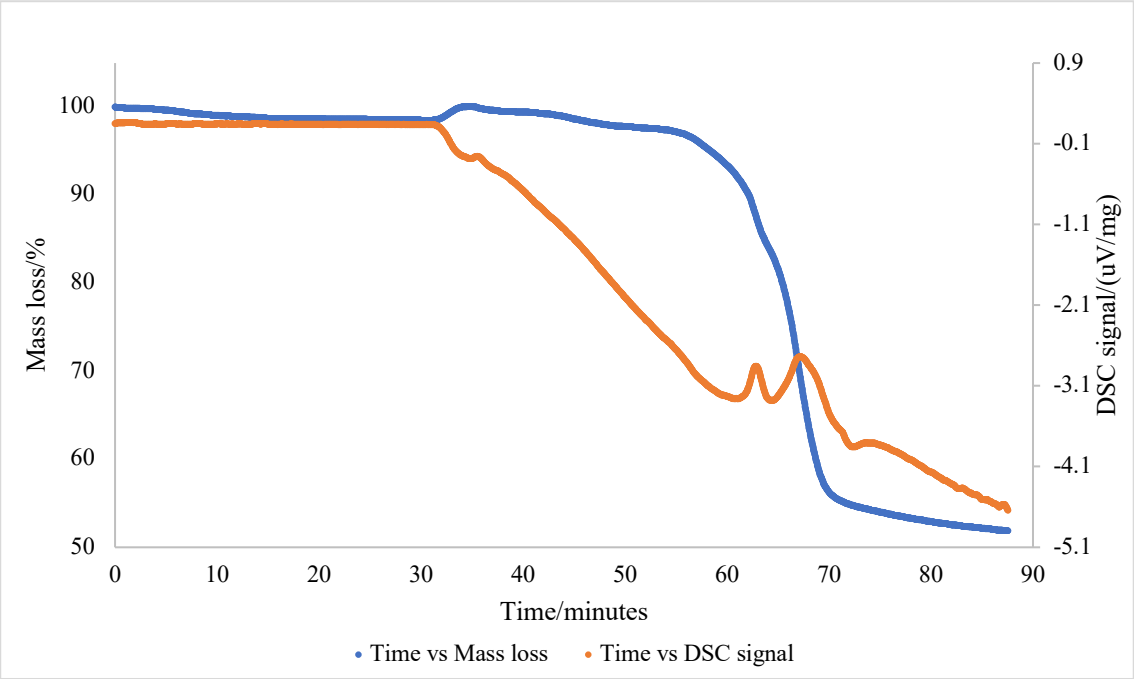


Figure A.31. Heat capacity (mW/mg) of **4Ho** as a function of temperature (°C) using Differential Scanning Calorimetry (DSC).

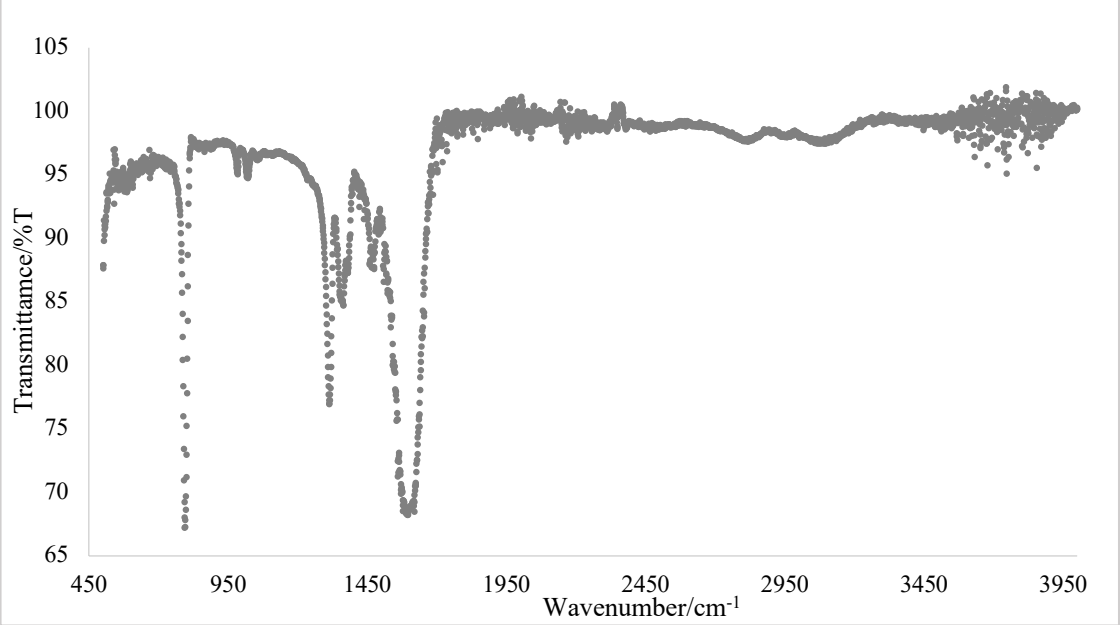


Figure A.32. IR spectrum of **3Dy**.

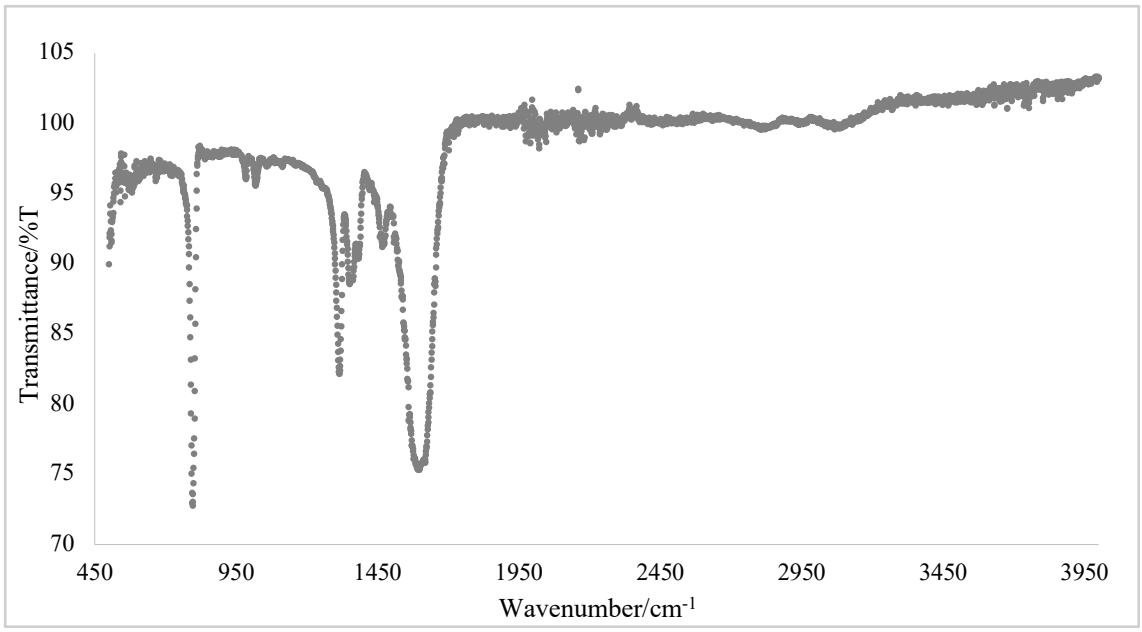


Figure A.33. IR spectrum of **4Ho**.